INTERFACIAL DESIGN AND MECHANICS ANALYSIS OF ADVANCED MATERIALS AND STRUCTURES

By

Sreeparna Sengupta

Dissertation

Submitted to the Faculty of the

Graduate School of Vanderbilt University

in partial fulfillment of the requirements

for the degree of

DOCTOR OF PHILOSOPHY

in

Civil Engineering

May, 2007

Nashville, Tennessee

Approved

Professor Roy L Xu

Professor Sankaran Mahadevan

Professor Prodyot K Basu

Professor Carol Rubin

To my Father, the Fighter
Hironmoy Sengupta

ACKNOWLEDGEMENT

I would like to express my gratitude to my dissertation advisor and committee chairman, Dr Roy Xu for his guidance and financial support during my stay at Vanderbilt University; Dr Sankaran Mahadevan for being more than a committee member – a mentor and a father figure; Dr Prodyot Basu for being instrumental in starting me off both in the academic and the real world and Dr Carol Rubin for being a sounding board whenever I needed to test ideas. Thanks are also due to Dr David Kosson and Dr Sanjiv Gokhale for going beyond their line of duty in helping me out of untoward situations. Dr Jy-An John Wang at OakRige National Laboratory was a teacher in the true sense of the term, encouraging and guiding me during my brief summer stay at OakRidge, Tennessee.

On a personal note; my friends and colleagues have been ever supportive and never let me forget the pitfalls of a dissertation left undone. In particular, Rituparna Ghosh, Nivedita Sumi Majumdar and Sarmistha Bhattacharya stood my raves and rants in good stead. My amazing friends-in-graduation – Surya, Sarit, Sohini and Ravi – you are the very best. To conclude; my parents, Hironmoy and Basanti Sengupta, and my sisters, Sreerupa and Shreya Sengupta, deserve accolades for their patience and understanding and I hope to have honored their daily sacrifices to the best of my ability.

TABLE OF CONTENTS

LIST OF TABLES

Page

LIST OF FIGURES

Page

CHAPTER I

INTRODUCTION

Many natural and technological processes involve phenomena dominated by interfacial mechanics – occurring within the overlapping region between several solid/fluid phases. Interfacial phenomena typically involve interplay of complex processes and the exact mechanics involving such processes is still not fully understood. As advanced materials and structures are being investigated to better optimize weight, cost and strength, it is imperative that material interfaces be better characterized in terms of their properties, thereby increasing reliability in usage.

Most structural failures are generally caused by either negligence during design, construction, operation etc or application of a new design or material. Stress singularity, as a mathematical phenomenon, and stress concentration, as a practical impediment, have been a major cause for concern in jointed structures encountered in daily life. Interfaces have always been the most vulnerable site for failure arising from stress concentrations associated with material and/or geometric discontinuity. A novel approach has been described and implemented in the second chapter to remove stress singularity and produce more reliable material strength data.

Reliability can be increased either by building better structures or by manufacturing better materials. Of late, carbon nanotubes and fullerenes are being cited as materials of the future. The search for new carbon nanostructures, higher mass fullerenes has strongly motivated chemists and physicists to utilize carbon nanotubes and

fibers to build stronger yet lighter structures. However, the application of a new design or material often produces unexpected and undesirable results and the incorporation of graphitic carbon nanofibers in an epoxy matrix did not increase the tensile strength of bonded interfaces. An explanation was sought for this behavior whereby interfacial stress transfer in nanocomposites was examined in the third chapter.

While the traditional strength of materials approach compares applied stress to yield/tensile strength, the fracture mechanics approach to design replaces tensile strength with fracture toughness and flaw size. The fourth chapter takes a critical look at existing methods of fracture toughness measurement and their shortcomings. A new experimental method developed at ORNL is proposed and a finite element method of measuring interfacial fracture toughness is delineated.

Fracture mechanics quantifies the critical combination of three variables namely applied stress, flaw size and fracture toughness. At material and structure interfaces, the critical size of a flaw also determines ultimate tensile strength. However, the strength definition of a material would be different if it were subjected to (a) uniform and (b) non-uniform stress distributions. This is especially true for brittle materials which are susceptible to fracture from initial defects and therefore, unreliable for carrying tensile loads. Monte Carlo simulations investigating interfacial failure under non-uniform stress fields are detailed in the fifth/final chapter.

CHAPTER II

A BIOLOGICALLY INSPIRED DESIGN FOR DISSIMILAR MATERIAL JOINTS

2.1. Introduction

2.1.1. Overview

Dissimilar material interfaces/joints can be found in numerous modern engineering and science fields, for example, adhesive bonded interfaces of two dissimilar materials; fiber/matrix interfaces of composite materials; thin film/substrate interfaces in micro-electromechanical systems (MEMS), to name a few. One major research effort in interface studies has been the interfacial strength evaluation of dissimilar materials (Drzal, 1990; Lara-Curzio et al., 1995; Rabin et al., 1998; Lin et al., 2001; Zhou et al., 2001; Xu and Rosakis, 2002a). Meanwhile, numerous studies have shown that failure often occurs along the interface/joint between two materials with high property mismatch (e.g., free-edge delamination in composite laminates and debonding between thin films/substrates), and that improving the interfacial properties (especially reducing the interfacial stress level) can modify overall material/structural behavior (Hutchinson and Suo, 1992; Needleman and Rosakis, 1999). Recent efforts also reveal that the chemical and mechanical aspects of interfacial bonding are essential for nano-structured material development (Thostenson et al., 2001). Indeed, interfacial bonding between the nano-scale reinforcement and the matrix is the most important subject in the development of nano-composite materials (Xu et al., 2004a).

However, macro-scale interfacial strength measurement is still a major challenge due to the stress singularity problem (Reedy and Guess, 1993; Tandon et al., 1999; Akisanya and Meng, 2003), i.e., the theoretical linear elastic stress will be infinite at the free-edge. It is necessary to develop reliable and quantitative measurements in order to characterize interfacial properties. As interfacial mechanical properties are intrinsic in nature, they are solely determined by the atomic structure and chemistry of the interfacial region (Swadener et al., 1999). However, the interfacial strength based on current measurements is not a material constant due to the free-edge stress singularity, according to some recent investigations (Reedy and Guess, 1993). Recently, Tandon et al., 1999, proposed a novel specimen design to measure the interfacial strength of fiber/matrix bonding. The key issue in measuring intrinsic interfacial strengths is the creation of a uniform interfacial stress state. So the first important step for intrinsic interfacial strength measurement is the elimination of stress singularities. The elimination of stress singularities is also required in structural/material joints subjected to fatigue and dynamic loading, since failure often occurs at the bi-material interface due to stress singularity (Pelegri et al., 1997; Xu and Rosakis, 2002a).

2.1.2. Objectives

The objective of this investigation is to propose a novel specimen/material design for removing the stress singularity, which yields reasonable interfacial strength measurement and delayed edge debonding of dissimilar material interfaces/joints. The following sections review the origin of stress singularities first and then propose a general solution inspired by tree mechanics. Typical metal/polymer joints will be selected as

examples for demonstration of the proposed new design through an integrated numerical and experimental investigation.

2.2. Theoretical background

2.2.1. Free-edge stress singularities in dissimilar material interfaces/joints

As illustrated in Fig. 2.1 (a), a butt-joint specimen was used to demonstrate the free-edge stress singularity in steel 4340 and Plexiglas (PMMA) joints (Xu et al., 2002b). Significant stress concentrations were found at the bi-material corners using the Coherent Gradient Sensing (CGS) technique, which was developed by Tippur et al., 1991, for full-field mechanical-optical measurements. The CGS fringe patterns correspond to the gradients of $\sigma_{xx} + \sigma_{yy}$. Figure 2.1(b) shows an Iosipescu shear test used to determine the interfacial shear strength of the same interface. Here too, a strong stress concentration caused by the free-edge stress singularity was observed. It is indeed this concentration/singularity that leads to free-edge debonding, which is often observed when the joint is subjected to dynamic and fatigue loading.

For some specific bi-material corners or edges, researchers (Williams, 1952; Bogy, 1971; Hein and Erdogan, 1971; Munz and Yang, 1993; Pageau et al., 1996; Akisanya and Meng, 2003; Klingbeil and Beuth, 2000; Labossiere et al., 2002) showed that stress singularities exist. The asymptotic stress field of a bi-material corner can be expressed by

$$\sigma_{ij}(r,\theta) = \sum_{k=0}^{N} r^{-\lambda_k} K_k f_{ijk}(\theta) \qquad (i, j = 1,2,3) \tag{2.1}$$

Here, $f_{ijk}(\theta)$ is an angular function and K_k is also called the "stress intensity factor".

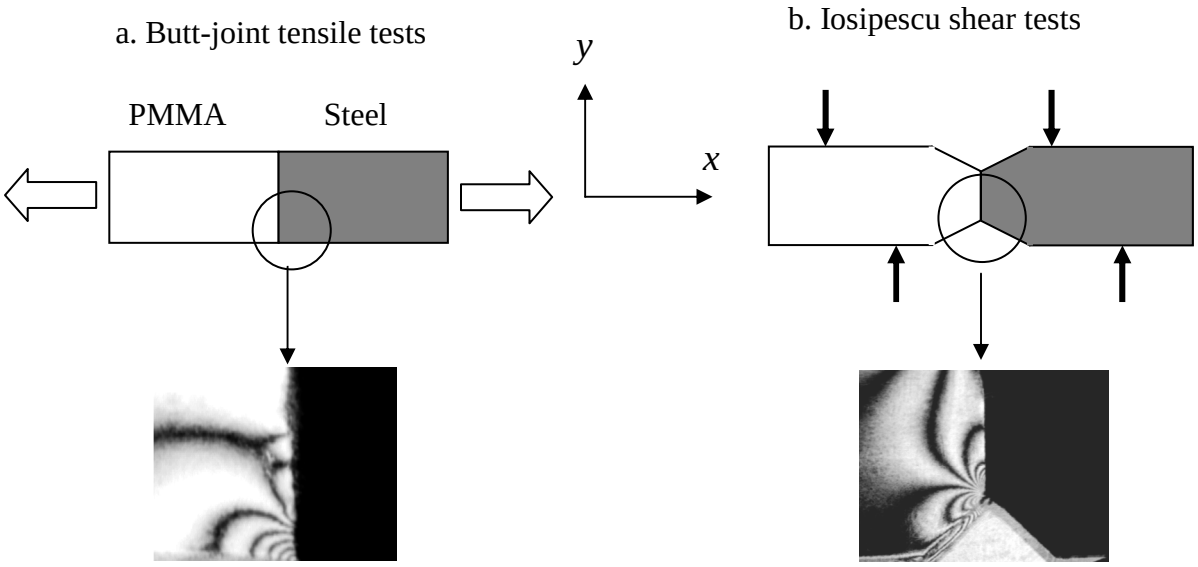

Fig. 2.1. Coherent Gradient Sensing (CGS) photographs showing strong stress concentrations (associated with fringe concentrations) at the free edges of bonded metals and polymers subjected to tensile and shear load (Xu et al., 2002b).

Although the fracture mechanics terminology "stress intensity factor" is used in interfacial mechanics to characterize a similar stress singularity problem, it should be noticed that for an interfacial fracture problem (assuming initial debonding), the stress singularity at a crack tip is intrinsic and cannot be removed. However, the stress singularity in interfacial strength investigation (assuming perfect bonding) can be removed through an appropriate material design: a key issue in this investigation. The stress singularity order λ may be a complex number. Hence the theoretical stress values will become infinite as r (defined in Fig. 2.2) approaches zero, if λ has a positive real part. This leads to a problem referred to as the "stress singularity problem". It is the presence of this stress singularity that leads to erroneous results in current interfacial strength measurements besides being responsible for free-edge debonding or delamination in dissimilar material joints.

However, if λ has a non-positive real part, then, the stress singularity disappears. Our major effort is focused on producing a non-positive real part for λ using a new interfacial design approach. There is yet another type of singularity in the form ln (r), which is weaker than the $r^{-\lambda}$ singularity (Chue and Liu, 2002) and this will not be of concern in this investigation. Bogy (1971) found that the stress singularity was purely determined by the material property mismatch and the two joint angles of the bi-material corner θ_1, θ_2 (defined in Fig. 2.2). Generally, the material property mismatch can be expressed in terms of the Dundurs' parameters α and β - two non-dimensional parameters computed from four elastic constants of two bonded materials (Dundurs, 1969):

$$\alpha = \frac{\mu_1 m_2 - \mu_2 m_1}{\mu_1 m_2 + \mu_2 m_1} \qquad \beta = \frac{\mu_1 (m_2 - 2) - \mu_2 (m_1 - 2)}{\mu_1 m_2 + \mu_2 m_1} \tag{2.2}$$

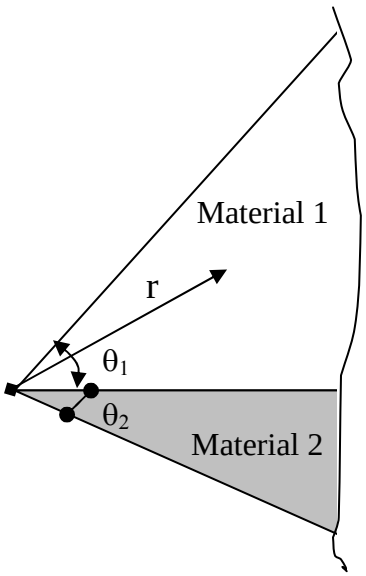

Fig. 2.2. Angular definitions at bi-material corners or edges.

Here μ_1 is the shear modulus of material 1, μ_2 is the shear modulus of material 2, v is the Poisson's ratio, $m = 4(1-v)$ for plane strain and $m = \frac{4}{1+v}$ for generalized plane stress.

The stress singularity order is related to material and geometric parameters, and is determined by a characteristic equation of coefficients A (θ_1, θ_2, p) — F (θ_1, θ_2, p):

$$f(\theta_1, \theta_2, \alpha, \beta, p) = A\beta^2 + 2B\alpha\beta + C\alpha^2 + 2D\beta + 2E\alpha + F = 0 \tag{2.3}$$

Where p=1-λ. A, B, C, D, E and F are expressed as following (Bogy, 1971):

$$\begin{aligned}
A(\theta_1, \theta_2, p) &= 4K(p, \theta_1)\,K(p, \theta_2), \\
B(\theta_1, \theta_2, p) &= 2p^2\sin^2(\theta_1)\,K(p, \theta_2) + 2p^2\sin^2(\theta_2)\,K(p, \theta_1), \\
C(\theta_1, \theta_2, p) &= 4p^2(p^2 - 1)\sin^2(\theta_1)\sin^2(\theta_2) + K[p, (\theta_1 - \theta_2)], \\
D(\theta_1, \theta_2, p) &= 2p^2[\sin^2(\theta_1)\sin^2(p\theta_2) - \sin^2(\theta_2)\sin^2(p\theta_1)], \\
E(\theta_1, \theta_2, p) &= -D(\theta_1, \theta_2, p) + K(p, \theta_2) - K(p, \theta_1), \\
F(\theta_1, \theta_2, p) &= K[p, (\theta_1 + \theta_2)]
\end{aligned} \tag{2.4}$$

Where the auxiliary function K (p, x) is defined by

$$K(p, x) = \sin^2(px) - p^2\sin^2(x) \tag{2.5}$$

Therefore, our basic idea is to vary these four independent parameters $(\theta_1, \theta_2, \alpha, \beta)$ in order to obtain a negative real value of the stress singularity order λ. As such, the stress distribution close to the free edge is not expected to be very sharp.

2.2.2. Convex interfacial joints for uniform interfacial stress distribution

The first step to establish a uniform stress state at the interface is to reduce or eliminate the stress singularity at the bi-material edge. Mattheck (1998) analyzed an interesting problem of a tree/steel railing interface as illustrated in Fig. 2.3.

His finite element analysis showed that for a total joining angle $\theta_1 + \theta_2 = 270^o$, the Mises stress has a concentrated value at the joint corner. A better design is the naturally formed convex shape, which corresponds to the optimized case shown in Fig. 2.3. As recently noticed by Mohammed and Liechti, 2001; an appropriate joining angle design at the bi-material edge may be a possible approach to reduce stress singularity, although they did not propose a general principle. In this paper, the joint angle design is based on the determinant $f(\theta_1, \theta_2, \alpha, \beta, p)$ introduced by Bogy, 1971. Since appropriate angular combinations can be selected according to different material combinations, a negative or zero value for Re[λ] is possible to obtain. Interpreted, that means that the degree of singularity can be reduced or removed. From this step, two joint angles θ_1 and θ_2 can be determined (as shown in Fig. 2.2).

A special example was examined as shown in Fig. 2.4. For a polycarbonate (PC) - aluminum (Al) interface/joint, the stress singularity order λ of value -0.01 can be obtained if the two interfacial joint angles fall within the zones marked by the designated curves using equation (2.3). This would mean elimination of stress singularity and the existence of a relatively uniform stress distribution at the PC/Al interface.

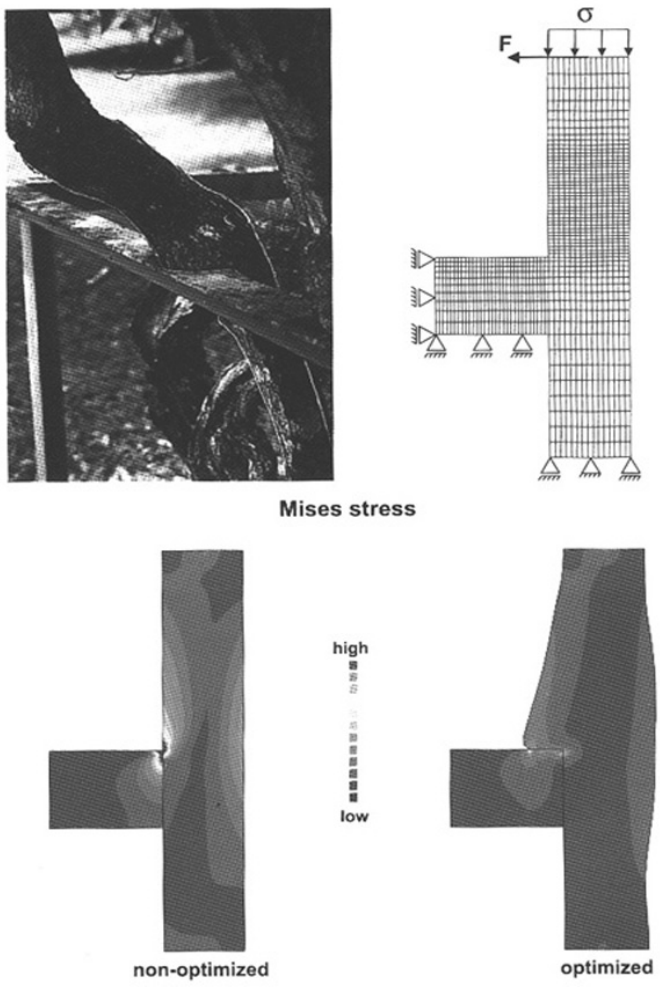

Fig. 2.3. Finite element stress analysis and corner optimization of a tree-steel railing interface/joint (Mattheck, 1998). The natural convex joint shows no stress concentrations/ singularities.

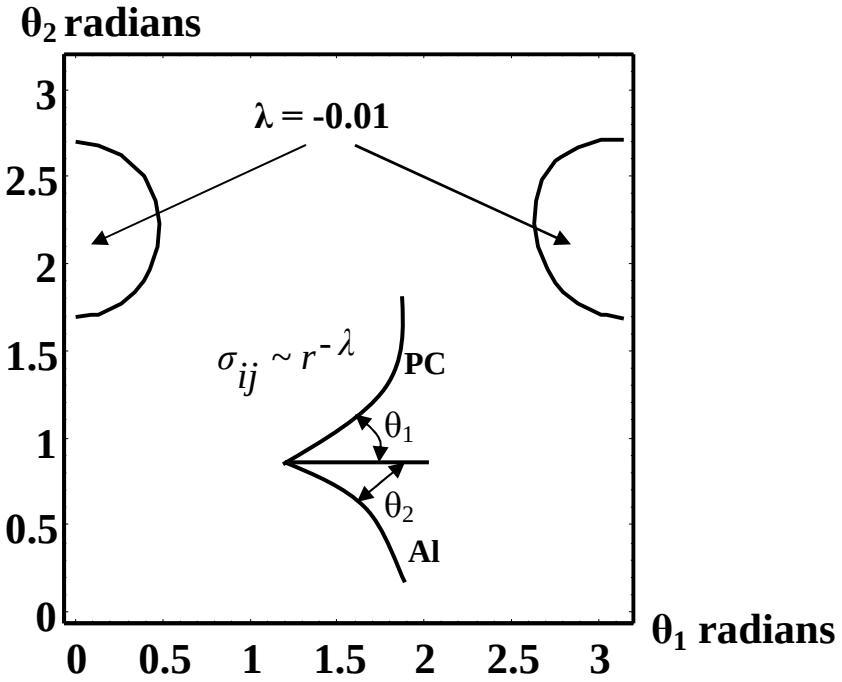

Fig. 2.4. A contour plot of possible joint angles without stress singularities for an aluminum-polycarbonate interface.

Here, a generalized plane stress case was considered in computing the Dundurs' parameters, α = -0.935 and β = -0.308. These results posed a more general question: is it possible to determine a specific convex joint pair with least stress singularities for a wide range of engineering material combinations? According to our numerous case studies, if an interfacial design is chosen with two joint angles: θ_1 = 45^o and θ_2 = 65^o and it is assumed that material 1 is a typical soft material and material 2 is a hard material then, there will be no stress singularity for a wide range of current engineering materials.

This result is illustrated in Fig. 2.5 for the entire possible range of two Dundurs' parameters (Hutchinson and Suo, 1992). It will be noticed that for this specific pair of joint angles, the stress singularity is limited to a very small zone near $\alpha \cong 1$. These extreme material joint combinations are quite rare in engineering applications since they represent extremely high mismatch in Young's moduli. Recent examples include nanotube/nanofiber reinforced polymer composites - the Young's modulus of carbon nanotubes is as high as 1000 GPa. Xu et al. (2004a) have reported a value of $\alpha \cong 0.99$ for a new nanofiber/epoxy composite. In recent studies on the stress singularity at an axisymmetric bi-material interface subjected to torsion load, Liu et al. (1999) found that the stress singularity order λ could be obtained from a simple characteristic equation. They also showed that there are no oscillatory stress singularities for this type of problem because all roots of λ are real. Also, if $\theta_1 = \theta_2$, as shown in Fig. 2.2, the stress singularity will depend on one joining angle only rather than the material property mismatch. One striking result from their research is that the stress singularity disappears as soon as θ_1 ($=\theta_2$) <90^o (convex joint). Hence, there is no stress singularity at the bi-material edge for the axisymmetric specimen subjected to torsion load. This is the exact

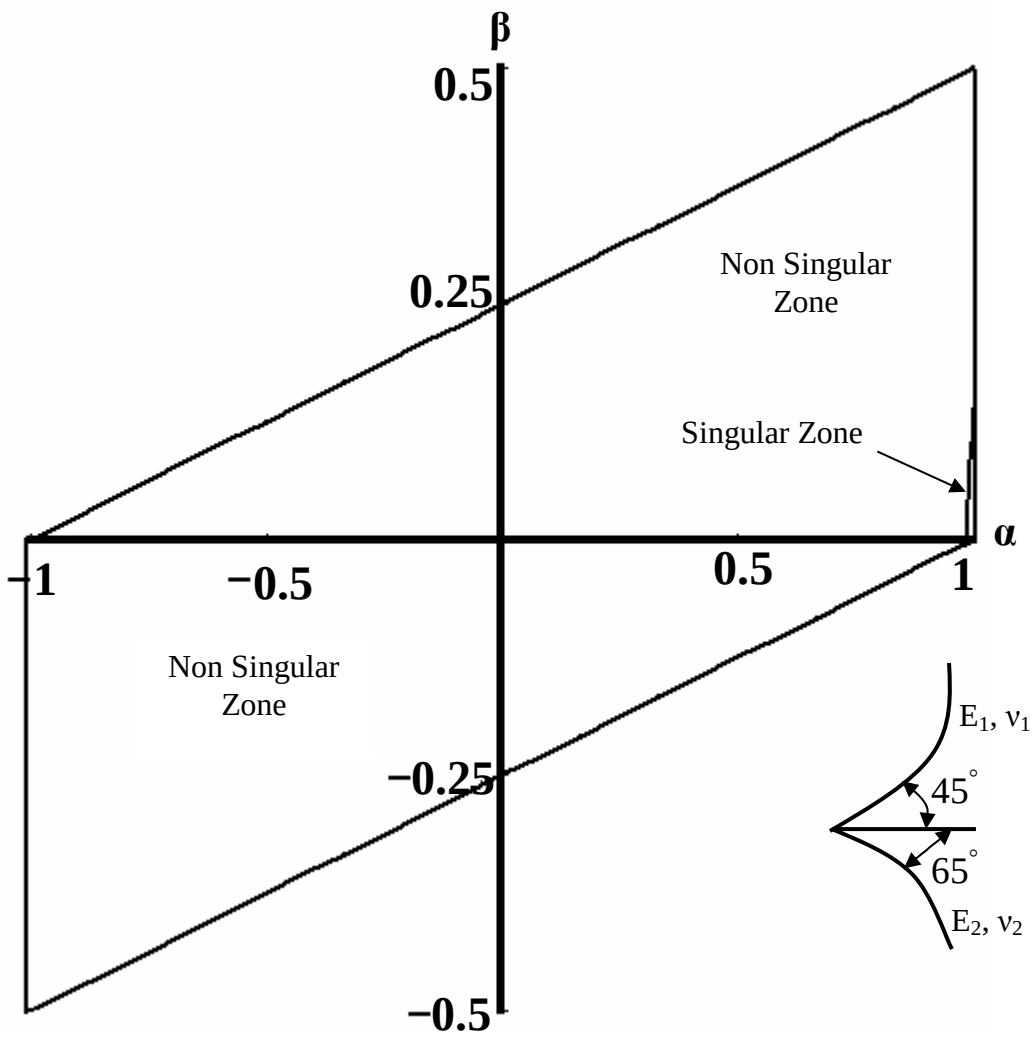

Fig. 2.5. Stress singularity order λ as a function of two Dundurs' parameters for a proposed pair of joint angles (45 and 65 degrees for soft and hard materials respectively). A very small singular zone implies the given pair of angles is applicable for a wide range of engineering material combinations.

theoretical foundation for a naturally optimal convex tree shape. The second step is to seek a contour design for obtaining a uniform stress distribution along the interface. Mattheck (1998) used an example of a buttress root to demonstrate the optimal contour design for a uniform stress distribution. A gradual transition in contour has generally been observed in tree roots. This underlying natural principle will be employed and simplified in the following example of typical metal/polymer joints.

2.3. Numerical and experimental investigation

2.3.1. Experimental findings and implications

Plane joints of polycarbonate-aluminum and PMMA-aluminum interfaces were tested using in-situ photoelasticity technique, and experimental results showed that failure load values of the same interface with different edge shapes were quite different. In order to understand the mechanics insight, a numerical investigation will be very necessary since the photoelasticity method mainly provides information of a two-dimensional stress state. Indeed, in modern experimental studies, integrated numerical simulations not only validate experimental results, but also reduce possible errors inherent in experimental setups. In this investigation, a two-dimensional finite element analysis will be conducted to verify and compare stress changes in the convex plane-joints to experimental findings. However, three-dimensional finite element analysis shows that the stress singularity along the thickness direction still exists. So, a convex axisymmetric joint will be proposed to provide reasonable interfacial strength measurements.

2.3.2. Finite-element modeling

Elastic finite element analysis of the baseline and the proposed convex metal-polymer (aluminum-polycarbonate) joint specimen was carried out employing the commercial software ANSYS. The dimensions of the baseline specimen (straight-edge, Fig. 2.6 (a)) were: length L= 254 mm, half width W= 19.05 mm, thickness 2T = 6.35 mm for thin specimens and 9.2 mm for thick specimens. In this investigation, four different joint types, with the same bi-material combination and equal bonding area, were subjected to the same in-plane tension load as shown in Fig. 2.6. One was the traditional butt-joint specimen with straight free-edges (Fig. 2.6(a)). It was expected that severe stress singularities would be observed at the free-edge in this baseline specimen. The second specimen had convex edges with proposed interfacial joint angles, as seen in Fig. 2.6(b). It should be mentioned here that our proposed new joint design reduced the material volume by at least 15% around the interfacial joint area. Greater reduction in total material volume would be attained if the area away from the interface were accounted for. The third specimen was a straight cylinder with free edges as shown in Fig. 2.6(c). This was used to illustrate the advantage of the convex edges of Fig. 2.6(d) over the straight edges of Fig. 2.6(c). The fourth specimen, as illustrated in Fig. 2.6(d), was an axisymmetric design with convex edges. Equating the interfacial bonding area of Fig. 2.6(d) to that of the three-dimensional non-axisymmetric specimen (Fig. 2.6(b)) yielded the radius of the axisymmetric specimen.

A detailed illustration of the mesh used for the convex plane-joint is shown in Fig. 2.7, where the gradual change in element size, from coarsely to finely meshed regions, may be noticed. Taking advantage of symmetry, only half of the specimen was modeled.

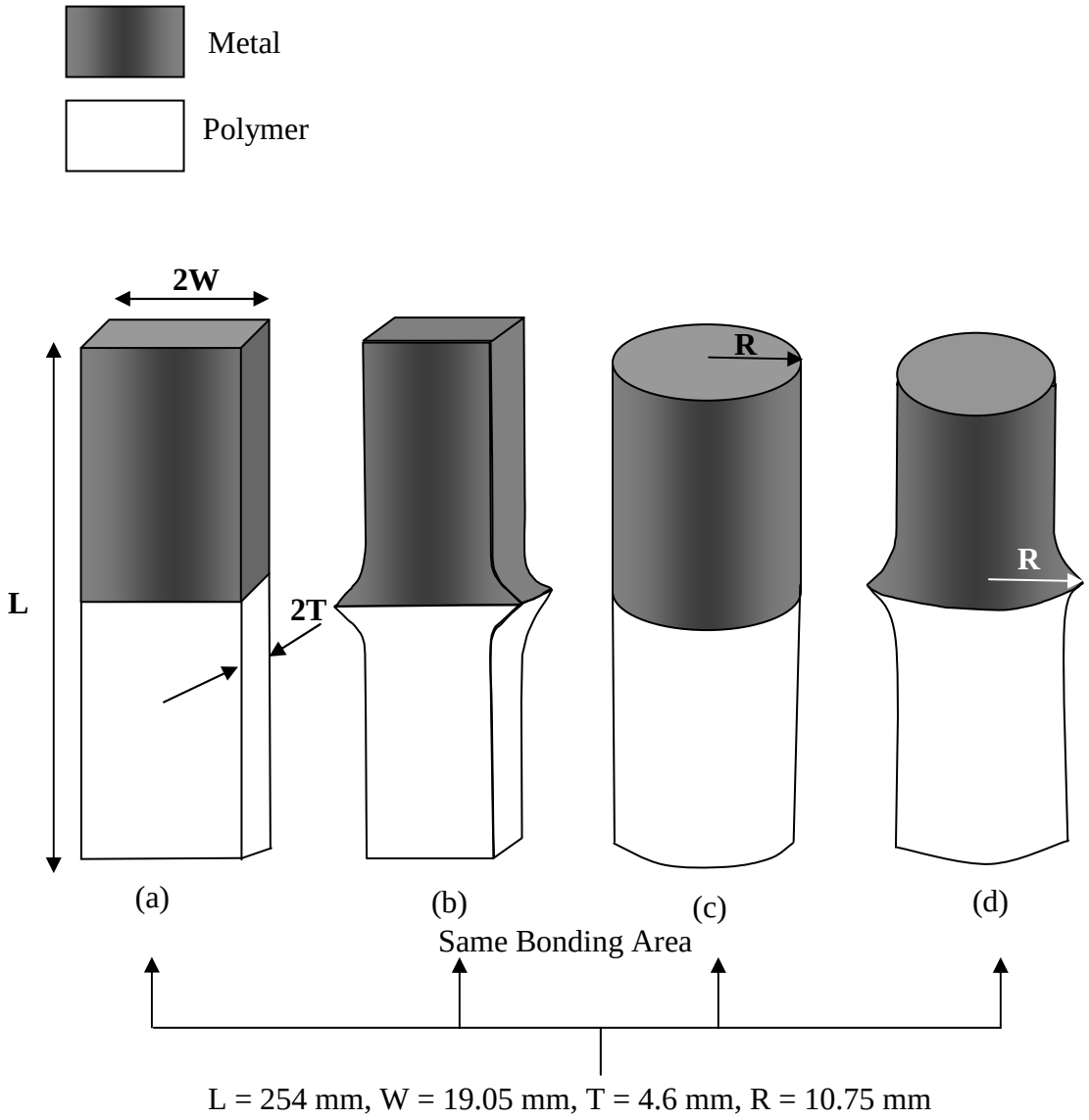

Fig. 2.6. Schematic diagrams of aluminum-polycarbonate joint specimens with (a) straight edges (baseline) (b) shaped edges with least stress singularities (c) axisymmetric design of straight edge specimen (d) axisymmetric design of shaped edge specimen.

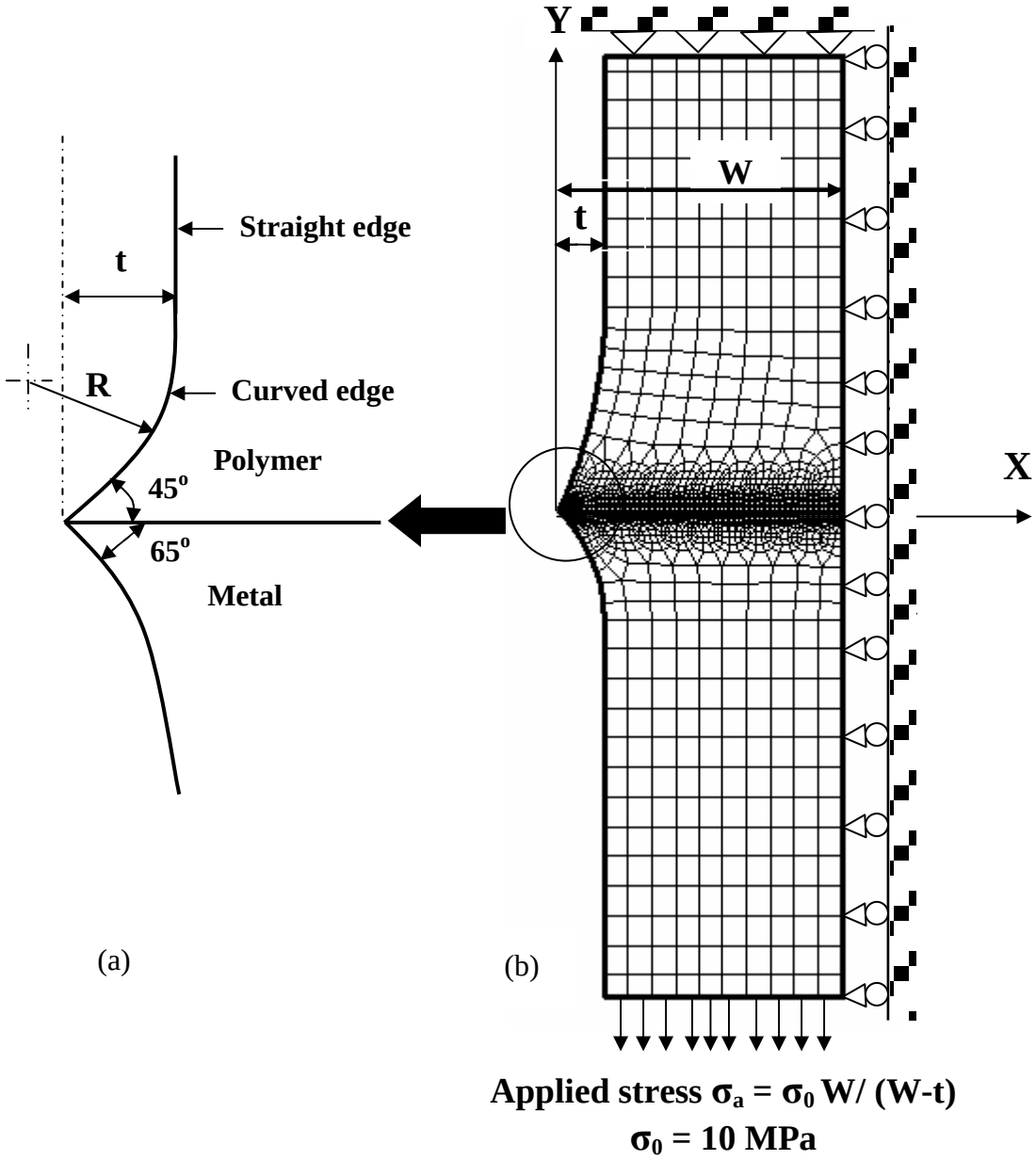

Fig. 2.7. (a) Illustration of a proposed convex joint of metal and polymer interface (b) Finite element mesh and boundary conditions of the new joint subjected to in-plane tensile load. Notice that the applied stress at the specimen end is a function of t such that the average tensile stress at the interface is always 10 MPa. W = half-width of the specimen.

The transition from the straight edge to the curved edge at the interface corner was achieved by means of a circular arc of radius R = {t/ (1 - Sin (θ))}, where θ is the joining angle and t is the convex extension distance as illustrated in Fig. 2.7(a). Roller boundary conditions were applied along the mid-plane of the specimen, i.e., at x=W. The finite element mesh consisted of PLANE 42 elements (2D four-noded element) and finer subdivisions were employed in regions where the stress gradient was expected to be high such as the interface corner and the entire length of the interface.

For the straight-edged specimens, the element length ranged from a maximum of 0.1W to a minimum of 0.000407W.While the maximum element edge length was retained in meshing the convex specimens, the smallest element length was changed to 0.000794W in order to utilize the same meshing pattern for both the shaped and baseline (straight-edge) specimens. The FE model was loaded by applying tension to the edge parallel to the x-axis at y = -127 mm. The edge at y = 127 mm was specified with zero displacement boundary conditions in the y-direction.

In assuming that the same total load at the interface area was transferred to both baseline and shaped specimens, the stress applied to the shaped specimen was obtained by multiplying the stress σ_0 (stress applied to the baseline specimen) by a factor of W/ (W-t). The stiffness properties for aluminum were chosen as E = 71 GPa, $\nu = 0.33$ and for polycarbonate, E = 2.4 GPa, $\nu = 0.34$.

A similar approach was taken for the three-dimensional analysis of the same convex plane-joint (Fig. 2.6(b)) except that the two-dimensional mesh was extruded in the Z-direction to achieve the thickness of the specimen. While 2-D plane stress elements (PLANE42) and 2-D axisymmetric elements (PLANE42) were used for modeling the

two-dimensional plane stress and axisymmetric models respectively, iso-parametric quadrilateral 20-node SOLID95 elements were used to construct the three-dimensional model. Taking advantage of symmetry, a quarter of the model was analyzed in 3-D analysis. Sub-modeling was utilized in the three-dimensional design to ensure a fine mesh in the close vicinity of the bimaterial interface.

2.4. Results and Discussion

2.4.1. Influence of geometrical shapes and material properties

In order to validate our numerical analysis results, we compared the stress singularity order, λ, obtained from the finite element analysis and from Bogy's formula. The approach adopted here is similar to that described by Munz and Yang, 1993. An aluminum-polycarbonate interface with joining angles of 90^o- 90^o was considered and the results have been illustrated in Fig. 2.8. On applying 10 MPa stress in the Y-direction, the interfacial normal stresses and shear stresses were plotted as functions of the ratio r/W. Here, r is the distance from the interface corner and W is the half-width of the specimen. According to the defining relation between λ and the stresses at the interface (Xu et al., 2004b), the slopes of these respective plots should yield the value of λ. From Fig. 2.8, it is seen that the slope as obtained from the interfacial normal stress plot was equal to 0.223 and the slope of the interfacial shear stress plot was 0.216. The analytical value of λ based on Bogy's formula is 0.225 for these specific materials and angle joints. These three values are quite close and hence we shall use the same tool and procedure to analyze the proposed convex joints.

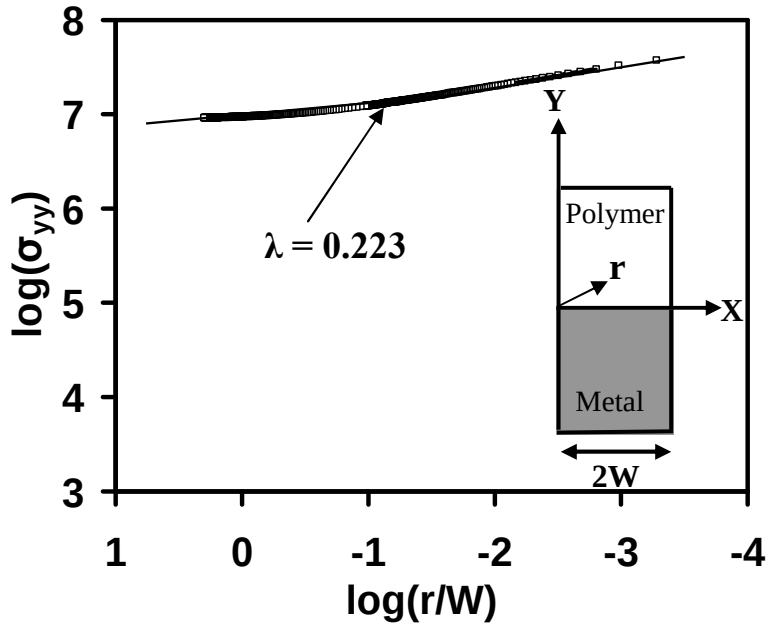

(a)

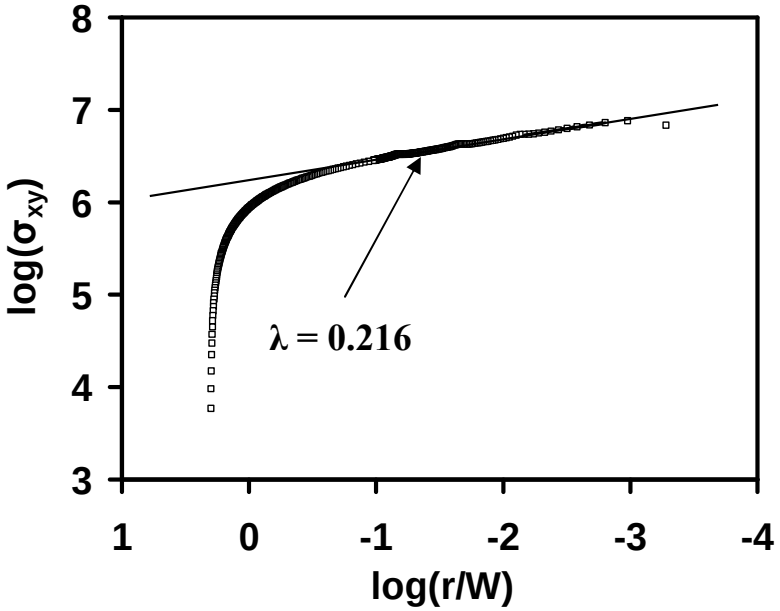

(b)

Fig. 2.8. Comparison of the stress singularity order λ obtained from the finite element analysis and Bogy's formula for an Al-PC joint with straight edges (a) FEM interfacial normal stress distribution close to free edge and fitted λ value (b) FEM interfacial shear stress distribution close to free edge and fitted λ value. Theoretical λ= 0.225.

The main parameters that have been varied in our finite element analysis are (a) convex extension distance t (b) joining angles and (c) elastic constants of the constituent materials. The influence of the geometrical parameters, on the stress distribution at the interface, has been illustrated in Figs. 2.9 and 2.10. Four cases have been examined for t = 0 (straight-edge or baseline specimens), 0.5, 1.0 and 3.0 mm. For zero extension distance, i.e., straight-edge specimens, a prominent stress singularity is seen at the bimaterial corner.

However, for increasing extension distances, the interfacial normal stress and shear stress have finite values at the interface corner and their respective distributions are seen to smoothen out over the interface to uniform values. From this analysis, we find that the free-edge stress singularity is successfully removed and the convex extension distance t mainly affects local stress distributions close to free-edges. Since stress singularity directly contributes to free-edge delamination or debonding, this results in a corresponding increase of the load transfer capability of the new joint as long as we use the specific convex joint.

However, convex specimens may not be accurately machined. So a natural question arises: whether we should use the exact interfacial joint 45^o-65^o angle combination only? Figure 2.10 is significant in that while only the 45^o angle of the polycarbonate part was retained and the joint angle of the aluminum part was varied from 45^o to 90^o, the stress singularity was still effectively removed.

This example, along with similar other numerical case studies, essentially pointed to the fact that as long as the sum of two joint angles is less than 180^o and each joint angle is less than 90^o, the stress singularities will be reduced.

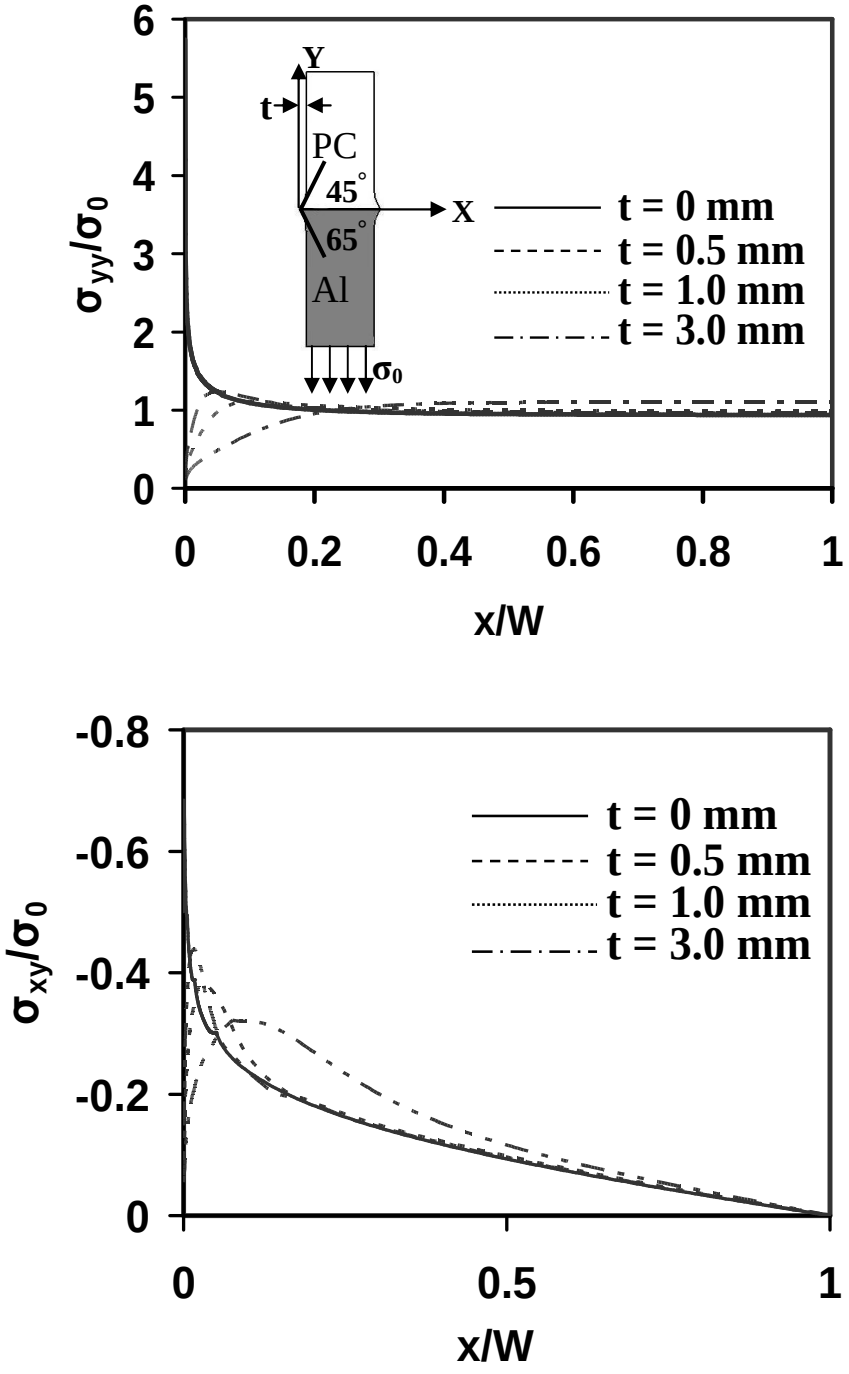

Fig. 2.9. Variations of (a) interfacial normal stress and (b) interfacial shear stress with different extension distances (fixed joint angles θ_1 (for polycarbonate) = 45°, θ_2 (for aluminum) = 65°). If t=0 (straight edge), stresses are singular at the free edges.

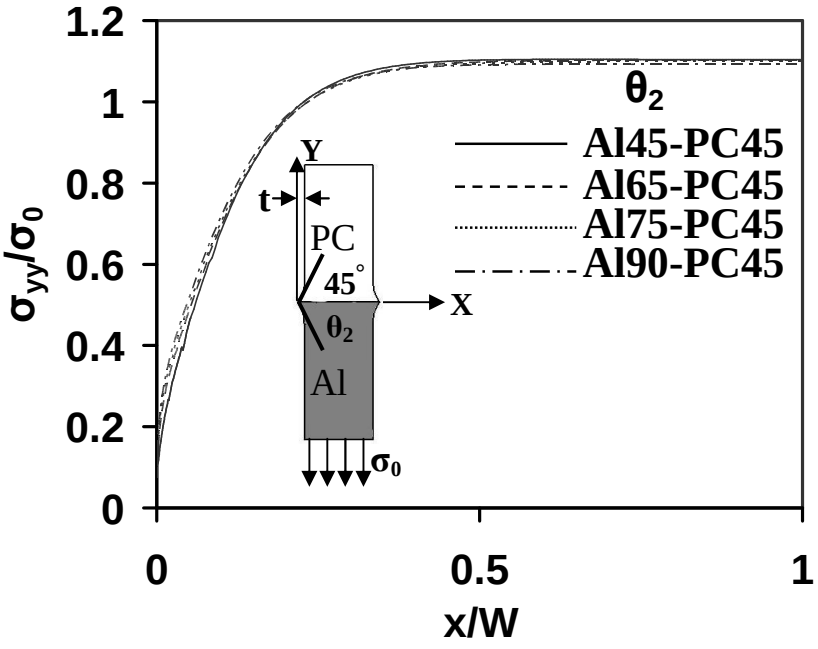

Fig. 2.10. Variation of normalized interfacial normal stress with the joint angle of aluminum (fixing the joint angle of PC at 45 degrees, t = 3mm).

In other words, stress singularity is successfully removed for the 45^o-65^o angle combination in theory but in reality, for a slight deviation from this combination, the stress singularity would be reduced if not removed absolutely. Our next question therefore is: would this statement hold true for most of the material combinations as shown in Fig. 2.5?

The influence of material properties on the reduction of stress singularity was examined by retaining the polycarbonate half of the tensile joint specimen and varying the Young's modulus of the other material. Four cases were chosen for E_2= 2.4 GPa, 10 GPa, 71 GPa, 200 GPa and the results have been illustrated in Figs. 2.11(a) and 2.11(b). Results show that while the interfacial normal stress distribution smoothened out over the interface, the interfacial shear stress distribution dipped within 15% of the distance from the joint tip. However, the normal and shear stresses were very near to zero at the interface corner, which has a direct impact on higher load transfer capacity since the interface would be less likely to fail at low load as compared to conventional straight-edged specimens. These numerical results verified the theoretical results shown in Fig. 2.5 and so these convex joints are effective in removing stress singularities for most engineering material combinations.

2.4.2. Comparison of numerical analysis with experimental results

Full-field photoelasticity was employed to make a direct comparison with the finite element simulation. Figures 2.12 and 2.13 bear the most conclusive testimony to the reduction of stress singularity at the interface of dissimilar materials. The photoelastic

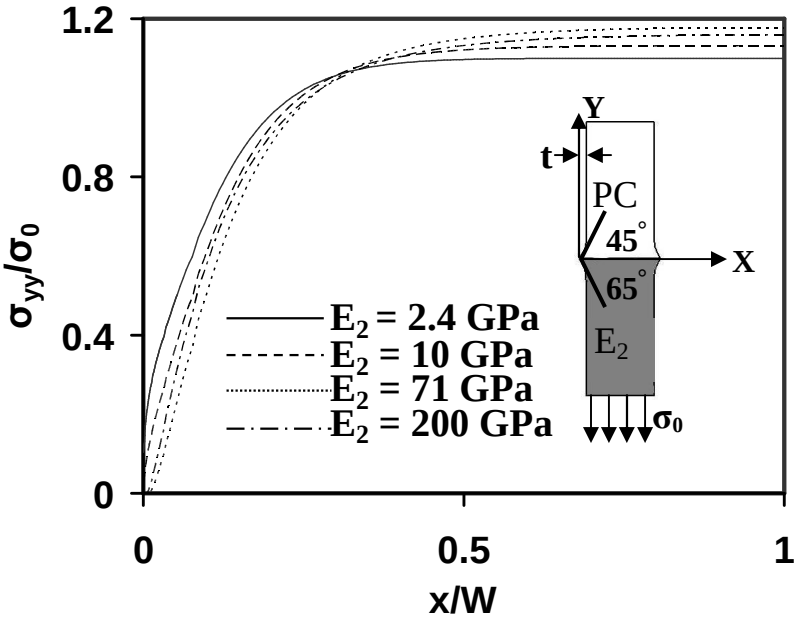

(a)

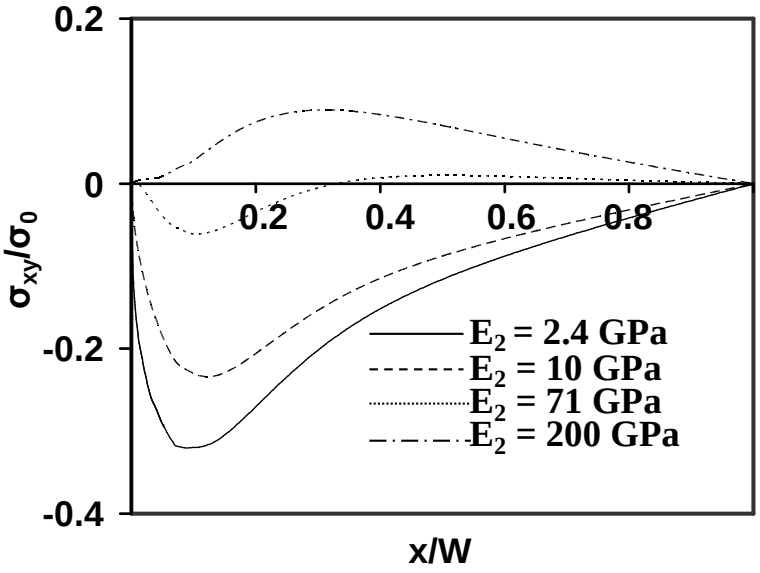

(b)

Fig. 2.11. (a) Variation of interfacial normal stress and (b) variation of interfacial shear stress with different material properties (keeping polycarbonate the same, t = 3 mm).

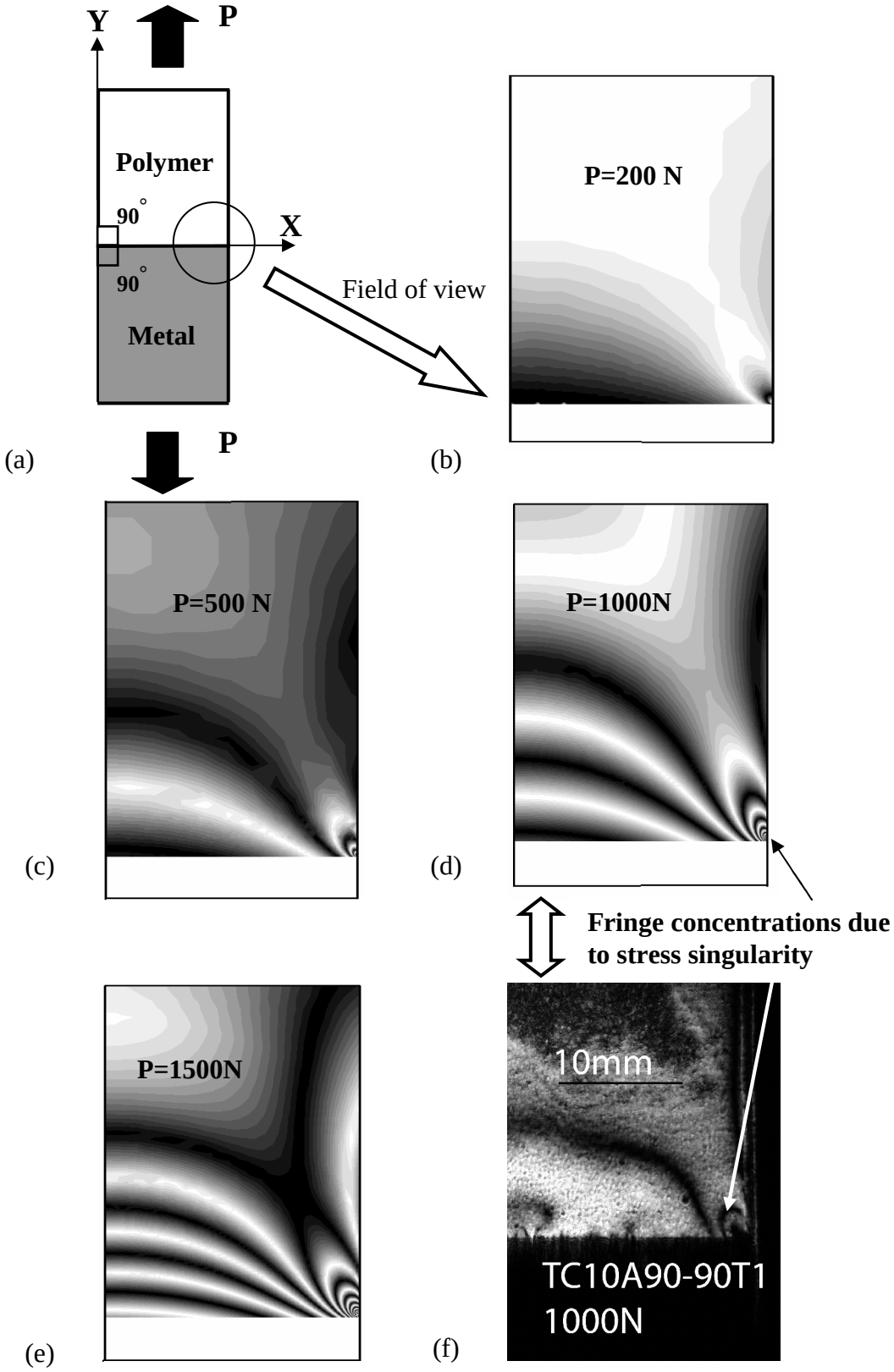

Fig. 2.12. Development of numerical photoelasticity patterns for load P= (b) 200 N (c) 500 N (d) 1000 N (e) 1500 N and (f) experimental photoelasticity pattern for a typical PC/Al joint with straight edges under P=1000 N.

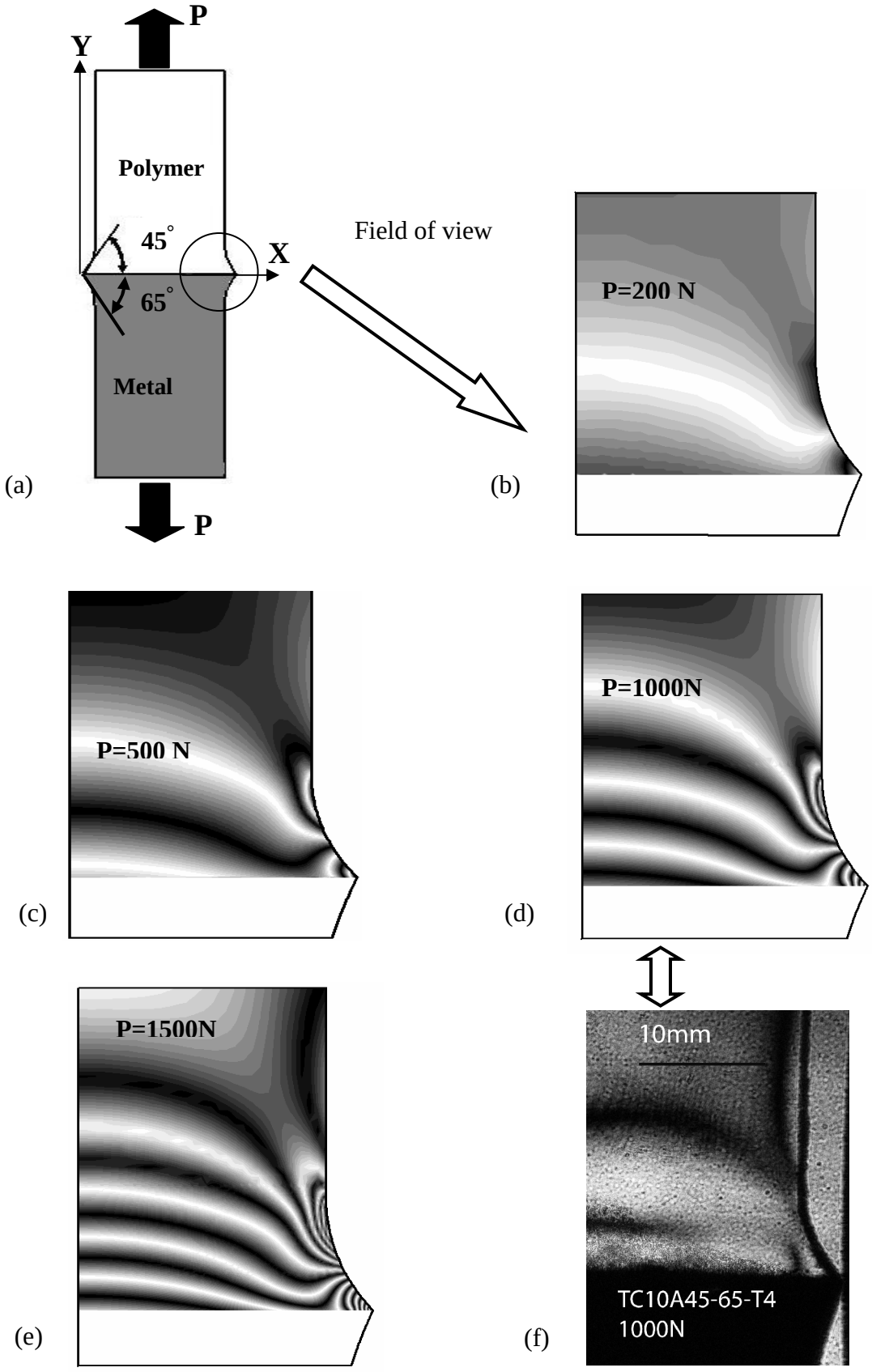

Fig. 2.13. Development of numerical photoelasticity patterns for load P=(b) 200 N (c) 500 N (d) 1000 N (e) 1500 N and (f) experimental photoelasticity pattern for a typical PC/Al joint with shaped edges under P= 1000 N.

fringe patterns are contours of the maximum in-plane shear stress according to the classical photoelasticity equation:

$$\tau_{\max} = (\sigma_1 - \sigma_2)/2 = \frac{Nf_\sigma}{2h} \tag{2.6}$$

Where σ_1 and σ_2 are in-plane principal stresses, N is the fringe order, f_σ is the stress-fringe constant (7 kN/m for polycarbonate) and h is the specimen thickness. After the fringe order N was computed at every node using Equation (2.6), a corresponding gray-scale value was calculated by associating a gray-scale value of 255 with full fringe orders (e.g., 0, 1, 2 etc) and a value of 0 with half fringe orders (e.g., 0.5, 1.5, 2.5 etc).A plotting software Tecplot 9.2 was then used to plot these gray-scale values, and the numerical fringe patterns shown in Figs. 2.12 and 2.13 were generated for stress field visualization and comparison with experimental results.

It is rather interesting to note that a clear fringe concentration originates at the interface corner for straight-edged specimens with increasing load, as shown in Fig. 2.12. This type of fringe concentration is a result of the free-edge stress singularity and is very similar to the fringe concentration caused by a bi-material interfacial crack (Xu and Rosakis, 2002a). It is noticed that the stress singularity order for Al/PC joints is around –0.2 and can be eliminated, but for interfacial cracks, the stress singularity order is $-0.5+i\varepsilon$ (Barsoum, 1988; Rice, 1988; Hutchinson and Suo, 1992) and is intrinsic. A direct comparison of the numerical fringe pattern (Fig. 2.12(d)) and the experimental pattern (Fig. 2.12(f)) of the specimen subjected to the same applied load of 1000 N verifies the existence of stress singularity at the free edge.

The accumulation of fringes at the bimaterial interfacial corner, seen in the straight-edged specimens, completely disappeared in the numerical fringe patterns for the

convex specimen as seen in Fig. 2.13. The experimental fringe pattern also validates this result as shown in Fig. 2.13(f). The highest fringe order actually went up to 23.5 for the straight-edged specimens whereas the highest fringe order in the shaped specimens under the same applied load (P=500 N) was only 6.5. This is a clear indication that the stress intensity has decreased by several orders in the proposed convex joint. It is noticed that the higher fringe orders signifying larger stress intensity move away from the free-edge towards the polycarbonate curved edge.

This stress re-distribution is indeed very important in interfacial joint designs since the bonding strength of the interface is generally lower than that of the bulk material (adherend). For example, the tensile strength of bulk polycarbonate is at least 60 MPa whereas the nominal interfacial tensile strength of PC/Al joints in this investigation is around 5-6 MPa. It may be noticed that the number of fringes in Fig. 2.13(d) and 2.13(f) do not match exactly although the general pattern of stress evolution is distinctly similar. This is because a finite element simulation assumes ideal conditions unlike the actual in-situ experiments conducted. As a result of reduction of the free-edge stress singularity, experiments conducted on PMMA-aluminum and polycarbonate-aluminum convex shaped specimens showed a marked increase in nominal tensile strengths (ultimate load/interface area) over those of straight-edged specimens (Xu et al., 2004b). Another interesting experimental phenomenon is the influence of specimen thickness which has also been considered for polycarbonate-aluminum joints. It was also noticed that thicker specimens (thickness 9 mm) showed less tensile strength increase than thin specimens (thickness 6 mm) (Xu et al., 2004b). This raises an important issue in the convex plane-joint since the free-edge stress singularity still exists around the thickness

direction although it was removed along specimen width direction. This problem can be solved by a simple axisymmetric design.

2.4.3. An axisymmetric convex joint for intrinsic interfacial strength measurements

The convex plane-joint was employed in the first part of this investigation simply because it can be used in direct comparison with in-situ stress visualization techniques such as photoelasticity. However, careful three-dimensional stress analysis revealed that the removal of free-edge stress singularities is not complete. Figure 2.14 depicts the distribution of normal and shear stresses of the polycarbonate-aluminum interface along width and thickness directions. The substitution of straight interface ends by convex angles has rendered a smooth stress distribution, without any sign of stress singularity along the width (X-direction). This same conclusion was reached in the two-dimensional finite element analysis of the same specimen (Fig. 2.9). One may conclude that Fig. 2.14(a) could be smoother (with a finer mesh) although the basic nature of the stress distributions would still be the same. The reason a finer mesh could not be employed is attributed to the limitation of the finite element analysis tool used for this purpose.

It is not surprising that Fig. 2.14(b) shows that the stress singularity in the thickness direction still exists. This is because although the specimen was given a convex shape in the X-Y plane, the stress singularity in the Y-Z plane still persisted due to the existing straight edges. An obvious solution to this problem would be an axisymmetric design where a convex shape is imparted to the entire circumference of the bi-material interface. An axisymmetric convex joint, which is naturally similar to a tree/bamboo shape, will be employed to measure the intrinsic interfacial strength.

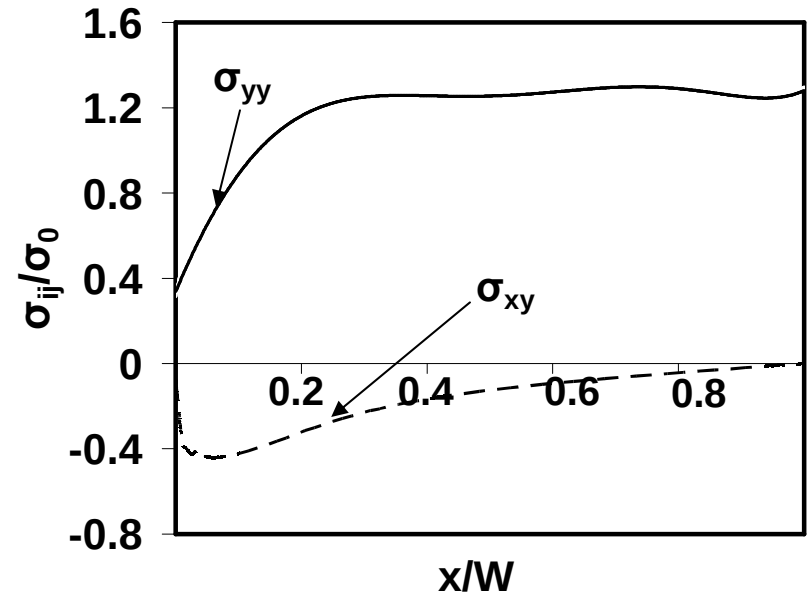

(a)

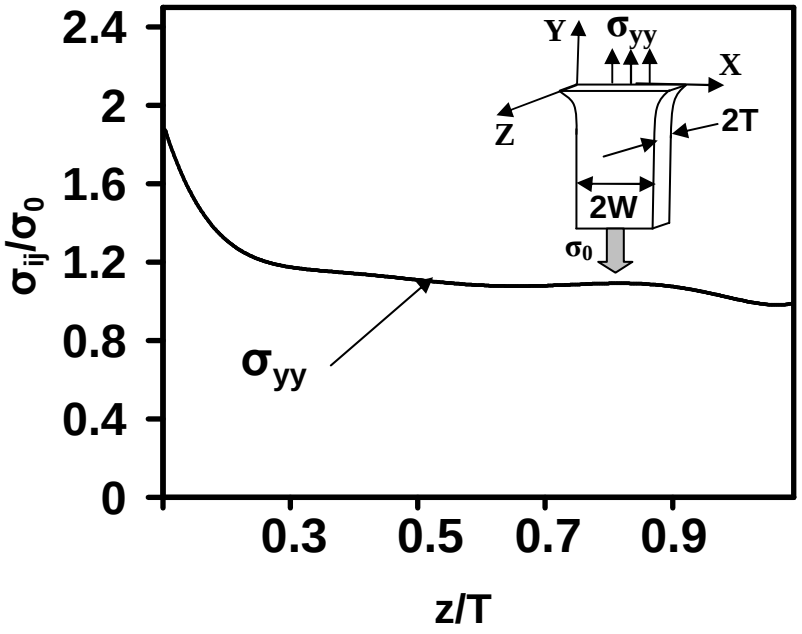

(b)

Fig. 2.14. (a) Variation of interfacial normal stress and shear stress in 3D finite element model along width (b) variation of interfacial normal stress in 3D finite element model along thickness (t = 3 mm).

Figures 2.15(a) and (b) compare the interfacial stress states in an axisymmetric cylindrical specimen with convex interfacial joints to that in an axisymmetric cylinder with straight edges. Singular stresses are normally expected close to the specimen free-edge as shown in Fig. 2.15(a) for the reference purpose of stress state comparison. This impedes us from obtaining an intrinsic interfacial strength. However, Fig. 2.15(b) clearly shows that stress singularities are eliminated if the axisymmetric design is used in future specimen design. To validate these stress states, more advanced experimental investigations should be conducted (Rabin et al., 1998) since traditional experimental stress analysis techniques, such as photoelasticity, face difficulty in depicting sharp three-dimensional stress change in a small zone close to the specimen free-edge. On the other hand, final tensile strength increase was predicted for the convex axisymmetric specimen over the straight cylindrical joint even before actual experiments were conducted.

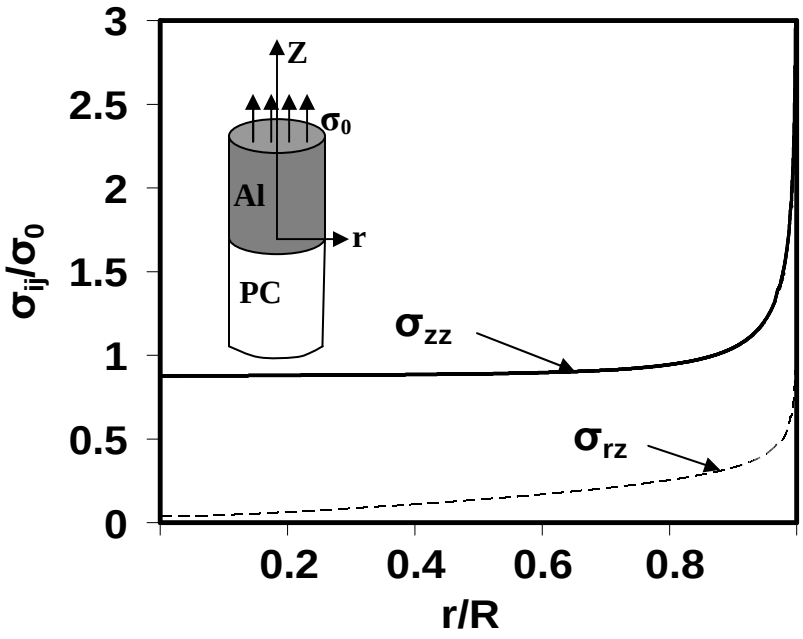

(a)

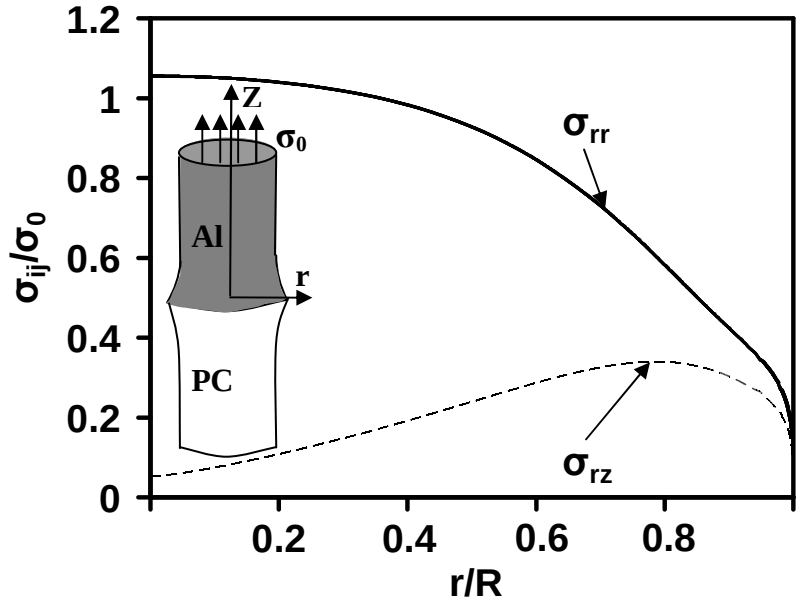

(b)

Fig. 2.15. (a) Variation of interfacial normal stress and shear stress in unshaped axisymmetric finite element model and (b) variation of interfacial normal and shear stress in shaped axisymmetric finite element model (t = 3 mm).

2.5. Conclusions

Finite element analyses on two-dimensional plane-stress, axisymmetric and full three-dimensional specimens were conducted in this investigation. The results were interesting in that the two-dimensional plane-stress specimens were devoid of stress singularities along the specimen width although the free-edge stresses along thickness direction were still singular. An axisymmetric design was shown to eliminate stress singularities along the periphery of the bi-material interface. This should lead to increased load transfer capability of the new joints and hence the convex axisymmetric specimen is expected to yield intrinsic interfacial tensile strength measurements.

CHAPTER III

INTERFACIAL STRESS TRANSFER IN NANOFIBER COMPOSITE MATERIALS

3.1. Introduction

Carbon nanotubes have extraordinary mechanical properties and tend to be used as reinforcements in polymers and other matrices to form so-called "nanocomposite materials" (Treacy et al., 1996; Lau and Hui, 2002; Qian et al., 2002; Luo and Daniel, 2003; Wagner et al., 1998; Qian et al., 2000; Yu et al., 2000; Schadler et al., 1998; Odegard et al., 2003; Thostenson et al., 2001). Nanocomposites are a novel class of composite materials where one of the constituents has dimensions in the range of 1-100 nm. It has been reported (Wagner et al., 1998) that load transfer through a shear stress mechanism was seen at the molecular level. Nanotubes increase composite strength by as much as 25% (Qian et al., 2002; Yu et al., 2000). Alternative reinforcement materials for nanocomposites include nanofibers, nanoplatelets, nanoclays etc. These reinforcements are functionalized with additives thereby resulting in a strong interfacial bond with the matrix. Generally, the three main mechanisms of interfacial load transfer are micromechanical interlocking, chemical bonding and the weak van der Waals force between the matrix and the reinforcement (Schadler et al., 1998). In order to form nanocomposite materials with excellent mechanical properties, strong chemical bonding between the reinforcement and the matrix is a necessary, but not sufficient condition.

In a previous experimental investigation (Xu et al., 2004a), Graphitic Carbon Nano-Fibers (GCNFs) were used as reinforcement in polymeric matrix nanocomposites.

Strong and stiff GCNFs (Young's modulus E > 600 GPa) have average diameters as small as 25 nm and demonstrate atomic structures such that edge carbon atom surface sites are present along the entire length of the carbon nanofiber. Chemical modification of these surface carbon sites and subsequent reaction with bifunctional linker molecules provides surface-derivatized GCNFs that can covalently bind to polymer resin molecules. By ensuring that a high number of surface sites on each GCNF form covalent bonds with polymer resin molecules, a carbon nanofiber/polymer interface of high covalent binding integrity can be achieved. This nanofiber/polymer covalent bonding is expected to delay interfacial debonding and should enhance the mechanical properties of the resulting nanocomposite material. So far, it has been difficult to quantify the improved interfacial bonding between the matrix and the nanofibers accurately (i.e., by direct measurement at the nano-scale). However, mechanical properties of the final macro-scale nanocomposite materials can be easily measured using various kinds of standard tests for engineering materials. To achieve maximum utilization of nanofiber properties, uniform dispersion and good wetting of the nanofibers within the matrix must be ensured (Zhong et al., 2004). All these local interfacial properties will affect the macro-level material behavior. For example, it was reported that there was as much as a 10% decrease in flexural strength in nanotube/epoxy composite beams due to weakly bonded interfaces (Lau et al., 2003). Also, significant reduction in composite stiffness was attributed to local nanofiber/nanotube waviness (Fisher et al., 2003; Srivastava et al., 2003). Xu et al., 2004a reports that bending, tensile and fracture property characterizations show that there was only very little increase in mechanical properties of nanocomposites although reactive linkers were used to improve the fiber/matrix interface.

It is suspected that the interfacial stress level in nanocomposites would be much higher than that of traditional composites because of high property mismatch between the nanoscale reinforcement and the matrix. Since high interfacial stress may lead to interfacial debonding and subsequent failure of nanocomposites, this may be the major reason contributing to the low failure strains in nanocomposites observed in many recent experiments (Xu et al., 2004a; Zhong et al., 2004). The small diameter of nanofibers or nanotubes affords increased interfacial contact area with the matrix, while its shortcoming is the high possibility of initial interfacial defects, which may lead to low failure strain of nanocomposites. Therefore, a theoretical analysis of interfacial stress transfer and stiffness and strength mismatch between the nano-scale reinforcement and the matrix will be much needed before we design and produce extensive varieties of nanocomposite materials.

As illustrated in Fig. 3.1, both the final failure strain (3.3%) and Young's modulus (2.9 GPa) of the pure epoxy are low. However, both the final failure strain (up to 10.0%) and Young's modulus (up to 1000 GPa) of the nanotubes or nanofibers are extremely high so the properties of the nano-scale reinforcement and the matrix are highly mismatched. A key question of nanocomposite design is that if these two types of materials were mixed (even if strong interfacial bonding was ensured); would the final composite properties (here we refer to the mechanical properties of discontinuous nanofiber/nanotube composites) demonstrate a reasonable increase over those of the

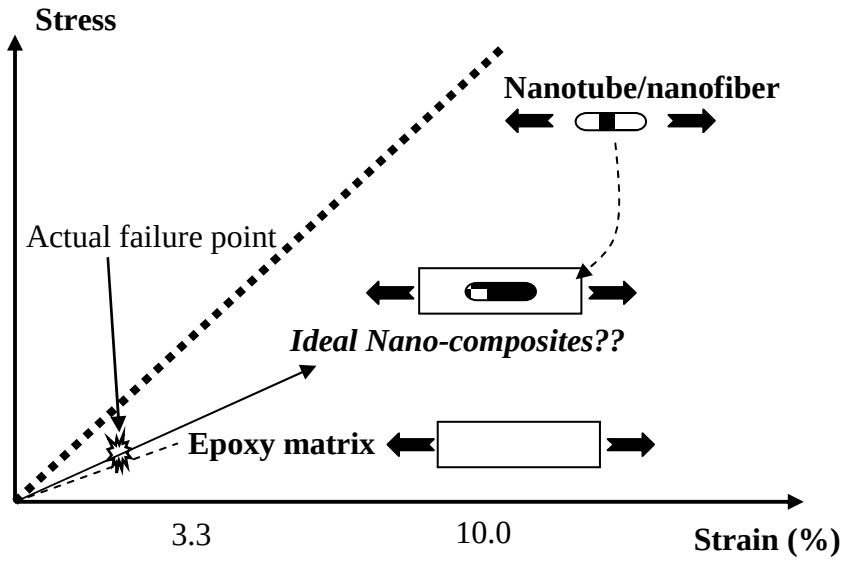

Fig. 3.1. Nano-composite design based on stress-strain curves

matrix? Generally, it has been found that the stiffness properties of nanocomposites are always higher than those of the pure matrix.

However, the strength of the nanocomposites may or may not exceed the strength of the pure matrix if discontinuous nanofibers/nanotubes (even if they were aligned) are used in nanocomposites. As seen in Fig. 3.1, the stress-strain curve of the nanocomposites is always steeper than that of the pure matrix if we only employ linear elasticity principles to simplify the explanation. Therefore, the final strength of the nanocomposites is mainly determined by the final failure strain of the nanocomposite. Unfortunately, the latter value was always lower than that of the pure matrix and significantly decreased with the increase of nanofiber/nanotube weight/volume percents as ascertained by numerous experimental studies.

3.2. FE Analysis and Stress Singularity Theory

The main purpose of this investigation is to seek the mechanical reasons for low failure strains of the nanocomposites. The major task is to examine the interfacial stress transfer which is critical due to high property mismatch of the nano-scale reinforcement and the matrix. Finite element analysis (FEA) was chosen as the primary tool for analysis instead of molecular dynamics simulations since the latter can only deal with physical phenomena at the level of a few nanometers at the current stage, while the size of a representative volume of a nanocomposite material ranges from 10 nanometers upwards to several hundreds of nanometers (Chen and Liu, 2004). Besides, the smallest dimension of our nanofiber lies in the range of 20-50 nano-meters and continuum mechanics assumptions, such as those used in finite element analysis, are still valid at such length-scales. Similar finite element analyses have been reported (Fisher et al., 2003; Chen and Liu, 2004) with a focus on stiffness analysis incorporating micro-

mechanics theory. It is noted that these finite element analyses simplified the complex interaction amongst the nano-scale reinforcement, matrix and the possible interphase. The interphase issue has received considerable attention in nanocomposite systems since nano-scale reinforcement affords a greater interphase volume compared to traditional composite materials. However, it is very difficult to determine the physical properties, such as thickness, of the interphase and they may certainly not be treated as material constants. From this viewpoint, the concept of interphase and its modeling is not employed in this investigation.

In this investigation, our objective is to investigate and reduce the singular interfacial stresses. Two separate cases were dealt with: (a) baseline nanocomposites subjected to tension and shear loading and (b) nanocomposite systems with modified nanofiber ends. Similar end modifications were effectively used to remove the interfacial stress singularity in macro-scale dissimilar material joints through integrated numerical and experimental investigation (Xu et al., 2004b). Since direct nano-scale experimental validation is very difficult to conduct at the current stage, numerical investigation is the focal point of research. Although nanofiber-reinforced composite is the main focus, the numerical analysis can be easily extended to nanotube-reinforced composite by varying the stiffness and dimensions of the nanoscale reinforcement.

Figure 3.2 (a) is a Transmission Electron Microscopy (TEM) picture showing short nanofibers well dispersed in an epoxy matrix. Usually, these nanofibers are curved and therefore the improvement in composite stiffness is not high (Fisher et al., 2003).

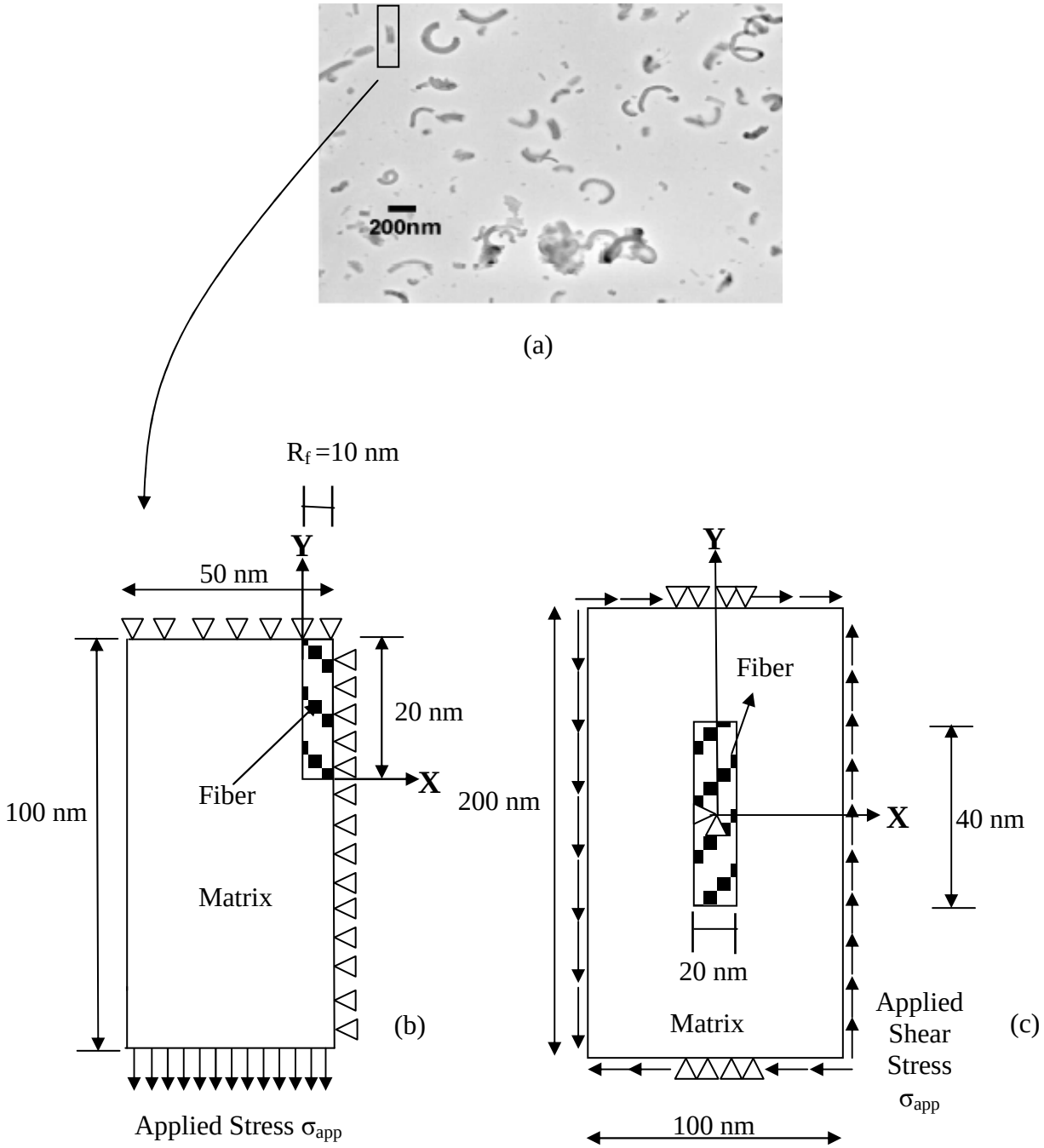

Fig. 3.2 (a) Transmission Electron Microscopy (TEM) image of nanofibers as dispersed in GCNF/epoxy nanocomposite and (b) Representative Volume Element (RVE) used for micromechanical analysis of nanofiber-epoxy nanocomposite under tension, σ_{app} = 0.01 nN/nm^2, V_f = 4%. A quarter of the original RVE is shown here with symmetric boundary conditions. (c) Same RVE under shear loading.

Based on the material analysis, a basic representative volume element for mechanics analysis (henceforth referred to as RVE) is shown with typical dimensions and boundary conditions in Fig. 3.2(b). Figure 3.2(c) shows the full RVE for shear loading case, with different boundary conditions. The volume fraction of the nanofiber/nanotube in the baseline RVE was 4% and this percentage was increased to 11% by retaining the dimensions of the nanofiber and decreasing the dimensions of the epoxy matrix.

A commercial FEA software ANSYS was used for numerical analysis. A transition mesh, using PLANE42 elements, was employed for the elements to fan out from a dense mesh in and around the nanofiber-epoxy matrix interface to a relatively coarser mesh utilized for the rest of the RVE. The material properties used in the baseline RVE were: epoxy matrix: E_m = 2.6 GPa, ν_m = 0.3; nanofibers E_f = 600 GPa, ν_f = 0.3. Similar to other finite element analyses, nanofibers were treated as transversely isotropic materials (Fisher et al., 2003; Chen and Liu, 2004). The elastic modulus of the nanofiber was varied such that four typical reinforcement cases were considered: E_f = 50 GPa (glass fibers), 200 GPa (carbon fibers), 600 GPa (graphite nanofibers) and 1000 GPa (carbon nanotubes). Remote tensile stress of 10 MPa (= 0.01 nN/nm^2) was applied along the shorter edge of the epoxy matrix and a linear elastic analysis was run to determine the dependence of interfacial stresses on elastic properties and volume fractions. The analyses were varied in terms of (a) applied stress of 10 MPa or (b) applied displacement of 0.1 nm to the RVE.

If two dissimilar materials are joined, interfacial stress components may be singular — hence a special approach will be employed to characterize their distributions (Munz and Yang, 1993):

$$\sigma_{ij}(r,\theta) = \frac{K}{(r/L)^{\lambda}} f_{ij}(\theta) + \sigma_{ij0}(\theta) \tag{3.1}$$

Here r and θ are polar co-ordinates, L is a characteristic length, K is the stress intensity factor and the constant stress term σ_{ij0} has been defined such that for mechanical loading perpendicular to the interface, $\sigma_0 = 0$. Also, $f_\theta(\theta)$ was defined in such a way that $f_\theta(\theta = 0) = 1$. Taking the logarithm of both sides of Equation (3.1), the stress intensity factor K can be obtained from the numerical interfacial stress distribution of $\lg(\sigma_\theta^{FE}(r,\theta) - \sigma_{\theta 0}(\theta))|_{\theta=0}$ versus lg(r/L). In this investigation, the radius of the nanofiber r_f is taken as the characteristic length L. The calculation of the stress singularity order λ was based on the determinant $f(\theta_1, \theta_2, \alpha, \beta, p)$ introduced by Bogy, 1971. For any particular material combination, the Dundurs' parameters α and β were calculated, which represent stiffness mismatch of two joint materials (Hutchinson and Suo, 1992). Besides, the joining angles for two kinds of materials were known: 90° for the nanofiber and 270° for the epoxy matrix. As such, the only unknown parameter p (=1-λ) could be determined from the equation cited earlier in Chapter 2 (equation 2.3).

3.3. Results and Discussion

3.3.1. Effect of varying Young's modulus

Different loading cases were applied to the RVE, and very different interfacial stress distributions along the short interface between the matrix and the nanofiber with straight ends were obtained, as illustrated in Figs. 3.3(a) and 3.3(b). While the interfacial normal stress in the tensile loading case remains positive in nature along the length of the short interface, Fig. 3.3(b) shows that the interfacial normal stress along the short interface changes from a positive value (tensile) to a negative value (compressive). This means that under shear loading, one end of the fiber is "pulled down" while the other end is "pushed out". Therefore, we may expect that the same nanofiber-reinforced composite would yield higher ultimate strengths or strains under shear loading as compared to tensile loading. It was also noticed that a higher Young's modulus of the reinforcement led to higher interfacial stresses for both loading cases and would surely induce a macroscale crack to cause final composite failure.

3.3.2. Effect of Young's moduli mismatch on stress singularity order

Figure 3.4 depicts the variation of the stress singularity order with Young's moduli mismatch between the matrix and the fiber. Since the singular stress values prevent accurate comparisons for different material combinations, the stress singularity orders were computed to compare different E_f/E_m cases. The starting point of the stress singularity order curve corresponds to the case where there is no property mismatch or zero stress singularity order. This curve shows a smooth transition and reaches a plateau gradually as E_f/E_m assumes a larger value.

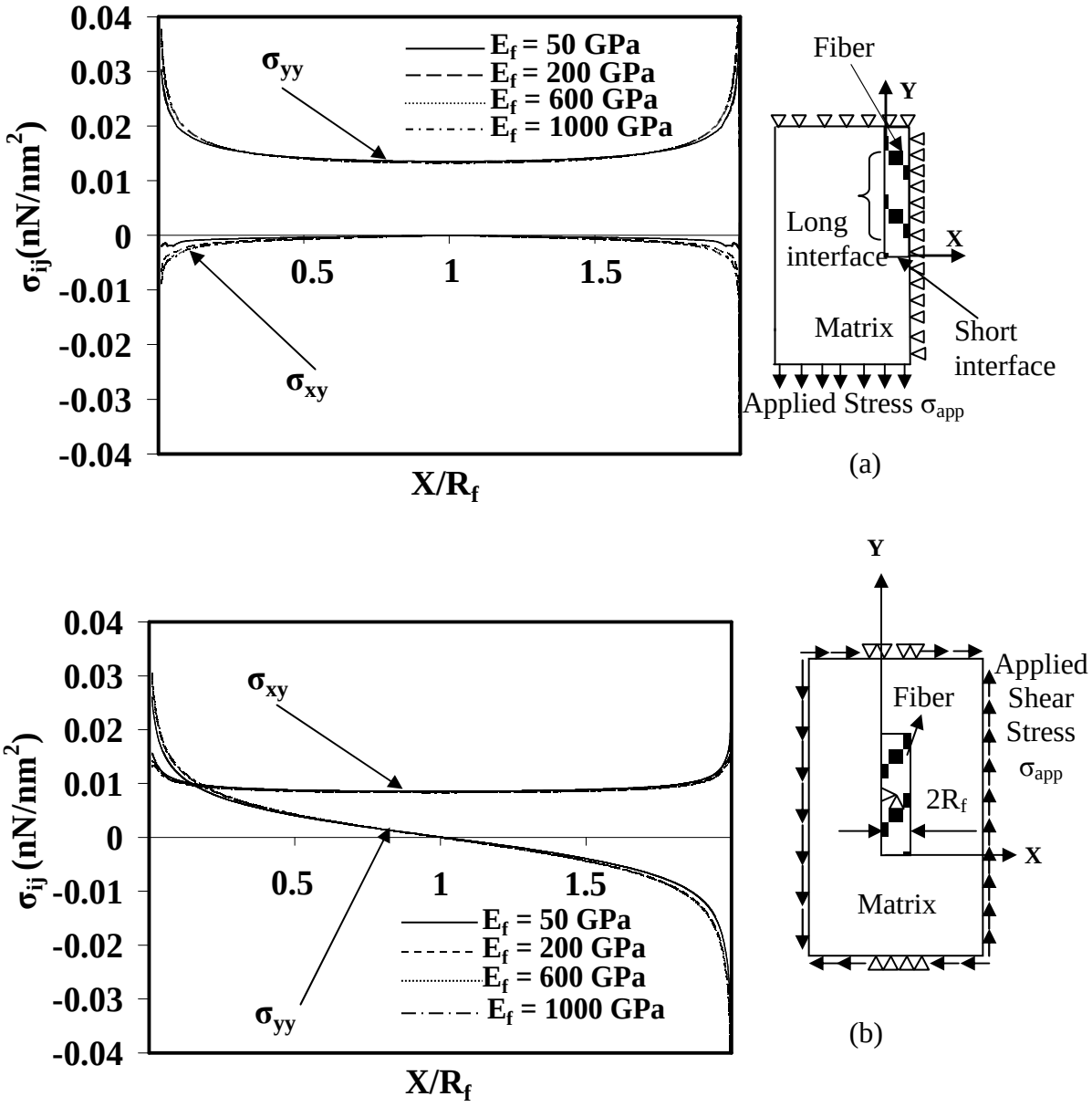

Fig. 3.3. Effect of applied loading types on the interfacial stress distributions (a) along the short interface for tension loading (b) along the short interface for shear loading (full specimen analyzed). V_f = 4%. Applied stress = 10 MPa.

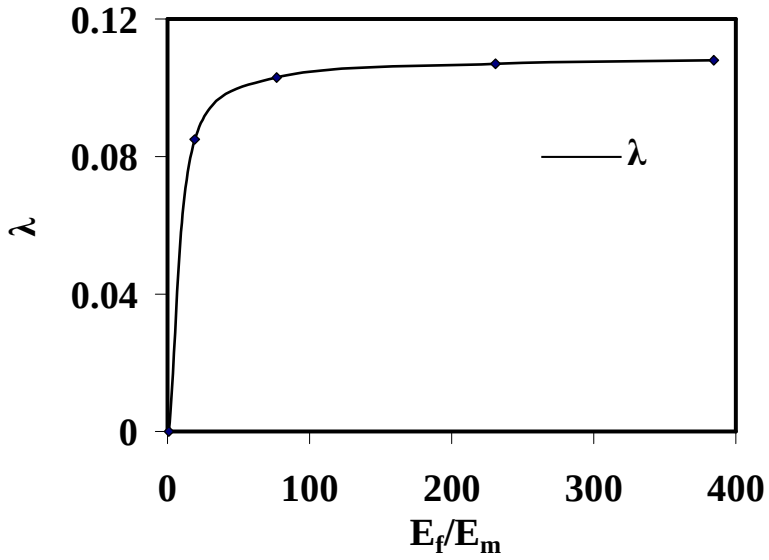

Fig. 3.4. Effect of Young's moduli mismatch on stress singularity order

3.3.3. Effect of volume fraction for applied stress boundary condition

Figure 3.5 depicts the effect of volume fraction on interfacial shear and normal stresses along the short and long interfaces, in response to an applied stress of 10 MPa. While an increase in volume fraction showed little effect on the stress distributions along the short interface, the interfacial shear stress along the long interface seems to be least for the baseline volume fraction V_f = 4% and increases slightly with increasing volume fraction. This would mean that a high volume/weight fraction of nanofibers has little influence on the local interfacial stress state, or on the final failure strain of the nanocomposite material. However, this was contradicted in the applied tensile strain case.

3.3.4. Effect of volume fraction for applied strain boundary condition

Figure 3.6 depicts the effect of nanofiber volume fraction on the interfacial shear and normal stresses along the short and long interfaces, in response to applied displacement of 0.1 nm (which corresponds to an applied tensile strain case). An increase in volume weight fractions of nano-scale reinforcements led to lower ultimate failure strains of nanocomposite materials. One might suspect that these results are caused by the singular interfacial stresses at the rectangular nanofiber ends.

3.3.5. Effect of geometry of nanofiber end

The possible singular interfacial stresses at the rectangular nanofiber ends are not the only reasons responsible for low failure strengths or strains - another important issue is interfacial stress transfer. Figure 3.7 shows the effect of geometry of the nanofiber end on the interfacial stress distributions. Two cases were considered: (a) the baseline case with straight edge forming a 90° at the interface corner and (b) round interface corner with a radius of 1 nm.

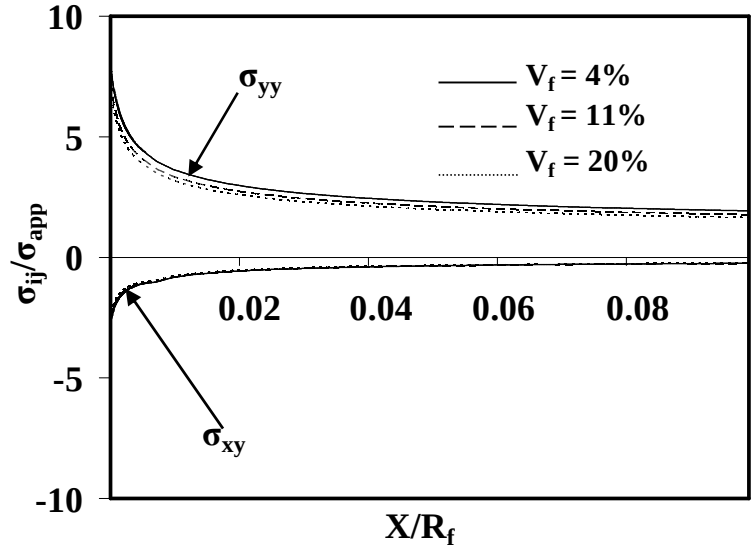

(a)

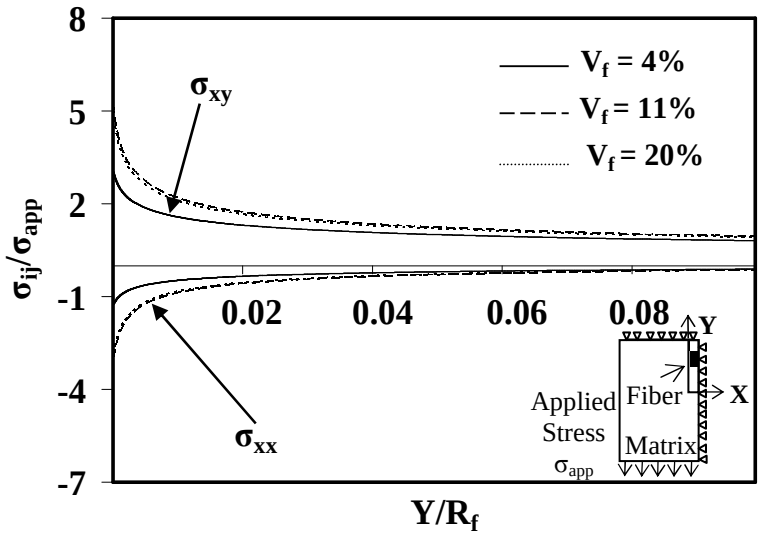

(b)

Fig. 3.5. Effect of nano-fiber volume/weight percents on interfacial stress (a) short interface under applied stress of 10 MPa (b) long interface under same applied stress.

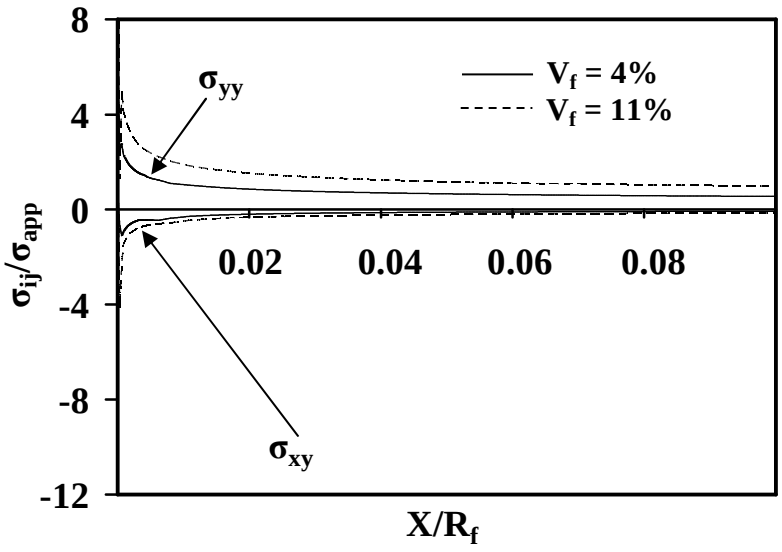

(a)

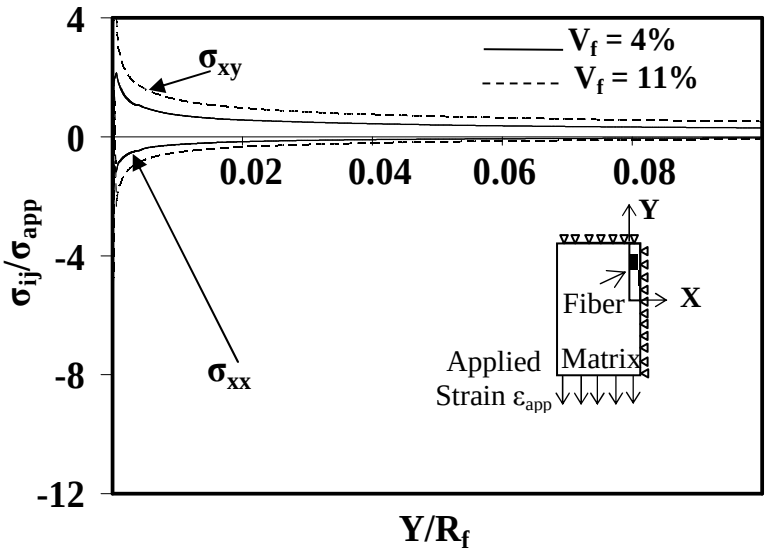

(b)

Fig. 3.6. Effects of the nanofiber volume percents on the interfacial stress distributions (a) along the short interface under applied displacement 0.1 nm (b) along the long interface under the same applied displacement.

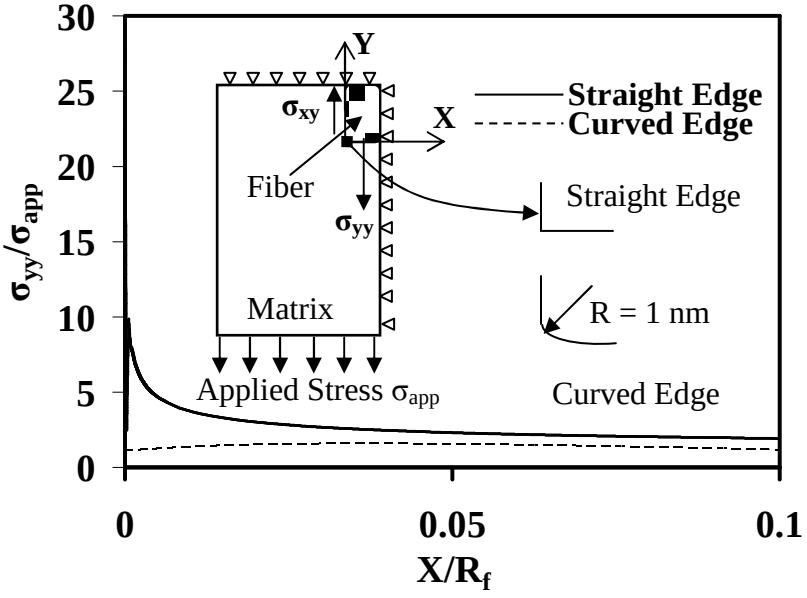

(a)

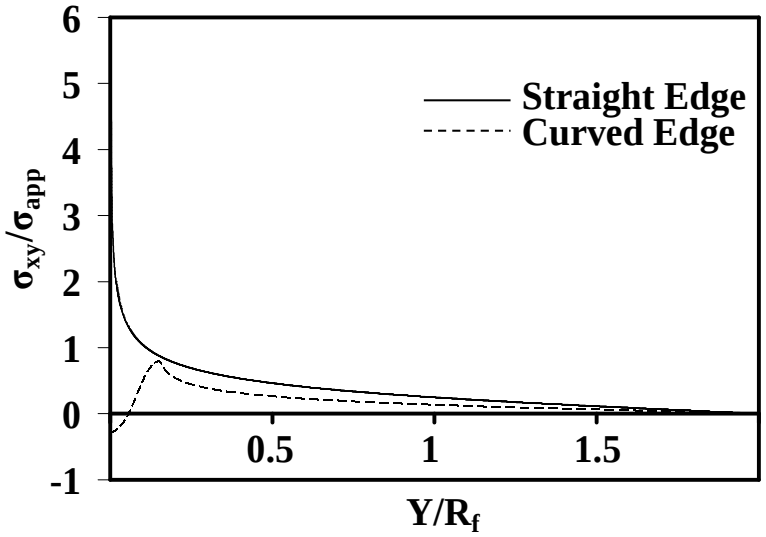

(b)

Fig. 3.7. Effect of the nanofiber end on the interfacial stress distribution (a) normal stress variation along short interface and (b) shear stress variation along the long interface for V_f = 4%, E_f=600 GPa, applied stress = 10 MPa.

As expected, the normal stress over the short interface showed a strong singularity in case (a) but not so in case (b). Shear stress variation along the long interface depicted in Fig. 3.7(b) also shows a significant reduction around the interfacial corners. Hence, nanofibers with slightly rounded edges are a better alternative to common nanofibers with straight edges. Similar conclusions for traditional fiber-reinforced composites were drawn by other researchers (Sun and Wu, 1983; Liou, 1997). However, the normal stress distribution of the nanofiber did not change significantly by shaping the nanofibers. Besides, from the composite processing viewpoint, rounded ends for each nanofiber would prove to be very time-consuming and costly.

3.3.6. Effect of volume fraction and Young's modulus on normal stress

The effects of both volume fraction and Young's modulus on the normal stress distribution along the mid-plane of the nanofiber, with straight or curved edges, have also been examined in Figs. 3.8(a) and (b). The normalized stress is seen to rise towards the center of the fiber as a result of interfacial shear transfer, or shear-lag effect (Gibson, 1994; Baxter, 1998). However, the maximum normal stress in the nanofiber is only around 1.6 times that in the matrix, far below the strength ratio of the nanofiber/nanotubes over the polymeric matrix (at least 100). Although some research results showed that modified ends/edges of the short fibers could effectively remove the stress concentration/ singularity (Sun and Wu, 1983; Liou, 1997; Gibson, 1994), the normal stress distribution of the short fiber is not altered significantly.

Therefore, such composite design will not make full use of the high strength of nanofibers/nanotubes. Discontinuous nanotubes/nanofibers with high strength and stiffness, when added as reinforcement to matrices, are undermined by the stress

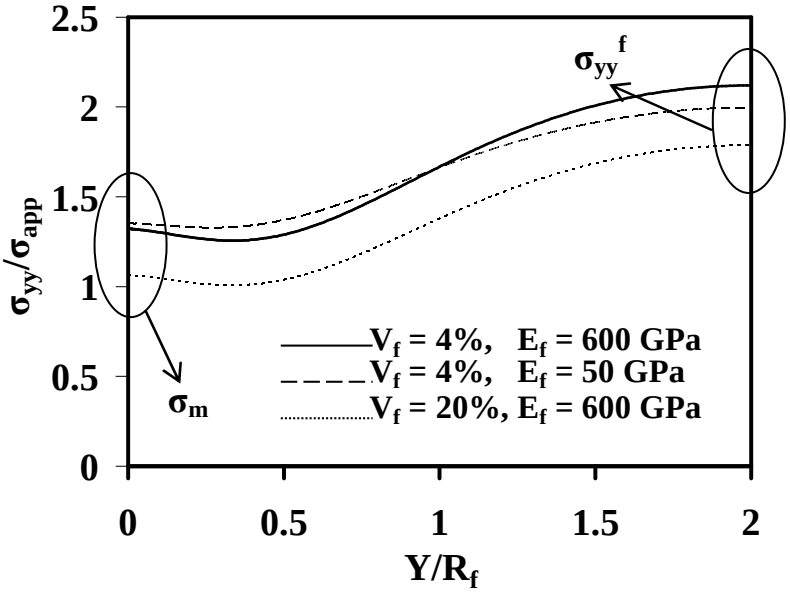

(a)

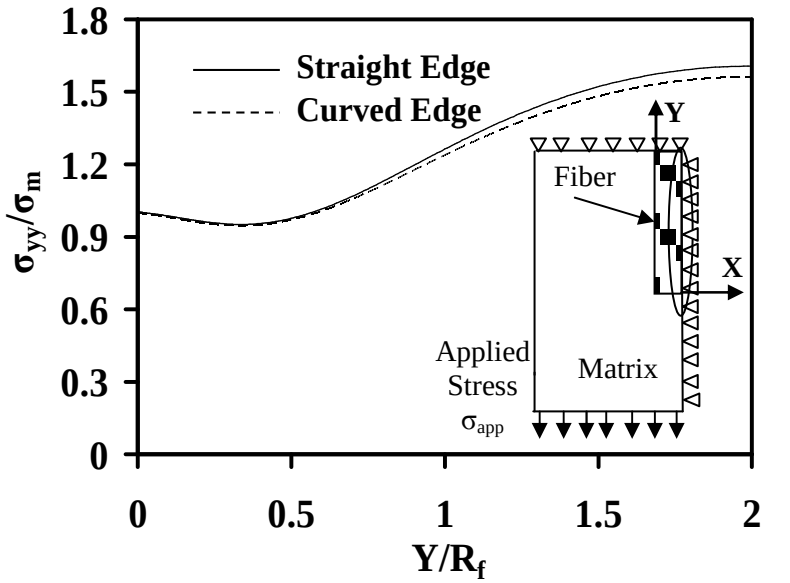

(b)

Fig. 3.8. Nano-fiber stress distribution under tensile load (mid-fibre stress) (a) variation with Young's modulus and volume fraction and (b) for straight edged and round edged nanofiber. Radius of round-edged nanofiber = 1 nm. σ_m = normal stress inside the matrix, σ_{yy}^{f} = normal stress inside the fiber. V_f = 4%, E_f = 600 GPa, applied stress = 10 MPa.

singularity at the fiber-matrix interface, and also by the inefficient interfacial shear stress transfer even if all nanofiber ends were rounded through special processing. This provides us with an important principle for nanocomposite design. It should be noted that the finite end stress singularity is a theoretically elastic phenomenon and will never occur in reality. A significant reduction in singularity has been noticed when more accurate models are used to depict the polymeric matrix (e.g. elastoplastic, viscoelastic model) in traditional composites with graphite fibers. In addition, for nanotube-reinforced composites, since the nanotube has a lattice-type structure at the nanometer level, the actual singularities that occur at the interface should be much lower than those predicted using the continuum mechanics approach.

Therefore, these two arguments lead to the conclusion that the singularities predicted in this investigation are overestimated. However, the interfacial shear stress concentration (due to the theoretical stress singularity) definitely becomes more severe if the stiffness mismatch of the reinforcement and the matrix increases, which in turn will lead to interfacial debonding.

3.4. Conclusions

Discontinuous nanotubes/ nanofibers with high strength and stiffness, when added as reinforcement to matrices, are undermined by the stress singularity at the fiber-matrix interface, and also by inefficient interfacial shear stress transfer. However, continuous forms of nanofibers or nanotubes without finite ends, on the other hand, preclude the presence of extra matrix material at the ends of fibers and hence eliminate stress concentration/ singularity. Thus, for future nanocomposite material designed with

an objective of strength or fracture toughness increase (Xu et al., 2004a; Roy et al. 2003), discontinuous nanofibers or nanotubes (in spite of being aligned) are not recommended.

CHAPTER IV

AN INNOVATIVE TECHNIQUE FOR INTERFACIAL FRACTURE TOUGHNESS MEASUREMENT

4.1. Introduction

4.1.1 Objectives

A material configuration of singular importance in micro-electronics is a thin film of one material deposited on a substrate of another material. In such cases, residual stresses and material discontinuities arise naturally from the deposition or growth processes used to produce such films and further stresses might be imposed due to mismatch in coefficients of thermal expansion of the film and the underlying substrate, chemical reactions or other physical effects. As such, the weakest link of such configurations occurs at the interface between the thin film and substrate (Chaudhury et al., 1999; Pint et al., 1998; Pindera et al., 2000; Evans et al., 1999). In order to manufacture multi-layered electronic devices and composites with long-term reliability, fracture behavior of the material interfaces must be well characterized. Since a state-of-the-art test procedure for evaluating interface fracture toughness that is fully conformed to fracture mechanics theory is still lacking, there is a great deal of uncertainty involved in the test results for thin coatings. The spiral notch torsion test (SNTT) was developed, by researchers in Oak Ridge National Laboratory, to address the problems associated with this deficiency in general (Wang et al., 2000; Wang, 2003). The role of this work is to model the SNTT and more specifically to determine the interfacial fracture toughness applicable to thin coatings. The objective of determining an accurate method of

characterization of interfacial fracture toughness is to enable the development of new coating materials with predictable performance assessment.

4.1.2. Advantages of SNTT over existing test methods

The current experimental techniques such as double-cantilever beam tests, four-point bending tests, indentation techniques etc are widely used in bi-material interface research (Turner and Evans, 1996; Charalambides et al., 1989; Suo and Hutchinson, 1989). In the first two methods, a large deal of uncertainty is involved in toughness evaluation since the interfacial crack does not generally propagate along the interface. In indentation technique, on the other hand, the test result is dependent on indentation load, penetration depth, specimen size and geometry. Due to these reasons, it becomes necessary to introduce a new method for interfacial toughness evaluation that reduces the uncertainty in quantification. To this end, a new method to evaluate fracture toughness of thin films on substrates has been developed by combining experimentation and numerical analysis.

The compact-tension specimens that are traditionally used for fracture toughness measurement have an inherent problem which is lack of means to uniformly distribute applied load throughout the entire specimen thickness. In contrast, the torque load acting on every cross-section along the rod-shaped SNTT specimen is the same and directly measurable. A plane-strain condition is achieved on every plane normal to the spiral groove.

For valid fracture toughness testing, conventional ASTM standards require fatigue precrack procedure to develop sharp crack front, which is a difficult task for interfacial fracture testing and the fatigue precrack itself causes large uncertainty in the results. For

SNTT approach however, no fatigue precrack is needed for brittle material such as ceramic or oxide layer and for ductile interface, the fatigue crack growth is expected not to change its course along the interface.

4.2. SNTT Approach for Toughness Evaluation

It should be mentioned at the onset that the SNTT methodology has been verified for homogeneous materials and for relatively large samples. Consequently, a feasibility study was conducted to study the applicability of this concept to determine the interfacial toughness of thin film-substrate systems – specifically that of thin aluminum oxide scales formed on a high-temperature commercial alloy, MA956 (Incoloy).

The SNTT methodology is based on applying pure torsion to a cylindrical specimen machined with a helical groove at a 45° pitch angle. The pure torsion creates a uniform, equi-biaxial tension/compression stress field on each concentric cylinder and the groove becomes an effective Mode I crack mouth opening, as shown in Fig. 4.1(a). The conceptual design used for testing the thin film is illustrated in Fig. 4.1(b). A circular rod of alloy MA956 (composition Fe20-Cr4.5-Al0.5-Y_2O_3), machined with a shallow groove was used as the baseline. At high temperatures and in presence of oxygen, this alloy forms a uniformly thick, adherent surface film of alumina. While this thin layer of alumina protects the substrate from damage (required in devices operating at high temperatures), it also prevents infra-red penetration – this makes it difficult to ascertain the exact position of crack initiation. A parameter study of notch geometry e.g. V- or U-

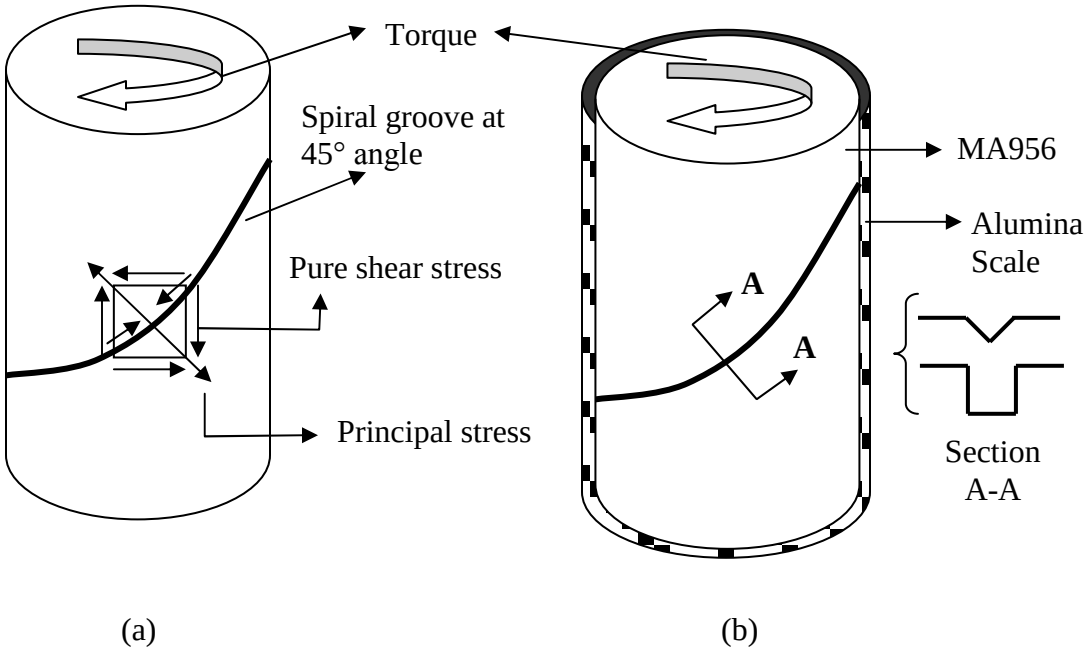

Fig 4.1. (a) Original SNTT specimen configuration for single-phase material
(b) Modified SNTT configuration for thin film specimen

notches will be conducted to determine the most suitable configuration for thin film testing. The SNTT method used for numerical determination of fracture toughness comprises of the following steps:-

1) Model a slice of the middle-portion of the cylindrical specimen overlaid by thin film and having a spiral groove at 45° pitch angle
2) Calculate K_{Ic} using following steps:
    a) Establishing 3D finite element meshes with wedge singular elements around crack front.
    b) Simulating spiral crack front and crack propagation orientation along the right conoids.
    c) Determining stress intensity factors K_I, K_{II}, K_{III} and J-Integral value.
    d) Determining fracture toughness K_{Ic} based on minimum energy criterion.

4.3. Fracture Mechanism of SNTT Thin Film Specimen

Experiments conducted on an alumina-MA956 thinfilm-substrate specimen have helped in postulating certain assumptions in the finite element model construction. No fatigue precrack was modeled since the oxide layer is brittle and a U-groove is sufficient for the crack to propagate under torsion loading. The details of the notch root geometry and the failure initiation site in a thin film sample are shown in Fig. 4.2 (a). The shaded area of alumina scale in Fig. 4.2 (a) indicates the region of thin film capable of transmitting resultant force of the principal stress induced by torsion loading. It can be surmised that, based on the relatively high hardness of the thin film compared to that of the substrate and the high compressive residual stress in the thin film, a crack is more

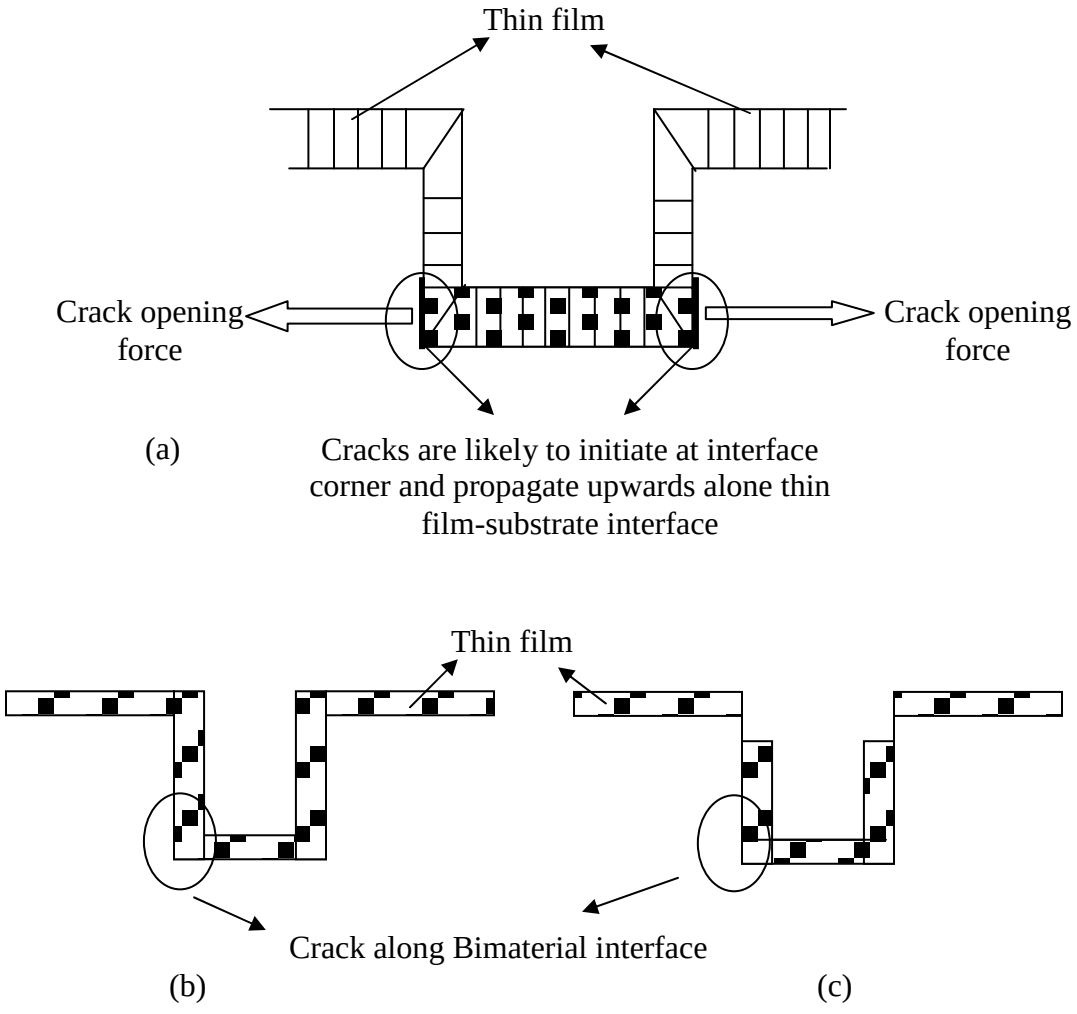

Fig. 4.2. Schematic diagram of notch root geometry and (a) possible associated crack initiation sites (b) actual layout near U notch (c) modified layout near U notch incorporated in finite element model.

likely to initiate from the corner of the notch root and propagate upwards along the interface. Moreover, it was ascertained from SEM examination of tested SNTT thin film samples that the corners of the thin film, adjacent to the substrate, were spalling under compressive stresses induced by thermal cooling. Preliminary calculations also showed that the contribution of the thin film to the total torque was only 2% and hence, the finite element model near the notch was modeled as shown in Fig. 4.2 (c), as opposed to the actual notch layout as seen in Fig. 4.2 (b).

4.4. Analytical Evaluation

4.4.1. Development of finite element model and analysis

A three-dimensional finite element study of the spiral notch torsion specimen was developed, for evaluating interfacial fracture toughness of a bimaterial system. This model, as mentioned before, has a thin film of alumina on the outside and a substrate core composed of MA956. PATRAN and ABAQUS were used as preprocessing and post-processing tools respectively – the former tool being used to generate three-dimensional mesh and the latter tool to analyze. Prismatic quadratic isoparametric singular elements surrounding the crack tip were modified to incorporate linear elastic and non-linear elastic-plastic capabilities. In the former, the nodes at the crack tip were constrained to have the same displacement. However, in case of perfect plasticity, the nodes at the crack tip were modeled such that they would be free to displace independently from each other.

4.4.2. Three dimensional configuration of SNTT finite element model

The mid-section of the SNTT specimen was used, as depicted in Figs. 4.3 (a) and (b) which includes a cylinder of radius 0.15 in, height of 0.1 in with a 45° spiral U-groove of depth 0.0166 in. The thin film thickness was set at 15 microns and the initial interfacial crack length was set at 5 microns. A void element was incorporated into the model just below the flaw in order to simulate the potential flaw site and it was anticipated that the initial crack growth would propagate upwards along the interface, instead of downwards through the substrate. This is obvious because less energy would be required for crack formation if the crack traveled along the interface – a region that is already susceptible to failure. Mesh configuration details near the bottom of the U-groove are shown in Fig. 4.3(c).

A major issue in constructing the FE thin film model was to incorporate large mesh size of the substrate and small mesh dimensions of the thin film in one model. The wide range of FE mesh size requires several layers of transition zones to mitigate the gradient of adjacent dissimilar mesh sizes. The details of three-dimensional FE models for mid-section of an SNTT thin film specimen and a focused view of the same are shown in Figs. 4.4 (a) and (b).

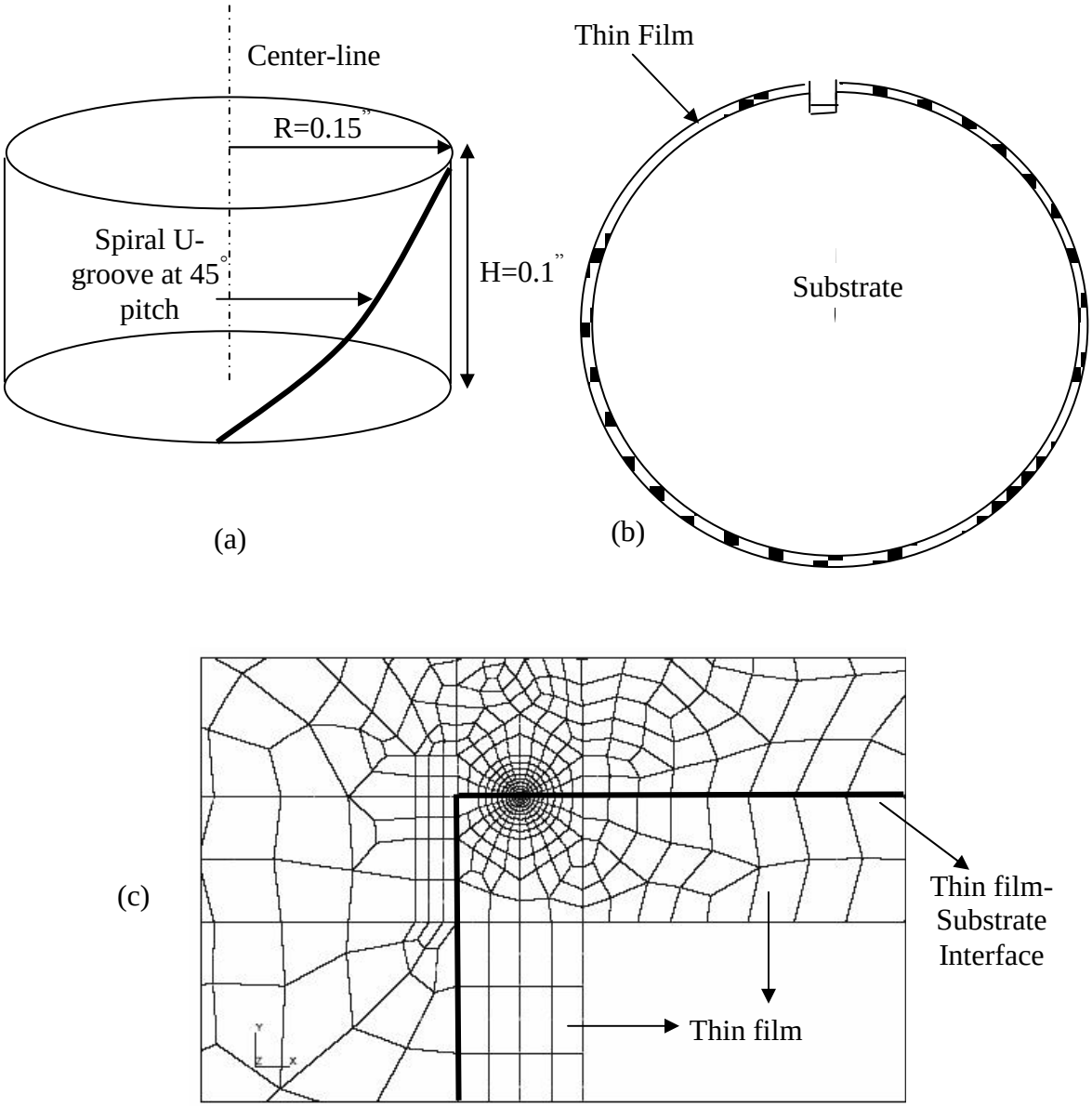

Fig. 4.3. (a)Elevation and (b) top view of SNTT finite element model
(c) detailed configuration of mesh near bottom corner of U-groove

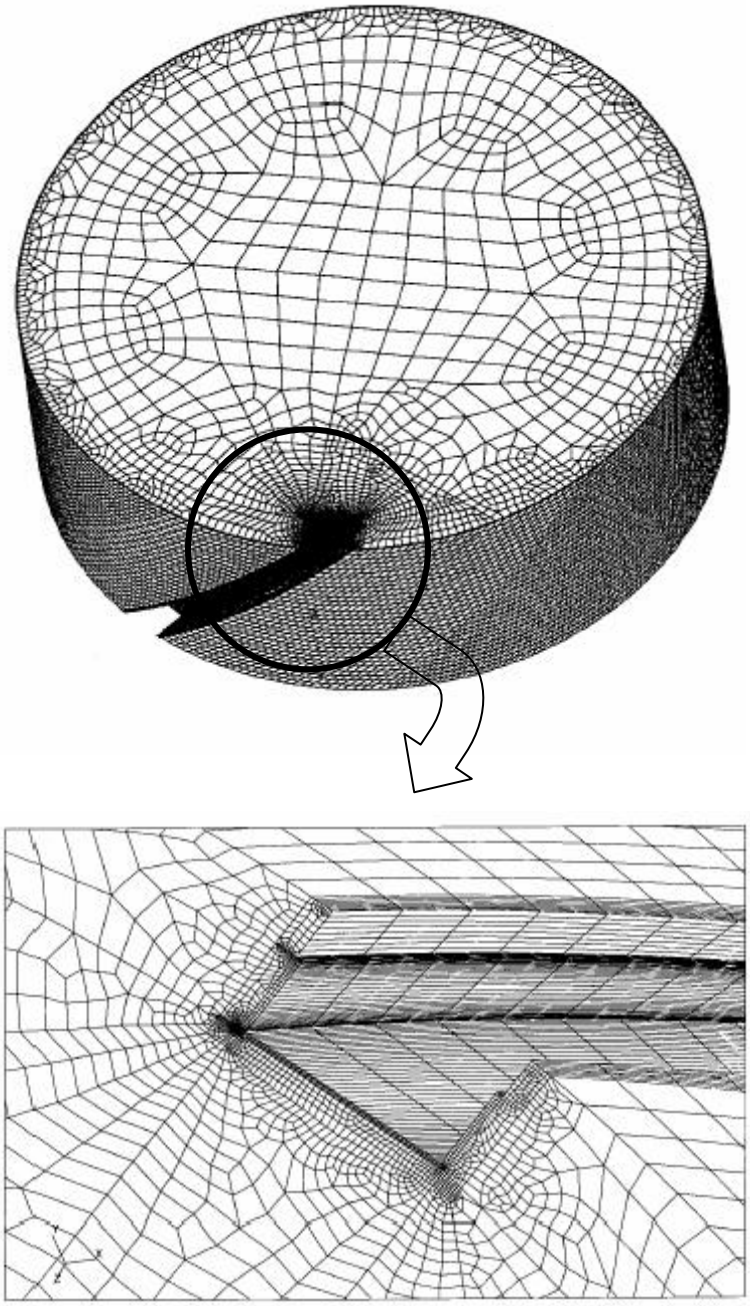

Fig. 4.4. (a) Finite element model for middle section of SNTT thin film sample (b) Details of SNTT thin film FEM near U-groove site

Boundary conditions and load cases were determined from experimental results which yielded a fracture torque of 4.77 N-m. This fracture torque was applied to the top layer of the finite element model in the form of displacement while the bottom layer of the model was kept fixed in the X-axis and Y-axis directions i.e. along two perpendicular radii of the cylinder surface. Displacements were allowed in the Z-axis direction or along the cylinder axis, to replicate experimental boundary conditions. An initial end rotation of 0.002334 radians was assigned to the top of the model; this was estimated from the fracture torque applied to a smooth bar with the same dimensions as the SNTT finite element model. The alumina film residual stress in terms of hydrostatic pressure was 2.5 GPa along the U-groove site and 3.7 GPa elsewhere on the film. The initial end rotation and the residual stress fields were used as input for the load cases.

The material properties of MA956 and alumina scale used in the FE analysis were: Alumina: E = 355 GPa, ν = 0.26, MA956: E=269 GPa, ν = 0.31.

4.4.3. Fracture toughness and J-Integral evaluation along the bi-material interface

The stress intensity factors K_I, K_{II}, K_{III} characterize the influence of load or deformation on the magnitude of the crack-tip stress and strain fields and measure the propensity for crack propagation or crack driving forces. For plane strain mode I, the energy release rate G_I can be written as (Irwin, 1957):

$$G_I = \frac{K_I^{\,2}(1-\nu^2)}{E} \tag{4.1}$$

Where E = Young's modulus, ν = Poisson's ratio. Similarly, for modes II and III, the energy release rates may be written as:

$$G_{II} = \frac{K_{II}^{\,2}(1-\nu^2)}{E} \qquad G_{III} = \frac{K_{III}^{\,2}(1-\nu^2)}{E} \tag{4.2}$$

For mixed mode fracture, the total energy release rate may be written as:

$$G = G_I + G_{II} + G_{III} \tag{4.3}$$

For a linear elastic material, G can be related to the J-integral as:

$$J = G \tag{4.4}$$

For an interfacial crack between two dissimilar isotropic materials with Young's moduli E_1 and E_2, Poisson's ratios ν_1 and ν_2 and shear moduli $\mu_1 = \frac{E_1}{2(1+\nu_1)}$ and $\mu_2 = \frac{E_2}{2(1+\nu_2)}$

J can be written as:

$$J = \frac{(1-\beta^2)}{E^*}(K_I^2 + K_{II}^2) + \frac{1}{2\mu^*}K_{III}^2 \tag{4.5}$$

Where, $\frac{1}{E^*} = \frac{1}{2}(\frac{1}{E_1} + \frac{1}{E_2})$, $\frac{1}{\mu^*} = \frac{1}{2}(\frac{1}{\mu_1} + \frac{1}{\mu_2})$ and $\beta = \frac{\mu_1(\kappa_2 - 1) - \mu_{21}(\kappa_{12} - 1)}{\mu_1(\kappa_2 + 1) + \mu_{21}(\kappa_{12} + 1)}$

and $\kappa = 3 - 4\nu$ for plane strain, axisymmetry and three dimensions; and $\kappa = \frac{(3-\nu)}{(1+\nu)}$ for plane stress (Shih and Asaro, 1988; Shih et al., 1986; Suo, 1990). Here, K_I and K_{II} are not the pure Mode I and Mode II stress intensity factors for an interfacial crack. They are simply the real and imaginary parts of a complex stress intensity factor, whose physical meaning can be understood from the interface traction expressions:

$$(\sigma_{22} + i\sigma_{12})_{\theta=0} = \frac{(K_I + iK_{II})r^{i\varepsilon}}{\sqrt{2\pi r}}, (\sigma_{23})_{\theta=0} = \frac{K_{III}}{\sqrt{2\pi r}} \tag{4.6}$$

where r and θ are polar co-ordinates centered at the crack tip. The bi-material constant ε is defined as:

$$\varepsilon = \frac{1}{2\pi}\ln(\frac{1-\beta}{1+\beta}) \tag{4.7}$$

The J-integral was calculated using the *CONTOUR INTEGRAL command of ABAQUS, which is based on the domain integral method. Since the co-ordinates of the

FE model were chosen to coincide with the principal stress orientation and since 99% of the J value is contributed by J_I (Wang et al., 2002), the contribution of K_{III} to the overall energy release rate can be considered to be negligible and equation (4.5) may be rewritten as (Shih, 1991):

$$J = \frac{(1-\beta^2)}{E^*}(K_I^2 + K_{II}^2) = \frac{(1-\beta^2)}{E^*}\left|K^*\right|^2 \tag{4.8}$$

Here, $K^* = K_I + iK_{II}$ and $\left|K^*\right| = \sqrt{\frac{E^* J}{(1-\beta^2)}}$.

For oscillatory fields, the phase angle of the mode mixity is specified by (Shih, 1991):

$$\tan\psi = (\frac{\sigma_{yx}}{\sigma_{yy}})_{r=L^*} \tag{4.9}$$

The length parameter L^*, although arbitrary, is constant for a chosen material pair. For a MA956-alumina scale thin film interface configuration, the bi-material constant ε is estimated to be 0.0057 – a relatively small quantity. Thus, $K^* r^{i\varepsilon}$ can be replaced by K^* and the associated mode mixity angle written as:

$$\tan\psi = (\frac{\sigma_{yx}}{\sigma_{yy}})_{r\to 0} or \tan\psi = \frac{K_{II}}{K_I} \tag{4.10}$$

Along the crack propagation orientation, the SNTT configuration has a relatively small K_{II}/K_I ratio and the associated phase angle can be set to zero. For the purpose of establishing a connection between the Mode I fracture toughness in homogeneous media, at the fracture load, the estimated equivalent Mode I interface fracture toughness can be written as:

$$K_{IC}^* = \sqrt{\frac{E^* J_c}{(1-\beta^2)}} \tag{4.11}$$

Where J_c = estimated J integral value at fracture.

4.5. Finite Element Analysis Results and Fracture Toughness Evaluation

4.5.1. Fracture toughness evaluation for oxide MA956 SNTT specimens

Throughout most gage lengths, uniform stress and strain fields exist in the test sample under pure torsion loading. However, only a portion of the gage length of the test sample was used in the FE model. Thus, with simulated boundary conditions, the stress and strain distributions under pure torsion are not entirely uniform throughout the model sample. However, the middle portion can be assumed to be reasonably uniform. Since a zero axial load is maintained during torsion, the specimen is permitted to deform freely along the axis. For all practical purposes, this condition can be simulated for the middle layer elements of the finite element model and was therefore used as a numerical boundary condition.

The torque applied to the specimen from the prescribed end displacement was calculated according to the following equation:

$$\text{Torque}_{END} = \Sigma\,(R_y * x - R_x * y)_{\text{node i}} \tag{4.12}$$

Where, R_x and R_y are the reaction forces at the fixed end of the FEM in the X-axis and Y-axis directions, respectively, derived from the linear elastic fracture mechanics for the fracture loading condition; here, x and y are the x- and y-components of the distance between the node i and the center of the circular bar, respectively.

The $3.593\times10{-}4$ radian end rotation at the fracture load of 4.63 N-m (41 in.-lb) was determined by iterative processes using eq. (4.12). Based on linear elastic fracture mechanics, at the fracture load, the J value in the crack propagation orientation at the

mid-layer of the FEM was estimated at 3.7 N-m/m² (0.021 lb-in./in²) for the sharp crack front. The E^* and β of eq. (4.5) are estimated as 311 GPa (4.52×104 ksi) and −0.008, respectively. Substituting E^* and β value into eq. (4.11), we obtained the estimated equivalent Mode I interface fracture toughness as 1.1 MPa$\sqrt{m}$ (0.97 ksi. *in)* for a sharp crack front model. The estimated equivalent Mode I interface fracture toughness of a sharp crack front is 1.1 MPa$\sqrt{m}$, which is lower than that of the alumina scale.

The experimental evaluation and the analytical evaluation seem to support that the interface is the weakest link for a non-precracked SNTT thin film sample. The extremely high compressive residual stress embedded within the thin film will retard the crack initiation but keeps the thin film intact. Therefore, for the SNTT thin film sample, the spallation failure of alumina scale involves a two-step process. First; the crack initiates at the interface and then propagates along the interface - this releases the associated tensile residual stress in the substrate locally just underneath the thin film. Second; torque-induced external tensile stress, applied to the substrate and the alumina at the interface, has a tendency to cause the delaminated alumina scale to move away from the substrate. The section of delaminated alumina scale resembles a non-lateral-support column with a compression loading. It eventually buckles at a threshold crack length along the interface and results in the spallation of alumina scale.

The residual stress of a thin film material is largely a direct result of the coefficient of thermal expansion mismatch between the scale and the substrate during the cooling. Thus, from a material history point of view, the residual stress represents a pre-loading boundary condition but also a thin film material property. Therefore, the residual stress plays an important role in the interface fracture toughness evaluation. Furthermore,

it is expected that slightly different compressive residual stresses of alumina scale will be experienced (or measured) at the side groove if different shapes of side grooves, such as U- or V-shapes are used. However, the associated stress-strain states of the substrate at the side groove, both before or during the torque loading, will also be different because of different geometry constraints if different side grooves are used. The combined effect of the compressive residual stress and the loading stress states of the substrate may offset each other for different groove geometries and result in less dependence on side groove geometry for a valid interface fracture toughness evaluation. However, this sensitivity issue regarding the side groove geometry impact on the interface fracture toughness evaluation will need to be evaluated from further study.

4.6. Conclusions

A unique approach has been developed for utilizing the SNTT method to estimate interface fracture toughness of bimaterial interfaces. It gave the estimated interface fracture toughness as 3.7 N-m/m² and the estimated equivalent Mode I interface fracture toughness as 1.1 MPa$\sqrt{m}$. This new approach for interface toughness research was validated by using MA956 material, but the developed methodology can be extended to other coating materials or bi-materials in general. Regarding the analytical evaluation, a more detailed parameter study and further refinement of the numerical models are needed. This additional analytical investigation would provide more details regarding the sensitivity of the varied parameters—such as the void element and the location of the crack tip to the accuracy of the evaluated interface fracture toughness.

CHAPTER V

MONTE CARLO SIMULATION OF INTERFACIAL FAILURE FOR NON-UNIFORM STRESS FIELDS IN BRITTLE MATERIALS

5.1. Introduction

5.1.1. Overview

Modern engineering systems are being increasingly manufactured from components that combine two or more materials for enhanced performance. The increased use of adhesives as a substitute for conventional mechanical fastening devices has called considerable attention to stress and strength analyses of various types of adhesive joints. Recent investigations show that the interfacial bonding strength has profound influence on the failure of dissimilar or composite materials (Hutchinson and Suo, 1992; Xu and Rosakis, 2002a; Needleman and Rosakis, 1999; Bogy, 1971). The accurate measurement of the interfacial bonding strength is critical for the evaluation of strength, durability and performance of such new materials. As two kinds of materials (adhesives and adherends) are used in bonding, bonding strength measurements are more complicated than the traditional strength measurements for homogeneous materials (Reedy and Guess, 1993; Xu et al., 2004c). It is the presence of this stress singularity that leads to erroneous results in current interfacial strength measurements. In order to reduce the stress singularity effect, Xu et al. (2003) recently designed selected artificial interfaces in bulk polymers such as PMMA and Homalite, as depicted in Fig. 5.1, and utilized different adhesives to achieve different bond strengths. The adhesive properties

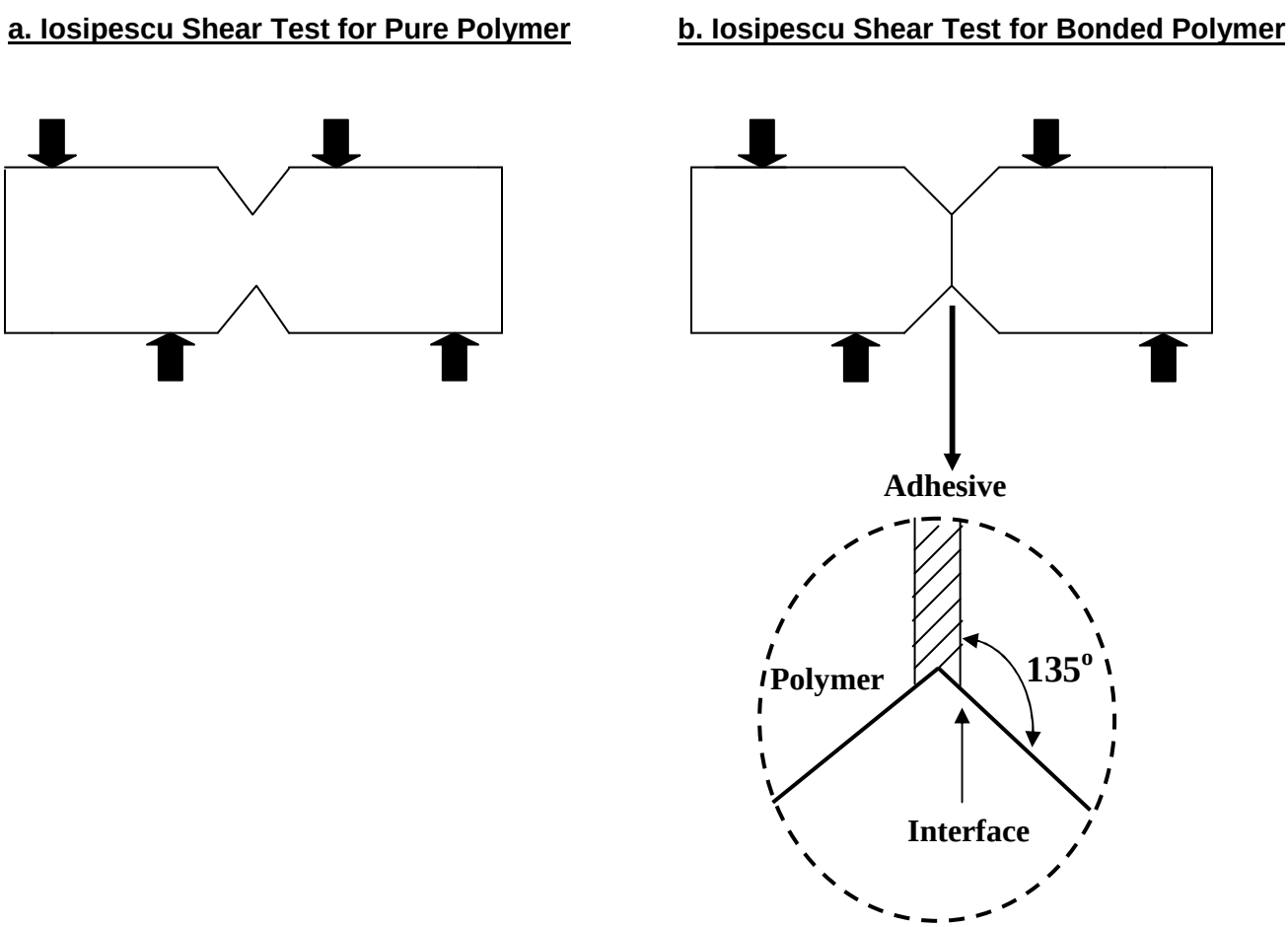

Fig. 5.1. Illustrations of Iosipescu shear tests for monolithic and bonded polymers

were chosen to be close to those of the bulk polymers. Hence, the stiffness mismatch was minimized and the magnitude of interfacial bond strength could be accurately characterized. Predictably, the magnitude of the stress singularity was low.

5.1.2. Objectives

The objectives of this study are (a) investigation of the shear stress distributions along the interface of Iosipescu specimens by means of an integrated experimental and numerical approach and (b) the influence of the presence of flaws on the interfacial shear strength of bonded interfaces in these two configurations. An illustration of the bonded shear specimens with the projected shear stress distributions is depicted in Fig. 5.2. Since these polymers have intrinsic optic-mechanical properties, optical methods were employed to record in-situ stress development during loading process. The experimental stress fields obtained from Xu et al. (2004d) were directly compared to the results from finite element analysis for validation purposes.

While the first part of this study concentrates mainly on idealized perfectly bonded interfaces; in reality, such interfaces do not exist. The presence of air bubbles and/or flaws in the adhesive contribute to the degradation of the integrity of the interface. The second part of the study, therefore, concentrates on using Monte Carlo simulation in estimating interfacial failure under non-uniform stress fields (which arise due to the presence of flaws) in brittle materials. It is worthwhile to mention here that the differences in fracture behavior amongst ductile, brittle and quasi-brittle materials are dependent on the development of a large inelastic zone ahead of the crack tip. The fracture process zone is characterized by progressive softening and is surrounded by a non-softening zone characterized by hardening plasticity. Together, these two zones form

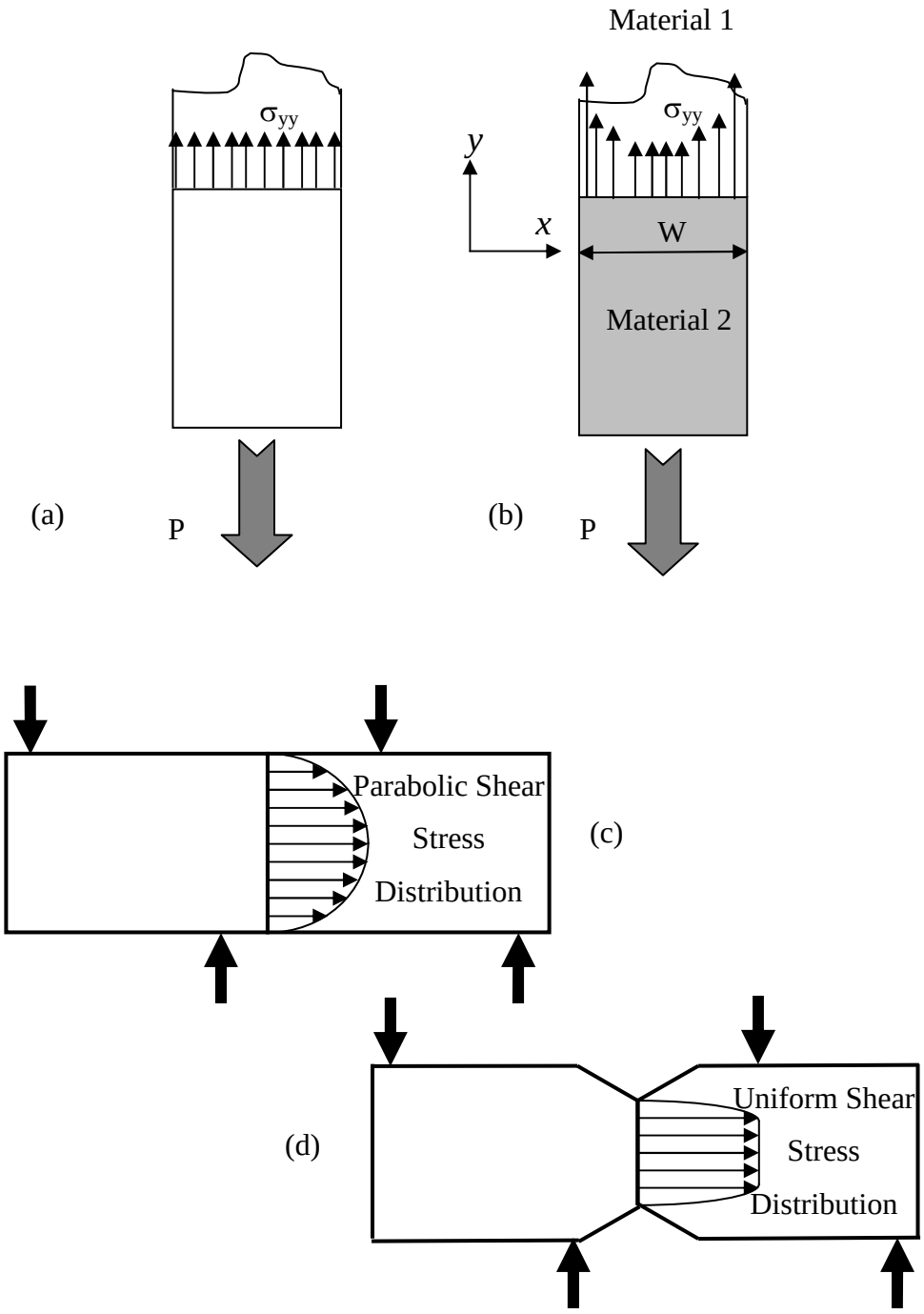

Fig. 5.2. Normal stress distributions of typical tensile specimens constituted of (a) same material (b) dissimilar materials. Interfacial shear stress distributions of (c) joint beam specimen – parabolic distribution and (d) Iosipescu shear specimen – uniform distribution

a nonlinear zone. In brittle materials, however, the whole nonlinear zone is small compared to the structure size. Then, the entire fracture process takes place almost at one point, the crack tip. The whole body is elastic and linear elastic fracture mechanics can be used (Zdenek and Planas, 1997).

The mechanical properties, shear modulus, Young's modulus and the strength of adhesives can be determined by butt and lap shear specimens. Of quite a different nature is the design concept that uses fracture mechanics to design adhesively bonded joints. The reasons to use fracture mechanics are the permanent existing singular corners between the adhesive and the adherend and the permanent existence of flaws (Pang and Seetoh, 1997). At this time, there are many specimens in use for the fracture testing of adhesive joints e.g. double cantilever beam, end notched flexure beam etc. However, for our purpose, we are interested in pure shear loading which is obtained as nearly as possible in Iosipescu specimens. A failure criterion is needed to predict the load carrying capacity of the bonded joint. The fracture mechanics discipline assumes that flaws are inherently present in the adhesive joint as a result of imperfect bonding or manufacturing defect. The quantity most often used in fracture mechanics to predict failure is the critical stress intensity factor, which determines the onset of rapid fracture (Sih, 1980). Stress concentration and non-uniform stress states are generated in the joints, when static loads are applied, due to geometric or material discontinuity. In particular, it is well known that stress singularity occurs at the edges of the interface between the adherends and the adhesive and that fracture will initiate at these positions. If bubbles are created and

remain in the adhesive layer during the bonding process, the stress concentrates around these hole defects and at the edges of the interface (Nakagawa et al., 1999).

Failure in an adhesive joint can occur in one of two ways: (i) adhesive failure occurring at the interface of adhesive/adherend (ii) cohesive failure occurring either in the adhesive or in the adherend (Reddy and Roy, 1988). It should be mentioned here that the purpose of this paper is not to model the adhesive and the failure therein but rather to model the effect of the interfacial stress fields on the ultimate strength distribution. Hence, if the material properties of the adherend and the adhesive are very similar, as chosen in the current study, the need for modeling the adhesive is effectively eliminated and the weak interface serves as a site for failure.

5.2. Experimental Investigation

5.2.1. Materials and specimens

Test materials included Homalite-100 and PMMA bonded with a weak adhesive (Xu et al., 2004d). Regular butt-joint and Iosipescu shear specimens were utilized for measuring the shear strengths of bonded and bulk (monolithic) polymer specimens.

The results of the shear tests on bulk polymer specimens were also used for the purpose of comparison and validation of finite element analysis. The advantage of the Iosipescu shear test is that a uniform shear stress distribution is produced in the gauge area of a compact specimen. To provide different interfacial bonding strengths, five kinds of adhesives – Weldon10, polyester, Loctite 330, Loctite 384 and Loctite 5083 – were used to bond the interfaces. Polyester, Weldon-10 and Loctite 330 are considered to be "strong adhesives". Loctite 384 forms an "intermediate strength bond" while Loctite

5083 gives a "weak bond". The thickness of the final adhesive layer was less than 20 μm. For bonded shear specimens, the interface of the adhesive and polymer may be a source of stress singularity since two dissimilar materials are involved.

Photoelasticity results were obtained for Homalite specimens (Singh and Shukla, 1996). The isochromatic fringe patterns observed were the contours of the maximum in-plane shear stress. These experimental results were useful in comparing the development of stress patterns, serving as an indirect means of validation of the numerical model. More details of the optical technique and experimental setup can be found elsewhere (Rosakis et al., 1998).

5.3. Numerical Investigation

5.3.1. Finite-element modeling

The stress/strain fields of the bonded butt shear and Iosipescu shear specimens were analyzed using the commercial finite element analysis software ANSYS. The dimensions of the Homalite specimen were chosen as: length of 76 mm, height of 20 mm and thickness of 6.45 mm. The finite element mesh was constructed using eight-node plane-stress elements (with thickness) and six-node triangular elements. The models were constructed as linear, elastic materials with Young's modulus E = 2.4 GPa and Poisson's ratio ν = 0.35 for Homalite-100 and for adhesive Loctite-384 E=2.76 GPa, ν = 0.35 (thickness = 20 μm). The gauge area was meshed finely with triangular elements to examine any stress singularity around the sharp or rounded notch, as the case might be, while a relatively coarse mesh of quadrilateral elements was used for the remaining area of the specimen. Finite element meshes of the bonded and monolithic Homalite-100

specimens had different levels of refinement since a possible stress singularity was expected in the bonded Homalite specimen.

Owing to large deformations expected in the specimen response, a linear static analysis was adopted incorporating large deformation effects, along the lines described in (Ho et al., 1993; Kumosa and Han, 1999). Basically, this means that a realistic simulation of load transfer from the fixture to the Iosipescu specimen was attempted in the following manner: (a) Since the left portion of the specimen is clamped during the experiment while the right hand portion of the specimen is allowed to move, the boundary conditions were specified by applying zero displacement constraints along the fixture-to-specimen contact region on the stationary left part of the specimen while uniform vertical displacement was applied on the top and bottom edges of the movable right part of the specimen. (b) After a single run, the reaction forces developed along the fixture-to-specimen contact region were checked to verify that none of the forces were tensile. If tensile reaction forces were encountered at nodes where compressive reactions were expected, the restraints at those nodes were removed and a new analysis with the revised set of boundary conditions was performed. This process was repeated until convergence was achieved. (c) The total load applied to the specimen was obtained by summation of reaction forces on the right hand portion of the specimen. Consecutive load steps at intervals of 0.5 mm were analyzed until applied displacement on the specimen reached 2 mm.

The numerical photoelasticity fringe patterns in the Homalite specimens were obtained by utilizing the same mesh as described above, except that PLANE42 elements were used solely to meet requirements of the plotting software Tecplot. After obtaining the principal stresses at each node from the finite element analysis, the numerical fringe

order N was computed. These fringe orders were then converted to gray-scale values by assigning a gray-scale value of 255 to full fringe orders (e.g. 0, 1, 2 etc.) and a gray-scale value of 0 to half fringe orders (e.g. 0.5, 1.5, 2.5 etc.). The gray-scale values were then plotted using Tecplot to get the numerical fringe patterns.

5.3.2 Monte Carlo simulation – a probabilistic viewpoint

This technique has proved to be a powerful tool for evaluating the risk or reliability, in other words the underlying probability of failure, of complicated engineering systems (Haldar and Mahadevan, 2000). In the simplest form of the basic simulation, each random variable in a problem is sampled several times to represent its real distribution according to its probabilistic characteristics. Considering each realization of all random variables in the problem produces a set of numbers that indicates one realization of the problem itself. Solving the problem deterministically for each realization is known as a simulation cycle.

The Monte Carlo simulation technique has six essential elements: (1) defining the problem in terms of all the random variables (2) quantifying the probabilistic characteristics of all the random variables in terms of their probability density functions (3) generating values of these random variables (4) evaluating the problem deterministically for each set of realizations of all the random variables (5) extracting probabilistic information from N such realizations (6) determining the accuracy and efficiency of the simulation.

As mentioned before, contingent on validation of Iosipescu and butt-joint shear specimens (numerical and experimental comparison); Monte Carlo simulations were set up in order to investigate the influence of non-uniform interfacial stress fields on the

ultimate interfacial shear strength distribution. Although it is acknowledged that there might be several competing flaw distributions present at the interface, it was assumed that only one flaw would cause and lead to ultimate failure of the specimen. The size and position of this flaw along the interface were treated as random parameters.

Based on the finite element analyses conducted on the Iosipescu and butt-joint shear specimens, a probabilistic design procedure was developed. The details of this procedure are given below.

(a) An analysis file containing the complete sequence was created to be used during looping. Quantities that would be used as random input variables, physical quantities "a" (flaw size) and "l" (flaw location) and output parameter, mode II stress intensity factor, were specified within the analysis. Within the analysis file, the input variables were initialized for the first run.

(b) Parameters were established in the ANSYS database to correspond to those used in the analysis file.

(c) The probabilistic design system was invoked and the analysis file was specified. A failure criterion was chosen such that a specimen would be assumed to have failed completely once the stress intensity factor reached the threshold of fracture toughness.

(d) No correlations were assumed between the random input variables. Direct Monte Carlo method was specified.

(e) Specified number of loops was executed within the probabilistic design cycle and for each cycle; a value for K_{II} was obtained.

(f) Probabilistic analysis results were reviewed to determine the number of failed specimens.

The two specimens (butt-joint and Iosipescu shear configurations of Homalite//Loctite-384//Homalite) were subjected to increasing displacement. To start out, three different displacements were applied: 0.2, 0.5 and 1.0 mm. K_{II} was computed for all these three cases corresponding to a central flaw location (l = 0.0). If the specimens did not fail at a displacement of 1.0 mm, the applied displacement was further increased until ultimate failure was reached (the maximum applied displacement did not exceed 2.0 mm in any case).

There is considerable dearth of literature related to the mode II fracture toughness value of a Homalite/Adhesive/Homalite interface. Ramsteiner (1993), in attempting to investigate mode II failure in polymers, postulated that K_{IIC} values are either very close to K_{IC} values or often only slightly higher, probably due to friction effects between the shearing planes and the slightly lower dilatational strain in the specimen under shear than under tensile stress. In light of this, the Mode I fracture toughness value was chosen as the lower limit of the failure criterion:

$$K_{II} > K_{IIC} = K_{IC} \tag{5.1}$$

Here, K_{IC} was chosen to be equal to K_{IIc} i.e. 0.38 MPa$\sqrt{m}$ (Xu and Rosakis, 2003). When the failure criterion was satisfied, the corresponding load was recorded and the interfacial failure shear strength was equal to the failure load divided by the cross-sectional area of the interface (=F/A).

The analysis of failures in inorganic glass and ceramics is far from simple, with the flaw shape and different types of crack growth complicating any size assessment.

Much of the use of fracture mechanics has been limited to large cracks. However, brittle failures from small inherent flaws do occur even at gross yielding, and from a practical design viewpoint it is important to have some knowledge of their nature and also to be able to predict how failures progress from them. Hashemi and Williams (1985) demonstrated from a series of experiments that surface flaws in polymers varied in length from 40 microns to 140 microns. While the lower value is acceptable, the higher limit on flaw size was increased, for purposes of the present investigation, to 1000 microns – as per observations in our experiments.

A lognormal distribution was assumed for the interface flaw size distribution (Haldar and Mahadevan, 2000). The PDF for lognormal distribution is:

$$f_X(x) = \frac{1}{\zeta_X x\sqrt{2\pi}} \exp\left[-\frac{1}{2}\left(\frac{\ln x - \lambda_X}{\zeta_X}\right)^2\right] \tag{5.2}$$

It was assumed that 90% of samples were covered in the 40-1000 microns range. According to this assumption, a 5% probability was assigned to the lower bound (40 microns) and a 95% probability was assigned to the upper bound (1000 microns). From this assumption, the mean and standard deviation of flaw size were calculated as:

$$\begin{aligned} \Phi\left[\frac{\ln 1000 - \lambda_X}{\zeta_X}\right] &= 0.95 \\ \Phi\left[\frac{\ln 40 - \lambda_X}{\zeta_X}\right] &= 0.05 \end{aligned} \tag{5.3}$$

The interfacial flaw location was chosen as a uniform variable assuming value between 0.0 and 0.9. In other words, it was assumed that the flaw could exist at any point on the interface with equal probability. At every flaw location, the flaw size was looped over and for every flaw size; all applied displacements between 1-2 mm were covered.

The stress intensity factor was checked at every step to determine if it exceeded the critical fracture toughness. Once the failure criterion was satisfied, the corresponding fracture load was recorded to determine the nominal shear stress at the interface.

5.4. Results

5.4.1. Comparison of experimental and numerical stress analysis for Iosipescu shear tests

The first and most important step was a direct comparison of experimental stress analysis and finite element simulation. As long as it could be verified that the stress singularity was weak and that the stress field was quite uniform in bonded specimens, valid bonding strength measurements were expected.

Interesting phenomena were observed during the Iosipescu shear tests. In order to understand the possible stress field change between a standard Iosipescu shear specimen (same material) and a bonded Iosipescu shear specimen (dissimilar materials because of the thin adhesive layer), we made a direct comparison of experimental and numerical photoelastic patterns as shown in Fig. 5.3. As the applied load was increased from 150 N to 400 N, the fringe patterns became more severe, as expected. No significant fringe pattern concentration was observed at the bonded notch. The stress singularity order was calculated for the bonded shear specimens using the approach outlined in Bogy (1971). A very weak singular order ($\lambda = 0.014$) was found and so, it appears logical that there is no fringe pattern concentration observed in bonded specimens.

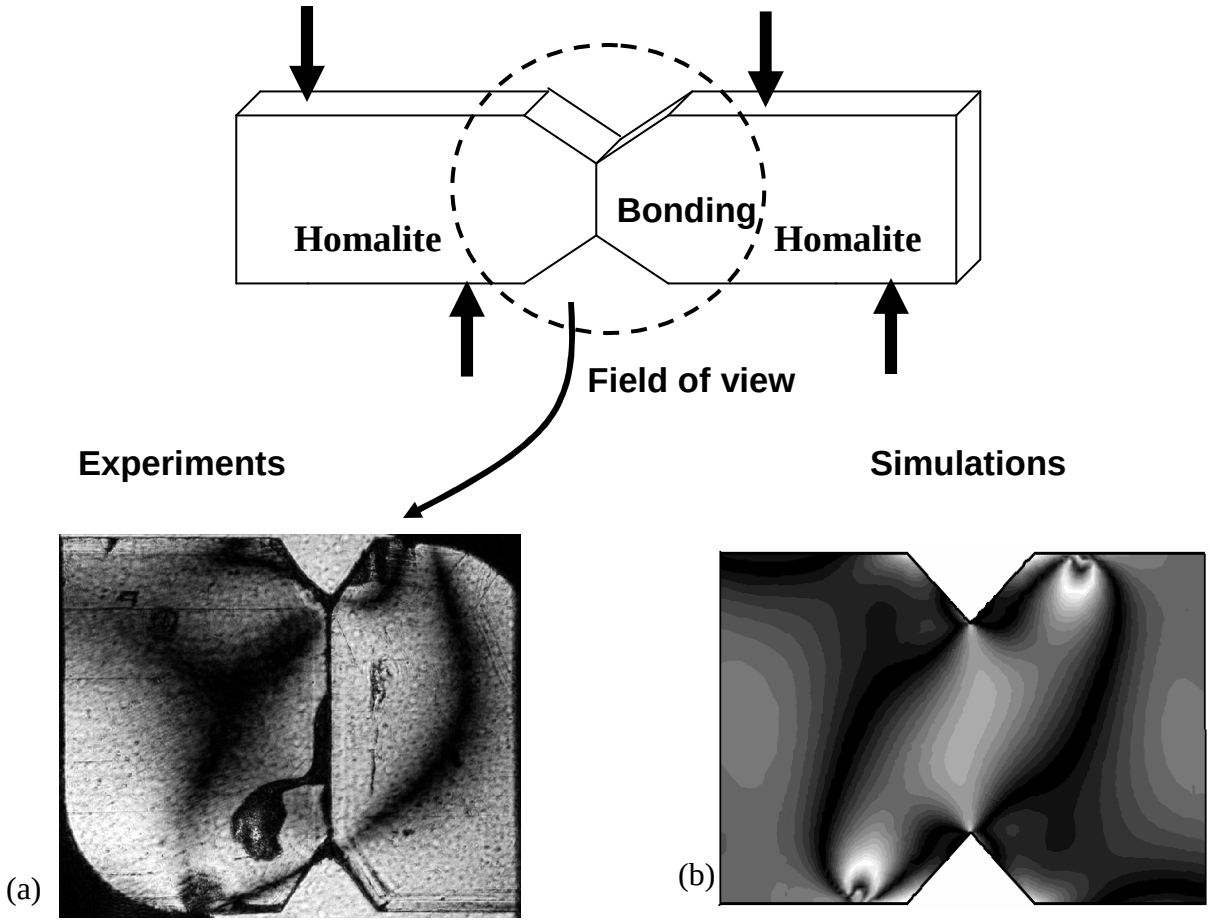

Fig. 5.3. Direct comparison of photoelastic pictures and finite element simulations for a bonded Homalite Iosipescu shear specimen.

Therefore, the shear stress distribution is quite uniform across the gauge area as seen in Fig. 5.4(b) for the bonded Homalite-100 specimen, which is very similar to the standard shear specimen seen in Figure 5.4(a). It should be mentioned here that the shear stress was plotted along the interface for both the bonded and monolithic Homalite-100 specimens, although in Figs. 5.4(a) and 5.4(b), more than half of the specimen meshes are shown. This was done only to emphasize the geometry of the rounded and sharp notched specimens. After a relatively uniform stress distribution was verified, the specimens were loaded to failure to measure bonding strengths.

For most bonded shear specimens, failure occurred along the bonding line so we could get the shear bonding strengths defined by F (failure load) /A (gauge area) and these data are listed in Table-1. However, for all Homalite specimens without adhesive bonding and for some specimens with strong Weldon-10 and polyester bonds, the shear specimen often failed in a tensile mode at the upper edge rather than an ideal shear mode at the gauge area. Similar phenomena were also reported in previous experiments by other researchers (Walrath and Adams, 1984; Sullivan, 1988; D'Almeida and Monteiro, 1999), and this mechanism can be easily explained using finite element stress analysis (Xu et al., 2004d).

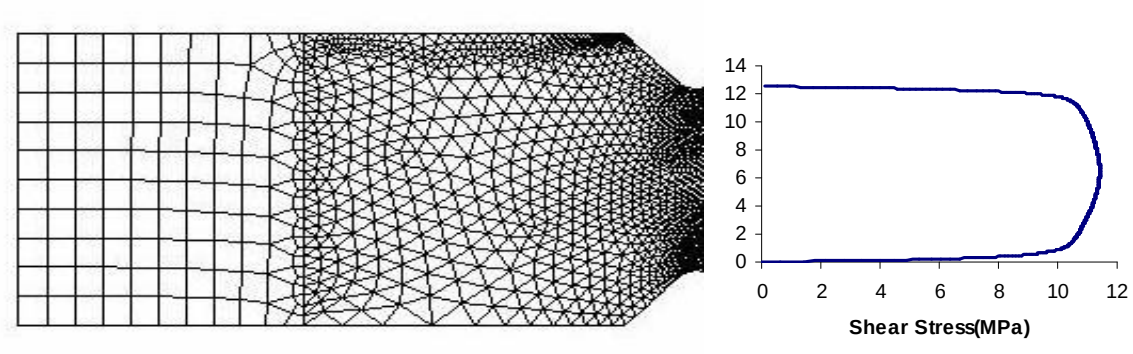

(a)

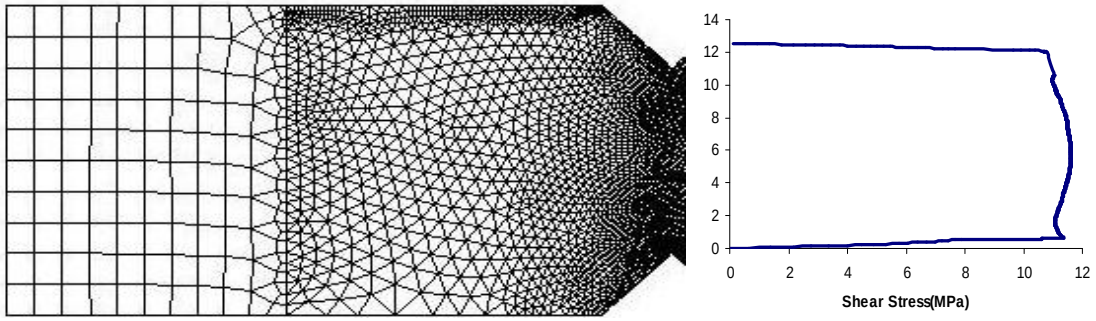

(b)

Fig. 5.4. Comparison of shear stress distributions in the gauge section in (a) Monolithic Homalite (b) Bonded Homalite

Table 1. Measured Bonding Strength Data

Polymer // adhesive //polymer	**Tensile Strength (MPa)**	**Shear Strength (MPa)**
Homalite // Polyester // Homalite	28	> 23.26
Homalite //Weldon-10 // Homalite	7.74	> 21.65
Homalite // 330 // Homalite	6.99	12.58
Homalite // 384 // Homalite	6.75	7.47
Homalite // 583 // Homalite	1.53	0.81

5.4.2. Results from Monte Carlo simulations

The Monte-Carlo simulations that were run on partially bonded Homalite specimens assumed weak bonding (Loctite 384) and according to Table 1, the Iosipescu shear specimens should have yielded interfacial strengths in the range of 7-8 MPa. However, Figs. 5.5(a), (b) yield high interfacial strength results in simulation, as compared to experimental observations.

In all the figures, it is clear that the scatter in Iosipescu shear interfacial strength is less than that recorded in butt-joint shear tests. This runs parallel to the prior observations where the non-uniform stress in butt-joint shear specimens was significantly higher than that in Iosipescu shear specimens. As a result, Iosipescu shear test specimens lend more credibility to the shear strength data. However, it is also noted that the mean interfacial strength in the baseline study is around 22 MPa for Iosipescu shear specimens, almost three times the experimentally observed value (7-8 MPa).

This discrepancy in strength data is not due to shortcomings of the simulation procedure. Accuracy of analysis results is, for the most part, dependent on the accuracy of the input. This overestimation in interfacial strength may therefore be attributed to several factors. It is the assumption that determines the magnitude of the error. Hence, a discussion on simulation assumptions and consequent effect on the results may shed some light on the discrepancy between experimental and simulation findings:

1. A mathematically sharp crack was assumed in fracture mechanics modeling. For the interface strength analysis, it is implied that fracture indeed occurs

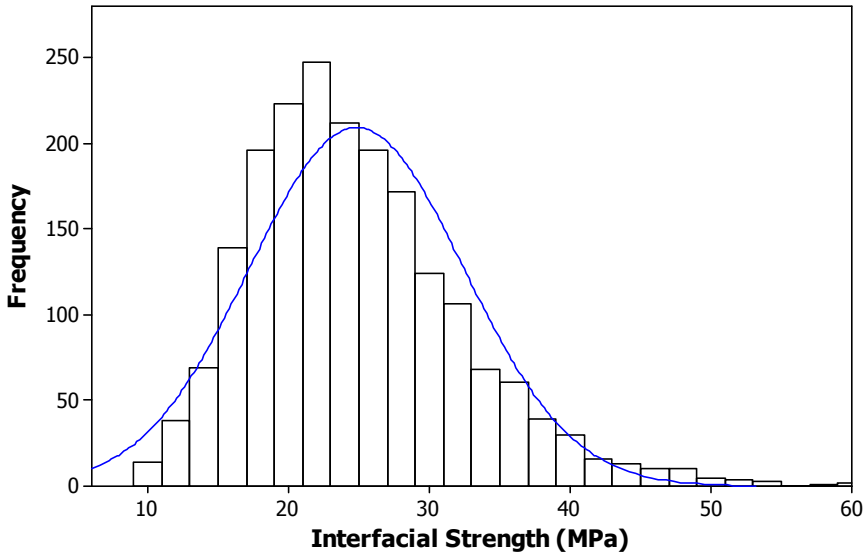

Fig. 5.5a. Interfacial strength distribution for butt joint shear; fracture toughness = 0.38 MPa√m. Mean = 24.83 MPa, Standard Deviation = 7.63 MPa, Number of Samples = 2000.

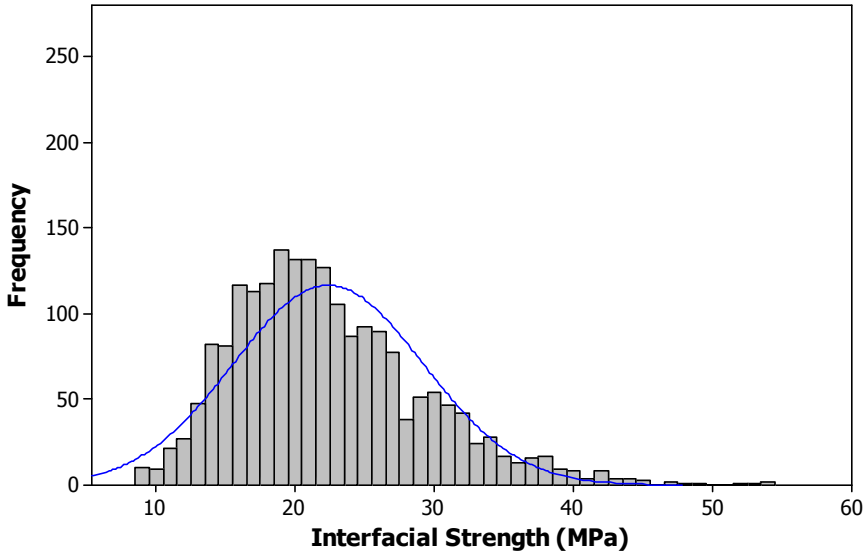

Fig. 5.5b. Interfacial strength distribution for Iosipescu joint shear; fracture toughness = 0.38 MPa√m. Mean = 22.37 MPa, Standard Deviation = 6.85 MPa, Number of samples = 2000.

when the highest stress intensity factor anywhere equaled the fracture toughness. If the flaw is circular, the stress intensity is the same everywhere and the use of this assumption is justified (Broek, 1988). However, in the case of an elongated flaw, the stress intensity at the end of the flaw would be less than the toughness at the point of satisfaction of this criterion. So, depending on the shape and size of the flaw, fracture could be either pre-poned or postponed. It is not possible to assess this theoretically – however, a correction factor could be applied to compensate for this overestimation.

2. The size of the flaw in question takes into account all representative flaw sizes that might be present at the interface. As such, it is difficult to predict the bounds on flaw size. A more realistic scenario would be the presence of multiple flaws at the interface. The proximity of these flaws would determine the onset of coalescence and possible failure. Further study is needed on this issue and use of a correction factor for this is justified.
3. The simulation model was two-dimensional in contrast to an actual three-dimensional specimen. Although the specimen thickness was entered as a parameter, this precludes the presence of flaws along the width of the specimen although admittedly, the width of the specimen is far less than the breadth of the specimen.
4. It was hypothesized that since the Iosipescu specimens exhibit a more uniform state of stress (shear stress) at the interface in comparison to butt joints (which exhibit both normal and shear stresses and also stress concentrations at the edges), the standard deviation of interfacial strength in the latter would be more than that

in the former specimen. While this trend is corroborated in the simulation results, the values are 3-4 times higher than test results. From the above discussion, it can be surmised that application of a correction factor brings the simulation results at par with the test results.

Based on the above conclusions, applying a correction factor of 3, the failure strength distributions for the three different cases (a) fracture toughness = 0.38 MPa√m (b) 0.76 MPa√m and (c) 1.14 MPa√m stand modified as shown in Figs. 5.6-5.8. The mean interfacial strength values and standard deviations of the scaled data are presented in Table 2.

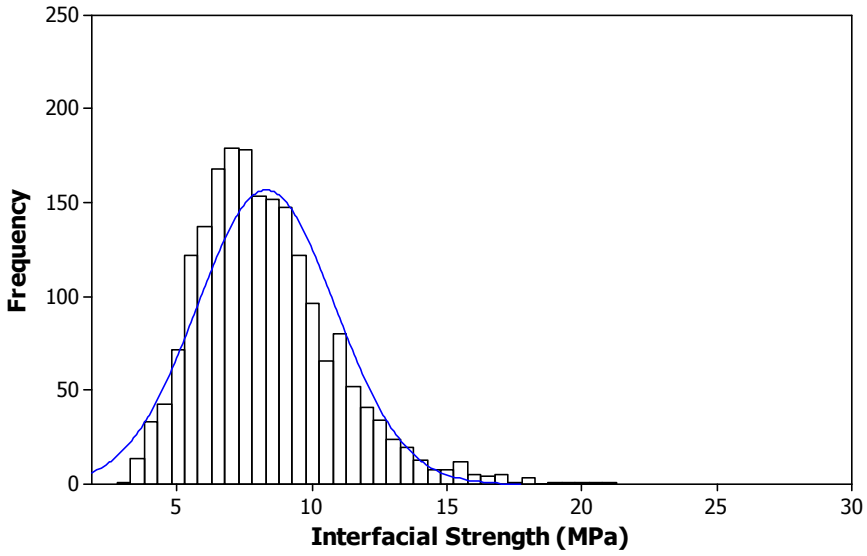

Fig. 5.6a. Scaled Interfacial strength distribution for butt joint shear; fracture toughness = 0.38 MPa√m. Mean = 8.28 MPa, Standard Deviation = 2.54 MPa, Number of samples = 2000.

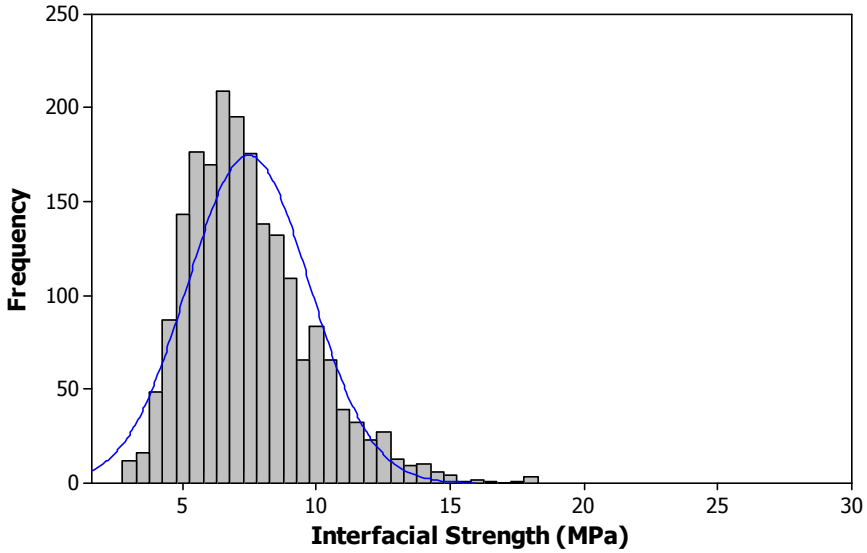

Fig. 5.6b. Scaled Interfacial strength distribution for Iosipescu joint shear; fracture toughness = 0.38 MPa√m. Mean = 7.46 MPa, Standard Deviation = 2.28 MPa, Number of samples = 2000.

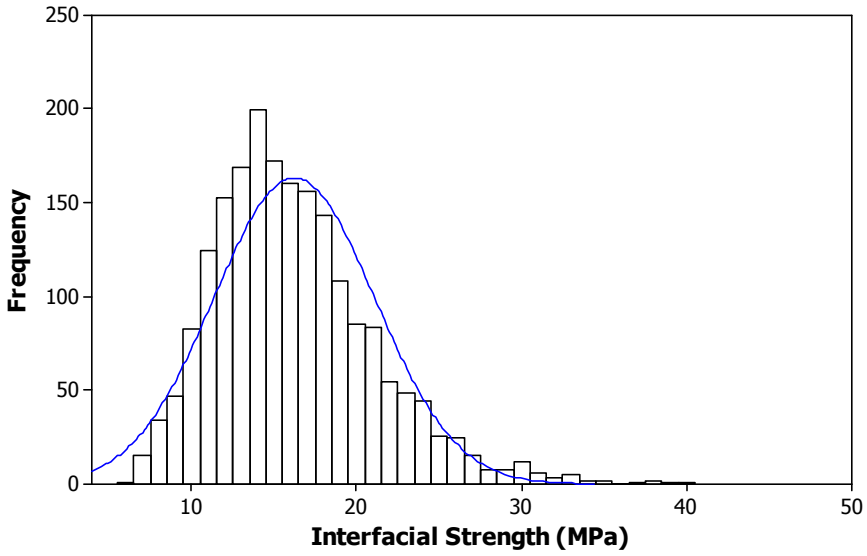

Fig. 5.7a. Scaled Interfacial strength distribution for butt joint shear; fracture toughness = 0.76 MPa√m. Mean = 16.22 MPa, Standard deviation = 4.89 MPa, Number of samples = 2000.

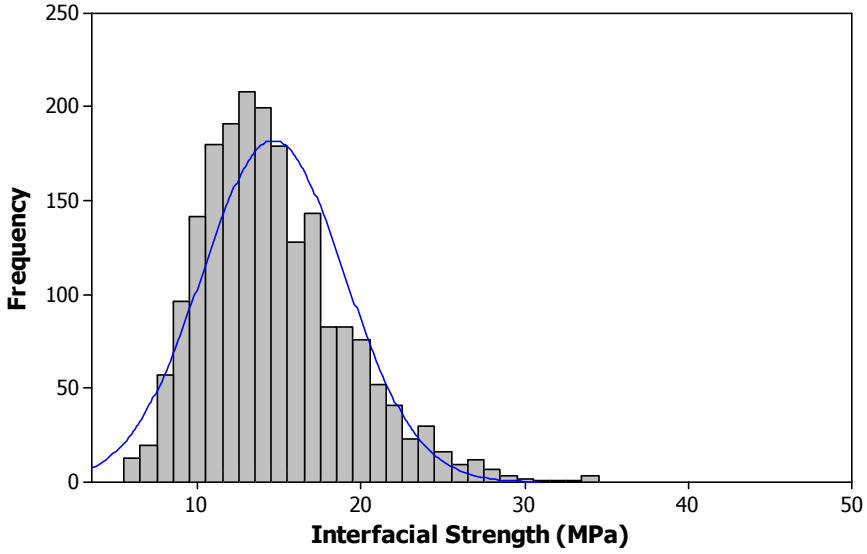

Fig. 5.7b. Scaled Interfacial strength distribution for Iosipescu joint shear; fracture toughness = 0.76 MPa√m. Mean = 14.62 MPa, Standard Deviation = 4.38 MPa, Number of samples = 2000.

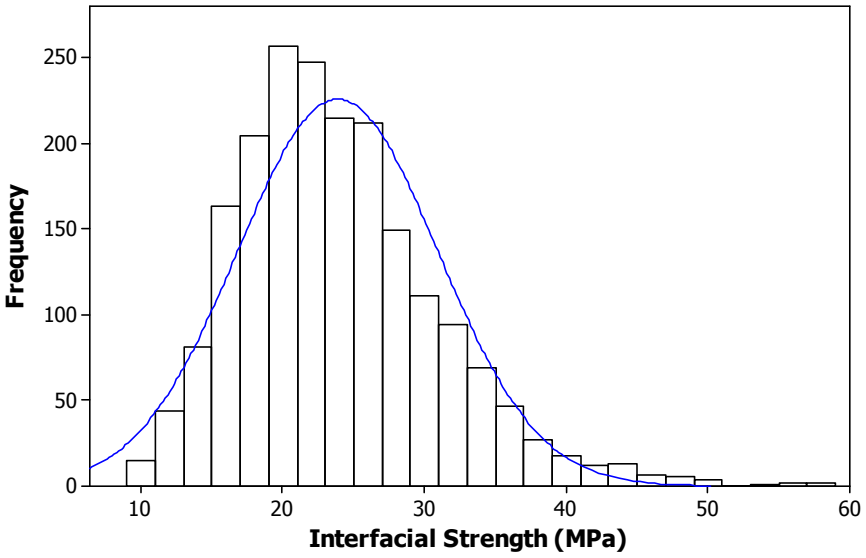

Fig. 5.8a. Scaled Interfacial strength distribution for butt joint shear; fracture toughness = 1.14 MPa√m. Mean = 23.88 MPa, Standard Deviation = 7.07 MPa, Number of samples = 2000.

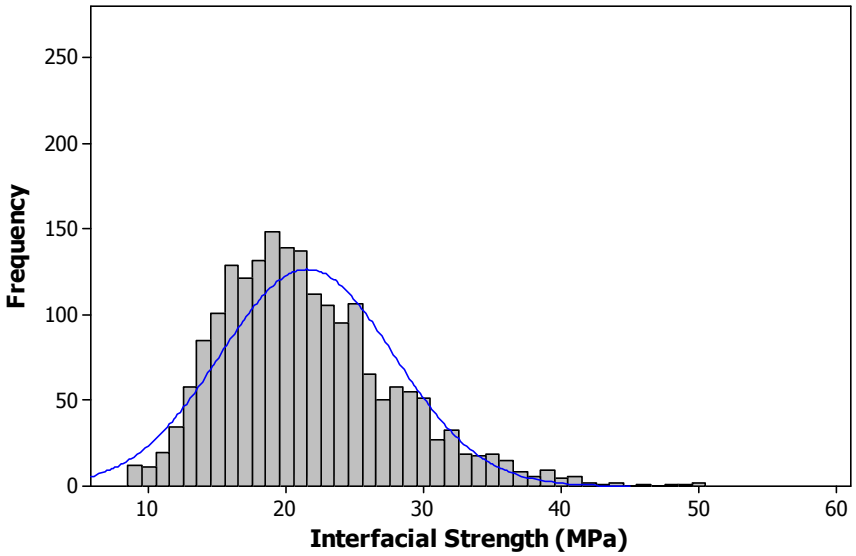

Fig. 5.8b. Scaled Interfacial strength distribution for Iosipescu joint shear; fracture toughness = 1.14 MPa√m. Mean = 21.5 MPa, Standard Deviation = 6.31 MPa, Number of samples = 2000.

Table 2. Interfacial Strength Statistics of Butt Shear and Iosipescu Shear Specimens for Varying Fracture Toughnesses

	Fracture toughness=0.38 MPa√m		Fracture toughness=0.76 MPa√m		Fracture toughness=1.14 MPa√m	
Mean Interfacial Strength (MPa)	Butt Shear	Iosipescu Shear	Butt Shear	Iosipescu Shear	Butt Shear	Iosipescu Shear
	8.28	7.46	16.22	14.62	23.88	21.5
Standard Deviation (MPa)	2.54	2.28	4.89	4.38	7.07	6.31

5.5. Conclusions

After we added a correction or fitting factor of 3, the interface shear strength data appear to be closer to the experimental range. However, our major focus was not to fit parameters – rather, it was to examine the average interface shear strengths and their standard deviations from the perspective of two different shear strength measurements. The influence of non-uniform stress field on the ultimate interfacial strength measurement was studied, and we concluded that the variation in strength values in Iosipescu specimens is less than that in butt-joint shear specimens (10%), however, the mean interface shear strengths are quite close (within 10% of each other). Since Iosipescu test setup is quite complicated, we highly recommend using butt-joint specimens to measure shear bonding strengths.

Meanwhile, our integrated investigation of finite element analysis and experimental stress analysis showed that along the polymer/adhesive/polymer interface of the Iosipescu shear specimen, a very weak stress singularity was found, so the stress distributions were quite uniform. Therefore, as long as the global interface stress is not singular (such as in straight butt-joint dissimilar materials (Xu et al., 2004b), the measured strength data should be close.

CHAPTER VI

CONCLUSIONS AND FUTURE WORK

With increasing demands on multi-functional needs in civil, aerospace, automobile and biomedical applications, the need for accurate characterization of multi-layer systems has become imperative. The bi-material interface is a subset of multi-layer the system. The overall mechanical behavior and response of bi-material interfaces is dependent on the mechanical properties and fracture behavior of the system. The presence of weak fiber-matrix interfaces, debonding at adhesive-bonded interfaces and at thin film-substrate interfaces highlight the role of interfacial mechanics. In this dissertation, the aim has been to address this topic by numerical simulations based on analytical derivations and subsequent validation by experiments conducted in the laboratory.

Characterization of interfacial tensile strength, examination of stress transfer across the nanocomposite fiber-matrix interface, interfacial fracture toughness measurement and the influence of non-uniform stress fields on interfacial strength have been addressed in the current study. However, for each of these topics, the preliminary investigation reveals a need for further scope of work in this field. For example, while stress singularity was reduced by designing convex shaped specimens, the need for absolute removal of inaccuracies can only be achieved by examining an axisymmetric specimen. In fracture toughness measurement, there is a huge potential for work that involves the influence of parameters like the shape of the groove, position and shape of

the void on interfacial fracture toughness. While butt joints and Iosipescu joints are traditionally used for tensile and shear stress measurement at the interface, the presence of voids and bubbles at the interface cannot be completely discounted. While the influence of the non-uniform stress fields on the interfacial strength has been investigated in the penultimate chapter, it was achieved by a rudimentary model based on the flaw shape and location. Further work can be conducted, either from a deterministic or a probabilistic point of view, to verify results.

REFERENCES

1. Akisanya, A.R. and Meng, C.S. (2003) Initiation of fracture at the interface corner of bi-material joints. *Journal of the Mechanics and Physics of Solids*, **51**, 27-46.

2. Bansal, A. and Kumosa, M. (1998) Analysis of Double Edge-Cracked Iosipescu Specimens under Biaxial Loads. *Engineering Fracture Mechanics*, **59**, 89-100.

3. Barsoum, R.S. (1988) Application of the finite element iterative method to the eigenvalue problem of a crack between dissimilar media. *International Journal for Numerical Methods in Engineering*, **26**, 541-554.

4. Baxter, W.J. (1998) The correct interpretation of the tensile strength of short fiber-reinforced composites. *Journal of Materials Science*, **33**, 5703 – 5706.

5. Bogy, D.B. (1971) Two edge-bonded elastic wedges of different materials and wedge angles under surface traction. *Journal of Applied Mechanics*, **38**, 377-386.

6. Broek, D. (1988) *The Practical Use of Fracture Mechanics*, Kluwer Academic Publishers.

7. Charalambides, P.G., Lund J., Evans A.G. and McMeeking R.M. (1989) A Test Specimen for Determining the Fracture Resistance Bimaterial Interface. *Journal of Applied Mechanics*, **55**, 77-82.

8. Chaudhury, Z.A., Newaz G.M., Nusier S.Q., Ahmed T. and Thomas R.L. (1999) Chronological Evaluation of Interfacial Damage in TBC due to Thermal Cycling. *Journal of Materials Science*, **34,** 2475-2481.

9. Chen, X.L. and Liu, Y.J. (2004) Square representative volume elements for evaluating the effective material properties of carbon nanotube-based composites**.** *Computational Materials Science*, **29**, 1-11.

10. Chue, C.H. and Liu, C.I. (2002) Disappearance of free-edge stress singularity in composite laminates. *Composite Structures*, **56**, 111-129.

11. D'Almeida, J.R.M. and Monteiro, S.N. (1999) The Iosipescu Test Method as a Method to Evaluate the Tensile Strength of Brittle Materials. *Polymer Testing*, **18**, 407-414.

12. Drzal, L.T. (1990) Fiber-matrix interphase structure and its effect on adhesion and composite mechanical properties. In: H. Ishida, Editor, Controlling Interphases in Composite Materials, Elsevier, Amsterdam, 309-319.

13. Dundurs, J. (1969) Discussion. *ASME Journal of Applied Mechanics*, **36**, 650-652.
14. Evans, A.G., Hutchinson, J.W. and He, M.Y. (1999) Micromechanics Model for the Detachment of Residually Compressed Brittle Films and Coatings. *Acta Materialia*, **47,** 1513-1522.

15. Fisher, F.T., Bradshaw, R.D. and Brinson L.C. (2003) Fiber waviness in nanotube-reinforced polymer composites—I: Modulus predictions using effective nanotube properties**.** *Composites Science and Technology*, **63**, 1689-1703.

16. Gibson, R.F. (1994) *Principles of Composite Material Mechanics*, McGraw-Hill Inc., New York.

17. Haldar, A. and Mahadevan, S. (2000) *Reliability Assessment using Stochastic Finite Element Analysis*, John Wiley & Sons.

18. Ho, H., Tsai M.Y., Morton, J. and Farley G.L. (1993) Numerical Analysis of the Iosipescu Specimen for Composite Materials. *Composites Science and Technology*, **46**, 115-128.

19. Irwin, G.R. (1957) Analysis of Stresses and Strains near the End of Crack Traversing a Plate. *Journal of Applied Mechanics*, **24**, 361-364.

20. Hashemi, S. and Williams, J.G. (1985) Fracture from inherent flaws in polymers. *Journal of Materials Science*, **20**, 4202-4208.

21. Hein, V.L. and Erdogan, F. (1971) Stress singularities in a two-material wedge. *International Journal of Fracture Mechanics*, **7**, 317-330.

22. Hutchinson, J.W. and Suo, Z. (1992) Mixed mode cracking in layered materials. *Advances in Applied Mechanics*, **29**, 63-191.

23. Klingbeil, N.W. and Beuth, J.L. (2000) On the design of debond-resistant bimaterials, Part I: Free-edge singularity approach. *Engineering Fracture Mechanics*, **66**, 93-110.

24. Kumosa, M. and Han, Y. (1999) Non-linear Finite-Element Analysis of Iosipescu Specimens. *Composites Science and Technology*, **59**, 561-573.

25. Labossiere, P.E.W., Dunn, M.L. and Cunningham, S.J. (2002) Application of bi-material interface corner failure mechanics to silicon/glass anodic bonds. *Journal of the Mechanics and Physics of Solids*, **50**, 405–433.

26. Lara-Curzio, E., Ferber, M.K., Besmann, T.M., Rebillat, F. and Lamon, J. (1995) Fiber-matrix bond strength, fiber frictional sliding and the macroscopic tensile

behavior of 2D SiC/SiC Composite with tailored interfaces. *Ceramics Engineering and Science,* **15**, 597-612.

27. Lau, K.T., Shi, S.Q., Zhou, L.M. and Cheng, H.M. (2003) Micro-hardness and Flexural Properties of Randomly-oriented Carbon Nanotube Composites. *Journal of Composite Materials,* **37**, 365-376.

28. Lau, K.T. and Hui, D. (2002) The revolutionary creation of new advanced materials—carbon nanotube composites**.** *Composites Part B,* **33**, 263-277.

29. Liou, W.J. (1997) Stress distributions of short fiber composite materials**.** *Computers and Structures*, **62**, 999-1012.

30. Lin, G., Geubelle, P.H. and Sottos, N.R. (2001) Simulation of fiber debonding with friction in a model composite pushout test. *International Journal of Solids and Structures*, **38**, 8547-8562.

31. Liu, Y., Xu, J. and Ding, H. (1999) Order of singularity and singular stress field about an axisymmetric interface corner in three-dimensional isotropic elasticity. *International Journal of Solids and Structures*, **36**, 4425-4445.

32. Luo, J.J. and Daniel, I.M. (2003) Characterization and modeling of mechanical behavior of polymer/clay nanocomposites**.** *Composites Science and Technology*, **63**, 1607-1616.

33. Mattheck, C. (1998) *Design in Nature: Learning from Trees*. Springer-Verlag, New York.

34. Mohammed, I. and Liechti, K.M. (2001) The effect of corner angles in bimaterial structures. *International Journal of Solids and Structures,* **38**, 4375-4394.

35. Munz, D. and Yang, Y.Y. (1993) Stress near the edge of bonded dissimilar materials described by two stress intensity factors. *International Journal of Fracture*, **60**, 169-177.

36. Nakagawa, F., Sawa, T., Nakano, Y. and Katsuo, M. (1999) Two dimensional finite element thermal stress analysis of adhesive butt joints with some hole defects. *Journal of Adhesion Science and Technology,* **13**, 309-323.

37. Needleman, A. and Rosakis, A.J. (1999) The effect of bond strength and loading rate on the conditions governing the attainment of intersonic crack growth along interfaces. *Journal of Mechanics and Physics of Solids,* **47**, 2411-2449.

38. Odegard, G.M., Gates, T.S., Wise, K.E., Park, C. and Siochi, E.J. (2003) Constitutive modeling of nanotube–reinforced polymer composites**.** *Composites Science and Technology,* **63**, 1671-1687.

39. Pageau, S.S., Gadi, K.S., Biggers, S.B. and Joseph, P.F. (1996) Standardized complex and logarithmic eigensolutions for n-wedges and junctions. *International Journal of Fracture*, **77**, 51-76.

40. Pang, H.L.J. and Seetoh, C.W. (1997) A compact mixed mode fracture specimen for adhesive bonded joints. *Engineering Fracture Mechanics*, **57**, 57-65.

41. Pelegri, A.A., Kardomateas, G.A. and Malik, B.U. (1997) The fatigue growth of internal delaminations under compressive loading in cross ply composite plates. *Composite Materials: Fatigue and Fracture, ASTM STP 1285*, E. A. Armanios, Ed., 146-163.

42. Pindera, M.J., Aboudi, J. and Arnold, S.M. (2000) The Effect of Interface Roughness and Oxide Film Thickness on the Inelastic Response of Thermal Barrier Coatings to Thermal Cycling. *Materials Science & Engineering A,* **284,** 158–175.

43. Pint, B.A., Wright, I.G., Lee, W.Y., Zhang, Y., Prüßner, Y. and Alexander, K.B. (1998) Substrate and bond coat compositions: factors affecting alumina scale adhesion, *Materials Science and Engineering A*, **245**, 201-211.

44. Qian, D., Dickey, E.C., Andrews, R. and Rantell, T. (2000) Load transfer and deformation mechanisms in carbon nanotube-polystyrene composites. *Applied Physics Letters*, **76**, 2868-2870.

45. Qian, D., Wagner, G.J., Liu, W.K., Min-Feng, Y. and Ruoff, R.S. (2002) Mechanics of carbon nanotubes. *Applied Mechanics Reviews*, **55**, 495-533.

46. Rabin, B.H., Williamson, R.L., Bruck, H.A., Wang, X.L., Watkins, T.R., Feng, Y.Z. and Clark, D.R. (1998) Residual strain in an Al203-Ni joint bonded with a composite interlayer: experimental measurements and FEM analysis. *Journal of American Ceramics Society*, **81**, 1541-1549.

47. Ramsteiner, F. (1993) An approach towards understanding mode II failure of poly (methyl methacrylate). *Polymer*, **34**, 312-317.

48. Reddy, J.N. and Roy, S. (1988) Non-linear analysis of adhesively bonded joints. *International Journal of Non-linear Mechanics*, **23**, 97-112.

49. Reedy, E.D. and Guess, T.R. (1993) Comparison of butt tensile strength data with interface corner stress intensity factor prediction. *International Journal of Solids & Structures*, **30**, 2929-2936.

50. Rice, J.R. (1988) Elastic fracture mechanics concepts for interfacial cracks. *Journal of Applied Mechanics*, **55**, 98-103.

51. Rosakis, A.J., Samudrala, O., Singh, R.P. and Shukla, A. (1998) Intersonic Crack Propagation in Bimaterial Systems. *Journal of the Mechanics and Physics of Solids*, **46**, 1789-1813.

52. Roy, S., Lu, H., Periasamy, S. and Ma, J. **(**2003) *Proceedings of the 44th AIAA/ASME/ASCE/AHS Structures, Structural Dynamics, and Materials Conference, Norfolk, Virginia).*

53. Schadler, L.S., Giannaris, S.C. and Ajayan, P.M. (1998) Load transfer in carbon nanotube epoxy composites. *Applied Physics Letters*, **73**, 3842-3844.

54. Shih, C.F. (1991) Cracks on Bimaterial Interfaces: Elasticity and Plasticity Aspects. *Journal of Material Science and Engineering A***, 143**, 77-90.

55. Shih, C.F. and Asaro, R.J. (1988) Elastic-Plastic Analysis of Cracks on Bimaterial Interfaces: Part I—Small Scale Yielding. *Journal of Applied Mechanics*, **55**, 299-316.

56. Shih, C.F., Moran, B. and Nakamura, T. (1986) Energy Release Rate along a Three-Dimensional Crack Front in a Thermally Stressed Body. *International Journal of Fracture*, **30**, 79–102.

57. Sih, G.C. (1980) Fracture mechanics of adhesive joints. *Polymer Engineering and Science*, **20**, 977-981.

58. Singh, R.P. and Shukla, A. (1996) Subsonic and Intersonic Crack Growth along a Bimaterial Interface. *Journal of Applied Mechanics*, **63**, 919-924.

59. Srivastava, D., Wei, C. and Cho, K. (2003) Nanomechanics of carbon nanotubes and composites. *ASME Applied Mechanics Reviews*, **56**, 215-230.

60. Sukumar, N. and Kumosa, M. (1993) Finite Element Analysis of Axial Splits in Composite Iosipescu Specimens. *International Journal of Fracture*, **62**, 55-85.

61. Sullivan, J.L. (1988) The Use of Iosipescu Specimens. *Experimental Mechanics*, **28**, 326-328.

62. Sun, C.T. and Wu, J.K. (1983) Stress Distribution of Aligned Short-Fiber Composites under Axial Load. *Journal of Reinforced Plastics and Composites*, **3**, 130-144.

63. Suo, Z. (1990) Singularities, Interfaces and Cracks in Dissimilar Anisotropic Media. *Proceedings of the Royal Society London A*, **427**, 331-358.

64. Suo, Z. and Hutchinson, J.W. (1989) Sandwich Test Specimens for Measuring Interface Crack Toughness. *Materials Science and Engineering A,* **107**, 135-143.

65. Swadener, J.G., Liechti, K.M. and Lozanne, A.L. (1999) The intrinsic toughness and adhesion of a glass epoxy interface. *Journal of the Mechanics and Physics of Solids*, **47**, 223-258.

66. Tandon, G.P., Kim, R.Y., Warrier, S.G. and Majumdar, B.S. (1999) Influence of free edge and corner singularities on interfacial normal strength: application in model unidirectional composites. *Composites, Part B: Engineering*, **30**, 115-134.

67. Thostenson, E.T., Ren, Z. and Chou, C.W. (2001) Advances in the science and technology of carbon nanotubes and their composites: a review**.** *Composites Science and Technology*, **61**, 1899-1912.

68. Tippur, H.V., Krishnaswamy, S. and Rosakis, A.J. (1991) A coherent gradient sensor for crack tip deformation measurements: analysis and experimental results. *International Journal of Fracture*, **48**, 193-204.

69. Treacy, M.M.J., Ebbesen, T.W. and Gibson, T.M. (1996) Exceptionally high Young's modulus observed for individual carbon nanotubes. *Nature*, **381**, 678-680.

70. Turner, M.R. and Evans, A.G. (1996) An Experimental Study of the Mechanisms of Crack Extension along an Oxide/Metal Interface. *Acta Materialia*, **44**, 863-871.

71. Wagner, H.D., Lourie, O., Feldman, Y. and Tenne, R. (1998) Stress-induced fragmentation of multiwall carbon nanotubes in a polymer matrix. *Applied Physics Letters*, **72**, 188-190.

72. Walrath, D.E. and Adams, D.F. (1984) The Iosipescu Shear Test as Applied to Composite Materials. *Experimental Mechanics*, **24**, 105-110.

73. Wang, J.A., Liu, K.C., McCabe, D.E. and David, S.A. (2000) Using Torsion Bar Testing to Determine Fracture Toughness, KIC. *Journal of Fatigue & Fracture for Engineering Materials and Structure*, **23**, 45-56.

74. Wang, J.A. (2003) Oak Ridge National Laboratory Spiral Notch Torsion Test System. *Journal of Practical Failure Analysis*, **3**, 23-27.

75. Wang, J.A., Liu, K.C. and McCabe, D.E. (2002) An Innovative Technique for Measuring Fracture Toughness of Metallic and Ceramic Materials. *Fatigue and Fracture Mechanics*, **33**, *ASTM STP1417*, W. G. Reuter and R. S. Piascik, Eds.

76. Williams, M.L. (1952) Stress singularities resulting from various boundary conditions in angular corners in extension. *Journal of Applied Mechanics*, **19**, 526-528.

77. Xu, L.R. and Rosakis, A.J. (2002a) Impact failure characteristics in sandwich structures; Part II: effects of impact speed and interfacial strength. *International Journal of Solids and Structures*, **39**, 4237-4248.

78. Xu, L.R., Rosakis, A.J. and Samudrala, O. (2002b) Measurements of adhesive tensile and shear strengths with the aid of two optical techniques. In: *Proceedings of the Society of Experimental Mechanics Annual Conference*.

79. Xu, L.R. and Rosakis, A.J. (2003) An experimental study of impact-induced failure events in homogeneous layered materials using dynamic photoelasticity and high-speed photography. *Optics and Lasers in Engineering*, **40**, 263-288.

80. Xu, L.R., Huang, Y.Y. and Rosakis, A.J. (2003) Dynamic Crack Deflection and Penetration at Interfaces in Homogeneous Materials: Experimental Studies and Model Predictions. *Journal of the Mechanics and Physics of Solids*, **51**, 461-486.

81. Xu, L.R, Bhamidipati, V., Zhong, W.H., Li, J., Lukehart, C.M., Lara-Curzio, E., Liu, K.C. and Lance, M.J. (2004a) Mechanical property characterization of a polymeric nanocomposite reinforced by graphitic nanofibers with reactive linkers. *Journal of Composite Materials*, **38**, 1563-1582.

82. Xu, L.R., Kuai, H. and Sengupta, S. (2004b) Dissimilar Material Joints with and without Free-edge Stress Singularities, Part I. A Biologically Inspired Design. *Experimental Mechanics*, **44**, 608-615.

83. Xu L.R., Sengupta, S. and Kuai, H. (2004c) Dissimilar Material Joints With and Without Free-Edge Stress Singularities: Part II. An Integrated Numerical Analysis. *Experimental Mechanics*, **44**, 616-621.

84. Xu, L.R., Sengupta, S. and Kuai, H. (2004d) An experimental and numerical investigation of adhesive bonding strengths of polymer materials. *International Journal of Adhesion and Adhesives*, **24**, 455-460.

85. Yu, M.F., Lourie, O., Dyer, M., Moloni, K., Kelly, T. and Ruoff, R.S. (2000) Strength and Breaking Mechanism of Multiwalled Carbon Nanotubes under Tensile Load. *Science*, **287**, 637-640.

86. Zdenek, B. and Planas, J. (1997) *Fracture and Size Effect in concrete and other quasibrittle materials*, CRC Press.

87. Zhong, W.H., Li, J., Xu, L.R., Michel, J.A., Sullivan, L.M. and Lukehart, C.M. (2004) Graphitic Carbon Nanofiber (GCNF)/Polymer Materials. I. GCNF/Epoxy

Monoliths Using Hexanediamine Linker Molecules**.** *Journal of Nanoscience and Nanotechnology*, **4**,794-802.

88. Zhou, X.F., Wagner, H.D. and Nutt, S.R. (2001) Interfacial properties of polymer composites measured by push-out and fragmentation tests. *Composites Part A*, **32**, 1543-1551.